This is to certify that the
thesis entitled

POWDER PROCESSING, POWDER CHARACTERIZATION, AND MECHANICAL PROPERTIES OF LAST (LEAD-ANTIMONY-SILVER-TELLURIUM) AND LASTT (LEAD-ANTIMONY-SILVER-TELLURIUM-TIN) THERMOELECTRIC MATERIALS

presented by

Bradley Devin Hall

has been accepted towards fulfillment
of the requirements for the

Master of Science	degree in	Materials Science and Engineering

Eldon D. Case
Major Professor's Signature

July 25, 2008
Date

POWDER PROCESSING, POWDER CHARACTERIZATION, AND MECHANICAL PROPERTIES OF LAST (LEAD-ANTIMONY-SILVER-TELLURIUM) AND LASTT (LEAD-ANTIMONY-SILVER-TELLURIUM-TIN) THERMOELECTRIC MATERIALS

By

Bradley Devin Hall

A THESIS

Submitted to
Michigan State University
in partial fulfillment of the requirements
for the degree of

MASTER OF SCIENCE

Materials Science and Engineering

2008

ABSTRACT

POWDER PROCESSING, POWDER CHARACTERIZATION, AND MECHANICAL PROPERTIES OF LAST (LEAD-ANTIMONY-SILVER-TELLURIUM) AND LASTT (LEAD-ANTIMONY-SILVER-TELLURIUM-TIN) THERMOELECTRIC MATERIALS

By

Bradley Devin Hall

LAST (Pb-Sb-Ag-Te) and LASTT (Pb-Sb-Ag-Te-Sn) are two recently developed thermoelectric semiconductors [Hogan 2007]. LAST (composition $AgPb_{18}SbTe_{20}$) has a ZT of 1.7 at 700 K, possibly due to Ag-Sb nanostructures in the PbTe matrix [Hsu 2004].

Much work for this thesis was done to develop a powder processing technique to produce fine powders. These new procedures mixed milling media, combined dry and wet milling, and varied milling speed and milling time. The powders produced had means ranging from 20.1 to 2.9 microns and medians ranging from 12.4 to 2.1 microns. The most effective milling procedure dry milled the powder for 3 hr at 100 rpm with 140 g of 20 mm diameter Al_2O_3 media and 60 g of 3 mm diameter Al_2O_3 media (nominally), then wet milled the powder for 6 hr at 100 rpm with 25 cc of hexane using the same media. The powder produced had a mean diameter of 3.4 microns and a median diameter of 2.3 microns.

This study also included mechanical property testing and further powder characterization. The Vickers hardness for LAST ingot and hot pressed specimens ranged from 0.57 to 0.88 GPa. The biaxial flexure strength of hot pressed LAST specimens averaged 51.6 MPa. BET specific surface areas ranged from 0.047 to 2.71 m^2/g for various LAST powders. ICP spectroscopy reported impurity concentrations were typically below 35 ppm for LAST powders.

ACKNOWLEDGEMENTS

The author acknowledges the financial support of the Office of Naval Research (MURI Grant number N000140310789).

Infinite thanks go to my advisor, Dr. Eldon Case, who has been an excellent teacher, and a thorough and thoughtful mentor. Without your help, I do not know where I would be.

Very special thanks to Dr. James Lucas for his honesty and encouragement. Again, without your help, I do not know where I would be.

Thanks to those with whom I have worked on this project: Dr. Timothy Hogan, Dr. Bhanu Mahanti, Dr. Donald Morelli, Nuraddin Matchanov, Fei Ren, Chun-I Wu, Ed Timm, Jonathan D'Angelo, Muhammad Farhan, Jen Ni, Zsolt Rak, Jason Johnson, Tori Buckley, John Jackowski, Kristen Khabir, Dan Kleinow, and Jessica Micklash. Your assistance along the way is greatly appreciated.

Thanks also to those from outside this project that helped anyway: Paul Kester from Micromeritics Instrument Corporation (Norcross, GA); Kirk Stuart from the Diagnostic Center for Population and Animal Health (Michigan State University, East Lansing, MI); the Center for Advanced Microscopy at Michigan State University (East Lansing, MI); Rosa M. Trejo from the High Temperature Materials Laboratory (Oak Ridge National Laboratory, Oak Ridge, TN); Dr. Hsin Wang from the High Temperature Materials Laboratory (Oak Ridge National Laboratory, Oak Ridge, TN); and Fancisco Nam from Shiva Technologies (Evans Analytical Group LLC, Syracuse, NY)

Thanks to Mom, Dad, Lisa, Grandma, Aunt Gayle, Uncle Jim, Uncle Joe, Jeff, Jen, Jodi, Mike, and Judi. You have given me more advice than I could ever hope to remember.

Special thanks to the friends that know me best: Nate Bacon, Chris Mallory, Matt McDougall, and Mark VanZwoll. Similar thanks go to all my other friends, whom are too numerous to name individually.

Thanks to the coaches that helped to shape me into the man I am today: Tony Lopez, Matt McDougall, Don Nohel, and Melvin Richendollar.

Thanks to everyone else that I should have mentioned, but did not. You know who you are. I appreciate all that you have done for me.

TABLE OF CONTENTS

LIST OF TABLES

Vickers hardness data for the LASTT hot pressed specimens, HPMSU-4B and HPMSU-4C, was greater than the any value reported in [22].

Table 5-3.....133
Expanded set of Vickers hardness data for ingot and hot pressed LAST and LASTT materials, including the data from Table 5-2. Notice that there data for both ingot and hot pressed specimens of the composition $Ag_{0.43}Pb_{18}Sb_{1.2}Te_{20}$ and $Ag_{0.86}Pb_{19}Sb_{1.0}Te_{20}$. The LASTT ingot data are for two specimens having two different compositions, while the hot pressed data are for specimens of the $Ag_{0.9}Pb_9Sb_{0.6}Sn_9Te_{20}$ composition. The data not contained Table 5-2 comes from Jennifer Ni, Fei Ren, and [22].

Table 5-4.....134
Room temperature thermal diffusivities for selected LAST and LASTT specimens. The room temperature thermal diffusivity data for the LAST and LASTT specimens compares well with the value of 0.0162 cm^2/s reported for another LAST ingot [91]. Also, the thermal diffusivities for the LAST specimens are slightly lower than those for the LASTT specimens.

Table 5-5.....136
Biaxial flexure strength for selected hot pressed HPMSU specimens. All specimens were 22 mm in diameter. No data is reported for HPMSU-13 because the specimen broke during polishing. The biaxial flexure strength for a LASTT ingot was 15.3 MPa, meaning HPMSU-14 and HPMSU-16 have a fracture strength that is more than a factor of three increase.

Table 5-6.....140
Brunauer-Emmett-Teller (BET) specific surface areas, and calculated equivalent spherical particle diameters, of selected LAST powders. The powders underwent various premilling treatments, and some powders were dry milled, while others were both dry and wet milled. All specimens were degassed for 6 hrs at 200 °C. The specific surface area data ranges between 0.0472 and 2.71 m^2/g.

Table 5-7.....144
ICP-MS and ICP-OES specimen labels and compositions included in this study. All milling was done in a milling jar lined with 99.7% pure alumina. The impurities in the alumina liner of the milling jar were SiO_2 (0.075%), Fe_2O_3 (0.010%), CaO (0.070%), MgO (0.075%), and Na_2O (0.010%). All dry milling was done at 100 rpm with ten 99.64% pure 20 mm diameter alumina spheres. All wet milling was done at 150 rpm with 150 cc of 99.64% pure 3 mm diameter alumina spheres. The impurities in the 20 mm diameter alumina spheres and the 3 mm diameter alumina spheres were SiO_2 (0.100%), Fe_2O_3 (0.020%), CaO (0.040%), MgO (0.150%), Na_2O (0.040%), and K_2O (0.010%).

Table 5-8.....144
ICP-MS results for selected LAST powders. Specimens were tested by Shiva Technologies. For specimens 2-5, most impurities have a concentration of 35 ppm or

less. Specimen 1, however, has higher concentrations of B, Na, Sn, and K, as well as an extremely high concentration of Si (1.1 wt%). This high concentration of Si may be from a glass bead, used to clean the milling jar, getting into the powder.

LIST OF FIGURES

1. Introduction

Thomas Johann Seebeck was a German physicist who lived from 1770 to 1831. Seebeck's experiments involved work with loops composed of two different metals. At one of the junctions where the loops were connected, the metal was heated [1]. After heating one of the junctions, Seebeck observed that the temperature gradient across the hoop caused a voltage drop [2]. This observation is a result of the thermoelectric, or Seebeck, effect: a junction of two dissimilar conductors, when exposed to a temperature gradient, will have a voltage difference between its two ends [1].

The simplest application of the thermoelectric effect is in thermocouples. Two dissimilar metals, such as iron and constantan, are electrically connected at one end by soldering them together. When a temperature difference exists between the two ends of the thermocouple, there is a potential difference between the terminals that is proportional to the temperature gradient [3].

Alternatively, the thermoelectric effect can be used to construct electrical generators. The idea of thermoelectric power generation was first proposed by Lord Rayleigh in 1885 [1].

A "good" thermoelectric material should have three characteristics. First, as mentioned above, it should have a large Seebeck coefficient, S (see Table 1-1). Second, it should have a high electrical conductivity, σ (see Table 1-1). A high electrical conductivity is important to minimize losses from Joule heating. Third, it should have a low thermal conductivity, κ (see Table 1-1). A low thermal conductivity is important so that the temperature gradient across the thermoelectric elements in a TEG is maintainable [1].

The Seebeck coefficient, electrical conductivity, and thermal conductivity can be combined with temperature to create a dimensionless figure-of-merit for evaluating a thermoelectric (TE) material. This figure-of-merit is ZT, and is defined as $S^2\sigma T/\kappa$. The higher a material's ZT, the more efficiently it converts heat into electricity.

The energy conversion efficiency, η, of a TEG is given by [4]

$$\eta = \frac{T_H - T_C}{T_H}\left[\frac{\sqrt{1+ZT}-1}{\sqrt{1+ZT}+T_C/T_H}\right] \tag{1.1}$$

where T_H is the hot-side absolute temperature, and T_C is the cold-side absolute temperature. In the equation for η, the term $(T_H - T_C)/T_H$ is the Carnot efficiency [4].

Thermoelectric generators (TEGs) require materials with large Seebeck coefficients. For metals the Seebeck coefficient is typically 10 μV/K or less. TEGs built with materials having such low Seebeck coefficients would only produce electricity at efficiencies of fractions of a percent. However, some semiconductors have Seebeck coefficients that are more than an order of magnitude higher than those for metals. Traditional TE semiconductors such as bismuth telluride (Bi_2Te_3), lead telluride (PbTe), and silicon germanium (SiGe) have maximum ZT's of approximately 1. Correspondingly, traditional TE semiconductors have efficiencies around 5% [1].

Contemporary TEGs built with semiconductors do not have overly complex designs. A "modern" TEG consists of numerous alternating n- and p-type paralellepipeds (called "legs") connected electrically in series with metal bands. Assemblies of legs are then placed between two electrically insulating, thermally conducting plates to create a module. This module is then connected to an external resistive load. As long as a

temperature gradient is maintained across the module, electrical power will be delivered to the load. See Figure 1 for a schematic of a TEG [1].

1.1. Thermoelectrics Background

The United States Deparment of Energy has called the development of more efficient thermoelectric materials a priority [5]. Greater efficiency, as noted above, requires that the ZT of TE materials be improved. Increasing ZT is not easy, though, as S, σ, and κ are interrelated [5], and in some materials (e. g. metals), the relationships between σ and κ is nearly constant [1].

The Wiedemann-Franz law states that, for metals at temperatures that are not extremely low, the ratio of thermal conductivity to electrical conductivity is directly proportional to temperature. The Wiedemann-Franz law is defined as [6]

$$\frac{\kappa}{\sigma} = \frac{\pi^2}{3}\left(\frac{k_B}{e}\right)^2 T \qquad (1.2)$$

where k_B is Boltzmann's constant, e is the charge per electron and T is the absolute temeperature [6]. The Wiedemann-Franz law is valid when the scattering of electrons is not dependent upon their energy.

Two investigative approaches for improving ZT have been followed since the 1990's: (1) increase the power factor of TE materials [11-13], which is the numerator of ZT ($S^2\sigma$), and (2) lower the thermal conductivity of TE materials [10, 14-15]. Efforts to improve power factor have focused on altering the density of electronic states for the mobile electrons. Efforts to lower thermal conductivity have focused on

Table 1-1—Seebeck coefficients, electrical conductivities, and thermal conductivities for selected modern thermoelectric materials.

Material	Temperature (K)	Seebeck Coefficient (μV/K)	Electrical Conductivity (S/cm)	Thermal Conductivity (W/m-K)	Ref.
n-type Bi_2Te_3	582	-247	70	1.92	[7]
p-type Bi_2Te_3	582	156	210	2.22	[7]
TAGS-85 $(AgSbTe_2)_{85}(GeTe)_{85}$	700	198	838	16.59	[8]
n-type SiGe	1200	-242	56	4.20	[9]
p-type SiGe	1100	237	34	4.38	[9]
LAST AgPbSbTe	700	-346	234	1.11*	[10]

*Point determined by linear interpolation. The points used for linear interpolation were located at (674, 1.15) and (723, 1.08) in Figure 3B from [10].

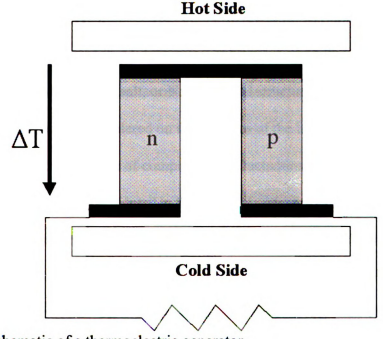

Figure 1-1—Schematic of a thermoelectric generator.

incorporating phonon scatterers into the material. In SiGe, the scatterers are Ge atoms in the Si matrix [5]. Also, recent research has been done on materials with cage-like structures that include rattling ions such as clathrates and skutterudites. Figure 2 shows a skutterudite crystal structure. Other recent research has been done on materials with nanoscopic features that act as phonon scatterers [8, 10, 16].

Two newly discovered thermoelectric semiconductor materials with high ZT's are doped lead tellurides [17]. LAST (lead-antimony-silver-tellurium) is an n-type semiconductor with a generic chemical formula of $AgPb_mSbTe_{2+m}$. LASTT (lead-antimony-silver-tin-tellurium) is a p-type semiconductor with a generic chemical formula of $Ag(Pb_{1-x}Sn_x)_mSbTe_{2+m}$ [17].

Earlier work suggested that LAST was a solid solution of PbTe and $AgSbTe_2$ [18-19]. Both materials have the rocksalt, or NaCl, crystal structure. As such, the Ag-Pb-Sb atoms would be statistically disordered on the Na sites of the lattice. However, LAST is actually nanostructured as a result of compositional fluctuations [20]. Theses nanostructures are quantum "nanodots" in the material. More specifically, these nanodots are Ag-Sb rich regions 2 to 4 nm across that are surrounded by a PbTe matrix [10, 20].

LAST is a noteworthy TE material because of its relatively high value of ZT. At 700 K, LAST (composition $AgPb_{18}SbTe_{20}$) has a reported ZT of 1.7 [10]. This high ZT value may be the result the nanodots in the material acting as phonon scatters, and, thusly, lowering LAST's thermal conductivity. Assuming a ZT of 2, a hotside temperature of 900 K, and a coldside temperature of 400 K, an efficiency of more than 18% may be possible [10].

Due to their relatively high ZT's at operating temperature gradients, LAST and LASTT have been of great research interest recently. Some of this research has focused on the mechanical properties of LAST and LASTT, including hardness, Young's modulus, and bend strength [21-23]. Especially noteworthy is the bend strength for LASTT ingots, which have grain sizes greater than 500 microns. The bend strength for LASTT ingot material is 15.3 MPa [21], which is rather low. (The bend strength of Al_2O_3, for comparison, can vary between 345 and 1035 MPa [24]. Also, this value is at the lower end of the strength values reported for semiconductors in Table 3-2.) The bend strength of LASTT and LAST, because they are brittle materials, can be improved by reducing the grain size of the material and thusly reducing the size of the critical flaws at which failure initiates.

One method by which the grain size, and flaw size population, can be reduced is to produce fine grained powders that are then densified to yield bulk specimens with small grain sizes. The work contained in this thesis describes efforts to produce powders with particle sizes on the order of a few microns, characterize these powders, and measure some of the properties bulk specimens manufactured from these powders.

2. Background

2.1. Powder Processing and Powder Characterization

Bulk thermoelectric (TE) materials can be produced by two techniques: solidified from a melt or powder processed. Of the two techniques, the former has generally been more popular [21, 25-26]. However, powder processing techniques have recently become of interest [27-32].

Powder processing of TE materials can be divided into two categories. One category involves the production of powders from ingots via milling; these powders are then densified by techniques such as cold pressing and sintering, spark plasma sintering [32], and hot pressing [27-31] to form bulk materials. The second category involves the production of TE powders by reacting the raw materials while milling. This is called mechanical alloying [33-36].

Cast TE materials—those solidified from a melt—typically have grain sizes on the order of hundreds of microns [21, 32, 37-39]. In brittle materials, such as common TE materials, fracture strength is a function of grain size because the critical flaws in the material (the fracture origins) scale in size with the material's grain size. So, brittle materials with larger grains have larger flaws. These larger flaws in turn require lower stress to initiate failure.

A brittle material's fracture strength can be increased by decreasing its grain size because the fracture strength of a brittle material is a function of the inverse square root

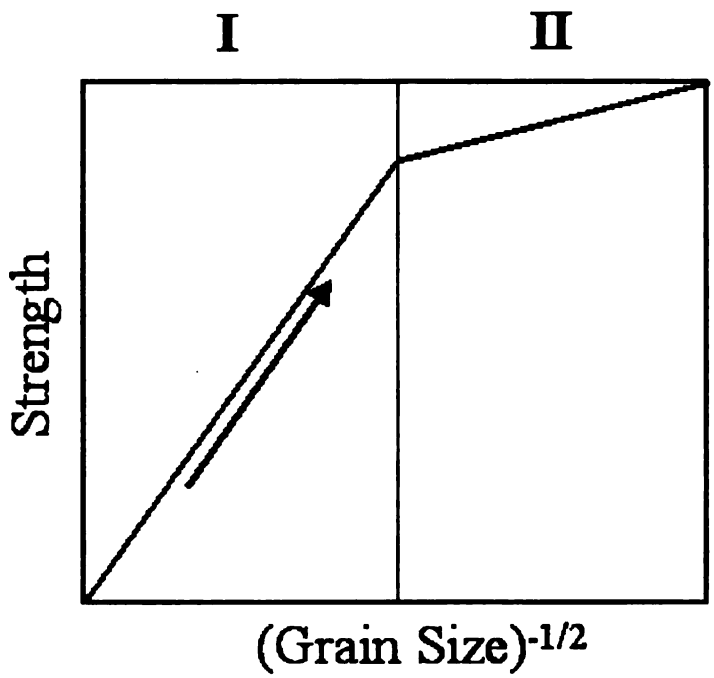

Figure 2-1—Schematic of strength as a function of grain size. Strength varies with the inverse square root of grain size. In region I, where the grains are "large," strength is a strongly correlated to grain size. In region II, where the grains are "small," strength is not as strongly correlated to grain size because the flaw size population is often dominated by surface flaws, including those introduced by grinding or polishing. Thus, in region II, the critical flaws at which failure initiates do not necessarily scale with grain size. The transition from region I to region II depends on the material of interest.

of grain size [40-41]. Reduced grain sizes can be achieved by manufacturing fine powders (powders with particle sizes on the order of microns). Using these fine powders one can produce fine grained bulk materials. With LAST and LASTT TE materials, combinations of dry and wet milling have been used to produce fine powders [42-43].

In some cases, ZT has also been improved by reducing a thermoelectric material's grain size. Jiang *et al* found that p-type $(Bi_2Te_3)_x(Sb_2Te_3)_{1-x}$ (where x was 0.16, 0.20, and 0.24), had a ZT of 1.08 when produced by zone melting. Spark plasma sintered material, which was comparatively finer grained, had a ZT of 1.15 [32]. Liu *et al* produced skutterudite $CoSb_3$ by a combination of mechanical alloying and spark plasma sintering. Specimens that were spark plasma sintered at 600 °C had a grain size of 300 nm and a peak ZT of 0.041 at a temperature of 151 °C. Specimens that were spark plasma sintered at 300 °C had a grain size of 50 nm and a peak ZT of 0.052 at a temperature of 403 °C [44].

Not only is the powder particle size important, but the particle size distribution, particle morphology, and contamination present in the powders also are important factors. As noted above, a small powder particle size allows for a small sintered grain size and the small grain size in turn enhances a material's strength. Likewise, as powder particle size decreases, sinterability increases. This increase in sinterability occurs because the driving force for sintering is proportional to particle curvature. As particle size decreases, the particle's curvature increases. With respect to particle size distribution, bimodal distributions that include very large particles (approximately 50

microns, for example) are undesirable because the large particles degrade a densified component's fracture strength.

Particle morphology is important because equiaxed, non-agglomerated powders pack the best in the green (unfired) state, which allows for more efficient sintering. Contamination during powder processing should be monitored since contaminants may form secondary phases that can potentially weaken the material or degrade its TE properties.

To characterize the powder particle size, size distribution, morphology and level of contamination, multiple complementary techniques have been used in this study. To measure powder particle size and particle size distributions, the Coulter counter technique has been employed. In addition to Coulter counter, Brunauer-Emmett-Teller (BET) analysis has been employed to indirectly gauge powder particle size. To observe powder particle morphology and qualitatively determine powder particle size, scanning electron microscopy (SEM) has been used. To monitor contamination and phases present, inductively coupled plasma mass spectrometry (ICP-MS) and x-ray diffraction have been employed.

2.2. Coulter Counter

The Coulter counter technique measures the number and size of particles suspended in an electrolyte solution. The technique was initially developed by Wallace Coulter to count blood cells [45]. Then, the Coulter principle was applied to particulate matter (dust from coal mines) by Anderson et al [46]. The techniques used by Anderson and his coworkers were further developed by Tomb and Raymond [47].

In the Coulter technique, the particles to be sized and counted are drawn through an aperture in the counter. The aperture is flanked on opposite sides by electrodes immersed in the same electrolyte. Between the electrodes, an alternating current is passed. When a particle passes through the aperture, it displaces an amount of electrolyte, which causes a change in the impedance between the electrodes. (It is assumed that only one particle passes through the aperture and between the electrodes at a given time.) As a result, voltage pulses are generated that are proportional to particles' volumes. From these voltage pulses, particles sizes are calculated and counted [48].

2.3. Mie Theory (Light Scattering)

Mie theory provides solutions to the problem of light scattering by small particles. Mie theory is a solution to Maxwell's equations, which are [49]

$$curlH = \frac{4\pi}{c} I + \frac{1}{c}\frac{dD}{dt} \tag{2.1}$$

$$curlE = \frac{-1}{c}\frac{dH}{dt} \tag{2.2}$$

and

$$divI + \frac{d\rho}{dt} = 0 \tag{2.3}$$

where E is the electric field strength, H is the magnetic field strength, D is the dielectric displacement, and I is the current density. The dielectric displacement, D, is defined as εE, where ε is dielectric constant. The current density, I, is defined as σE, where σ is the

electrical conductivity. The other variables, c and t, are the speed of light and time, respectively.

Mie theory models a plane electromagnetic wave scattered by a homogeneous sphere. Both the medium outside the sphere and the sphere itself have their own complex refractive index (having both a real part, n, and an imaginary part, k), denoted by m (m_1 is the complex refractive index for the sphere and m_2 is the complex refractive index for the medium). The incident radiation is assumed to be linearly polarized. For the solution, the origin of the coordinate system is typically set as the center of the sphere, and the positive z-axis is along the propagation direction of the incident wave and the x-axis is in the incident wave's plane of electric vibration.

With the above conditions set, and the amplitude of the incident wave set to 1, the incident wave is described by [49]

$$E = a_x e^{-ikz+i\omega t} \tag{2.4}$$

and

$$H = a_y e^{-ikz+i\omega t} \tag{2.5}$$

where a_x is the unit vector along the x-axis, a_y is the unit vector along the y-axis, k is the propagation constant, and ω is the angular frequency. The propagation constant, k, is defined as $2\pi m_2/\lambda_{vac}$, where λ_{vac} is wave length of the incident wave in a vacuum.

The solution to the Mie problem are the coefficients a_n and b_n, which are [49]

$$a_n = \frac{\psi_n'(y)\psi_n(x) - \frac{m_1}{m_2}\psi_n(y)\psi_n'(x)}{\psi_n'(y)\zeta_n(x) - \frac{m_1}{m_2}\psi_n(y)\zeta_n'(x)} \tag{2.6}$$

$$b_n = \frac{\frac{m_1}{m_2}\psi_n'(y)\psi_n(x) - \psi_n(y)\psi_n'(x)}{\frac{m_1}{m_2}\psi_n'(y)\zeta_n(x) - \psi_n(y)\zeta_n'(x)} \tag{2.7}$$

In the equations for a_n and b_n, ψ_n is a modified Bessel function of the first kind, ξ_n is a modified Bessel function of the third kind, and the primes of these functions are the first time derivatives. The argument x is defined as $2\pi a m_2/\lambda_{vac}$, where a is the radius of the sphere. The argument y is defined as $2\pi a m_1/\lambda_{vac}$.

Once a_n and b_n are known, the wave vectors for the scattered wave outside the particle can be calculated. The wave vectors, u and v, are given by [49]

$$u = e^{i\omega t}\cos\varphi\sum_{n=1}^{\infty} -a_n(-i)^n \frac{2n+1}{n(n+1)} P_n^1(\cos\theta) h_n^{(2)}(kr) \tag{2.8}$$

and

$$u = e^{i\omega t}\sin\varphi\sum_{n=1}^{\infty} -b_n(-i)^n \frac{2n+1}{n(n+1)} P_n^1(\cos\theta) h_n^{(2)}(kr) \tag{2.9}$$

Where θ and φ are the spherical coordinate angles, $P_n^1(\cos\theta)$ is a Legendre polynomial, and $h_n^{(2)}(kr)$ is a spherical Bessel function.

As stated above, Mie theory models scattering by a sphere. It will be observed later in this thesis that the powders sized through application of Mie theory are not spherical. As noted in [50], the scattering of light by non-spherical particles is a problem that still requires work. For irregularly shaped Fe_2O_3 and TiO_2 particles, which have relatively high values for the real part of the refractive index, the measured scattering data and the scattering predicted by Mie theory agreed well [51]. Jurewicz *et al* found that for powdered limestone composed of spheroidal particles, Mie theory most accurately modeled light scattering [52]. However, for irregularly shaped quartz particles, Curtis *et al* found that Mie theory overestimated the light scattering [53].

2.4. BET Surface Area Analysis

BET (Brunauer-Emmett-Teller) testing, is a technique by which size information for very fine powders can be determined. BET analysis determines a powder sample's total surface area. Surface area varies inversely with powder particle size, so a larger surface area denotes a smaller average particle size. Also, if particle morphology is assumed, and the powder's mass density is known, an equivalent average particle size can be calculated.

BET analysis is based on a theory published by Brunauer *et al* in 1938. This theory assumes that multimolecular adsorption is caused by the same forces that cause condensation. The theory says, at equilibrium, the rate of condensation on the surface of layer s_{i-1} is equal to the rate of evaporation from layer s_i. This condition is described by equation 2.10 [54].

$$a_i p s_{i-1} = b_i s_i \exp\left(\frac{E_i}{RT}\right) \tag{2.10}$$

In equation 2.10, a_i and b_i are constants, p is pressure, s_i is the surface area covered by the *i*th layer of adsorbed molecules, E_i is the heat of adsorption for the *i*th layer, R is the Universal Gas Law constant, and T is the temperature. Additionally, a_i, b_i, and E_i are assumed to be independent of the number of molecules already adsorbed in layer s_i. Also, equation 2.10 is similar in form to Langmuir's equation for unimolecular adsorption.

Through algebraic manipulation, equation 2.10 yields equation 2.11 [54].

$$\frac{p}{v(p-p_0)} = \frac{1}{v_m c} + \frac{c-1}{v_m c}\frac{p}{p_0} \tag{2.11}$$

In equation 2.11, p is pressure, v is the total volume of adsorptive adsorbed, p_0 is the saturation pressure for the adsorptive, v_m is volume of gas adsorbed when the entire sample surface is covered with a complete unimolecular layer, and c is given by equation 2.12 [54].

$$c = \frac{a_1 g}{b_1}\exp\left(\frac{E_1 - E_L}{RT}\right) \tag{2.12}$$

In equation 2.12, R and T are the same as described for equation 2.10. The variables a_1 and b_1 are the constants from the first equation in the form of equation 2.10. E_1 is the heat of adsorption for the molecular first layer. The variable g a constant based on the assumption that beyond the first adsorbed layer, the ratio of b_i to a_i does not change, i.e $g = b_2/a_2 = b_3/a_3 = \ldots b_i/a_i$. Similarly, E_L is the heat of liquefaction for the adsorptive,

which is assumed to be equal to the E_i, and E_i is assumed to be equal to the heat of adsorption for all layers proceeding layer where i = 1; i.e. $E_2 = E_3 = \ldots E_i = E_L$.

Equation 2.11 models the case where an infinite number of unimolecular layers may adsorb to the surface. This means that for a powder sample, it is assumed that the powder particles are not in contact with one another. If a finite number of molecular layers can adsorb to the surface the BET equation changes. Specifically, a term for the finite number of molecular layers that can adsorb is added and the equation becomes [54]

$$v = \frac{v_m cx}{(1-x)}\left[\frac{1-(n+1)x^n + nx^{n+1}}{1+(c-1)x - cx^{n+1}}\right] \tag{2.13}$$

Equation 2.11 is convenient since plotting $p/[v(p-p_0)]$ on the ordinate versus p/p_0 on the abscissa gives a straight line with an intercept of $1/v_m c$ and slope $(c-1)/v_m c$. Using the data from the plot, the volume of a complete unimolecular adsorbed layer, v_m, may be calculated. Once v_m has been determined, the total surface area and then the specific surface area of the sample may be determined based on the area that each adsorbed molecule covers [54].

2.5. Inductively Coupled Plasma Mass Spectrometry (ICP-MS)

At the heart of inductively coupled plasma (ICP) analytical techniques is the plasma, which is an electrical discharge that is like a flame. The plasma is formed from argon (Ar) gas. A stream of Ar gas flows through the torch, which is composed of three concentric quartz tubes. At the end of the torch is the copper induction coil, which is connected to a radiofrequency generator. The radiofrequency generator typically operates at frequencies of 27 or 40 MHz at output powers between 1 and 2 kW. In the Ar

gas, a current is generated by the magnetic field that results from the radiofrequency current passing through the induction coil. Seeding the Ar gas with energetic electrons produced by a Tesla discharge or a piezoelectric transducer forms the plasma. As long as the Ar flows symmetrically and the magnetic field maintains a sufficient strength, the plasma is both stable and self-sustaining [55]. Figure 2-2 is a schematic of an ICP.

ICP spectrometries are popular analytical techniques for four principle reasons: (1) very low detection limits, (2) high precision (0.2-0.3% relative standard deviation), (3) the capability to detect almost all elements, and (4) concentration ranges for most elements spanning four to eleven orders of magnitude. Another benefit to ICP spectrometries is that there is little interelement interference compared to flame, arc, and spark spectrometry techniques [55]. Interferences can arise from the formation of refractory compounds, which then reduce the emission of certain ions [56].

In ICP-MS, the sample is typically in liquid form as some kind of solution. The first step in the analysis is to pump this liquid into the sample introduction system [57]. In the sample introduction system, the sample is turned into an aerosol by a nebulizer [58] and injected into the base of the plasma [57]. As the sample passes through the plasma, it is successively dried, vaporized, atomized, and ionized. The atoms and ions from the sample then reach the analytical zone of the plasma, where the mass spectroscopy is completed [57]. If the plasma begins where the sample is injected and ends at a tip, the analytical zone of the plasma starts at approximately the midpoint and extends to roughly the three-quarter mark of the plasma [55].

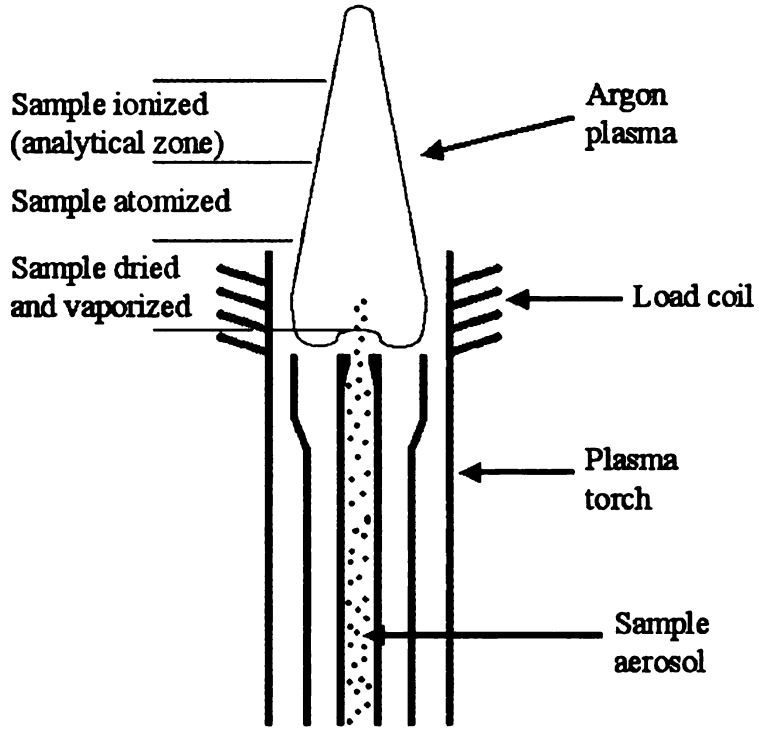

Figure 2-2—Schematic of an ICP.

3. A Review of Mechanical Properties for Thermoelctric Materials

The mechanical property database for thermoelectric (TE) materials is very limited. A review of the mechanical property data in the open literature for TE materials is useful for several reasons. It provides a resource for the stress-strain response, fracture, and reliability of individual TE materials. Additionally, it establishes a range of mechanical property values that are common to most TE materials. Thirdly, it allows comparison to other semiconducting materials.

With grants from the Office of Naval Research and the Department of Energy, work has been done at Michigan State University to develop LAST and LASTT materials for use in thermoelectric generators. LAST is an n-type TE composed of lead, antimony, silver, and tellurium. LASTT is a p-type TE composed of lead, antimony, silver, tin, and tellurium. The properties of LAST and LASTT will be compared to other TE's and other semiconductors.

Why is it important to consider the mechanical properties of TE materials? In the applications of TE materials, thermo-mechanical stresses are generated. In waste heat recovery applications, these stresses arise from thermal gradients across the TE element (which will exist in all TE applications), mechanical vibrations, and thermal expansion mismatch stresses among the TE module components (legs, electrical interconnects, mounting plates, etc.). As a result of these stresses, microcracks and macrocracks can form. The cracks and microcracks can in turn lead to the failure of the TE material. How TE materials respond to the applied stresses are a function of the material's microstructure.

In this review, data on the hardness [22-23, 26, 30, 59-63], Young's modulus [1, 25, 27, 29, 62-64], bend strength and Weibull modulus [21, 27-28, 31-32, 38, 62, 64-72], and fracture toughness [27-28, 30] for common TE materials will be presented.

Primarily, the materials reviewed will be PbTe [25-26, 59, 62], LAST/LASTT [21-23, 29, 62], Zn_4Sb_3 [27-28, 30], and Bi_2Te_3 [31-32, 38, 60, 64-69, 71-72]. Very limited data for TAGS ($(GeTe)_{1-x}(AgSbTe_2)_x$) [61], SiGe [9], and $Bi_{85}Sb_{15}$ [70] will also be presented. Unfortunately, no data for skutterudites, clathrates, and half and full Heusler compounds will be shown because none could be found in the open literature.

The materials reviewed were produced by many different techniques. Polycrystalline specimens were prepared by techniques including casting [25-26], extrusion [38, 70-72], hot pressing [27-31, 62], and spark plasma sintering [32]. Single crystal specimens were prepared by the Czochralski [60, 64-68, 71], Bridgman, and floating crucible [69] methods.

Just as the materials were prepared by various methods, many different techniques were used to measure materials' mechanical properties. The elastic moduli were measured by indentation [23], and the ultrasonic pulse-echo technique [29]. Hardness was measured via Vickers indentation [22, 25, 27, 30, 59, 62]. Bend strength data came from three-point bend [27-28, 32, 38, 60, 65, 67, 72] and biaxial flexure [21, 62] tests. Single-edge notched beam tests were done to measure fracture toughness [27-28].

3.1. Hardness

Hardness data was found for PbTe, LAST, Zn_4Sb_3, Bi_2Te_3, and TAGS. Except for Zn_4Sb_3, the hardness of common TE materials is less than 1 GPa. The reported

hardness for zinc antimonide is 2.24 GPa [30]. For PbTe, hardness falls between 0.339 [26] and 0.451 [59] GPa. For LAST, the hardness data ranges from 0.526 to 0.964 GPa [22]. For Bi_2Te_3, the hardness data ranges from 0.253 to 0.679 GPa [60]. For TAGS, the hardness falls between 0.098 and 0.215 GPa [61]. Figure 3-1 shows the hardness data found in the open literature.

For the materials presented in Figure 3-1, there is limited microstructural information. No microstructural information is reported for PbTe [25-26, 59,]. In [30], Ur *et al* reports the the Zn_3Sb_4 specimens tested were comprised of the ε and β phases of Zn_3Sb_4 as well as Zn. Ur *et al* also states that the specimen densities ranged between 96.5 and 103.2% of theoretical (the densities exceeding 100% are explained by the presence of extra Zn in the material) [30]. From [60], the only information given is that the Bi_2Te_3 specimens are single crystals. In [61], the TAGS specimens are nearly theoretically dense (approximately 97% dense). The actual porosity may be less than 3% because cracks were present in all the specimens [61].

Both Darrow [25] and Rogacheva [26] present data for doped PbTe (Figure 3-2). Darrow [25] substituted S and Se for Te, while Rogacheva [26] substituted Sn, Ge, Cd, In, Bi, and Ga for Pb. With S additions ranging between 0 and 5 mol%, the hardness increased from 0.43 to 0.72 GPa [25]. With Ga additions ranging between 0 and 0.4 mol%, the hardness almost doubled, increasing from 0.34 to 0.59 GPa [26].

3.2. Young's Modulus

Young's Modulus data was found for PbTe [62], LAST [23, 29], Zn_4Sb_3 [27], Bi_2Te_3 [64], and SiGe [9] (Figure 3-3). Expept for SiGe [9], Young's Modulus for TE

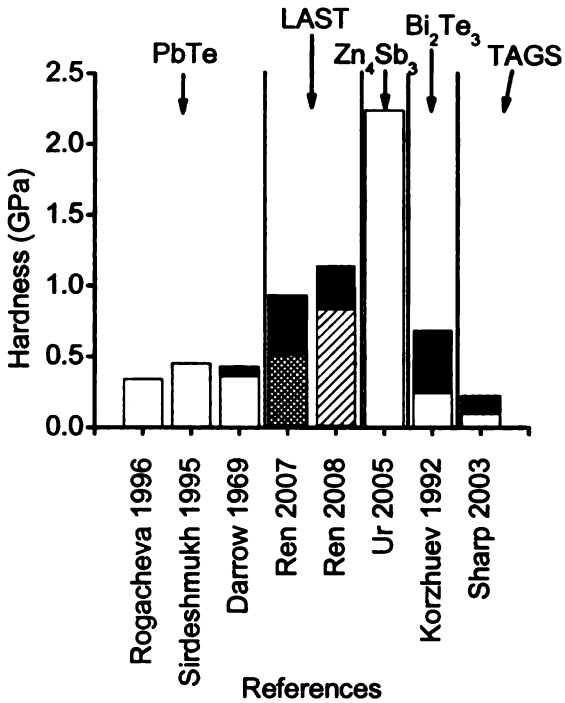

Figure 3-1—Hardness data for common TE materials. The colored portions of the bars represent the range in reported values. For LAST, data for both ingot material (left) and hot pressed specimens (right) are presented [22, 25-26, 30, 59-61].

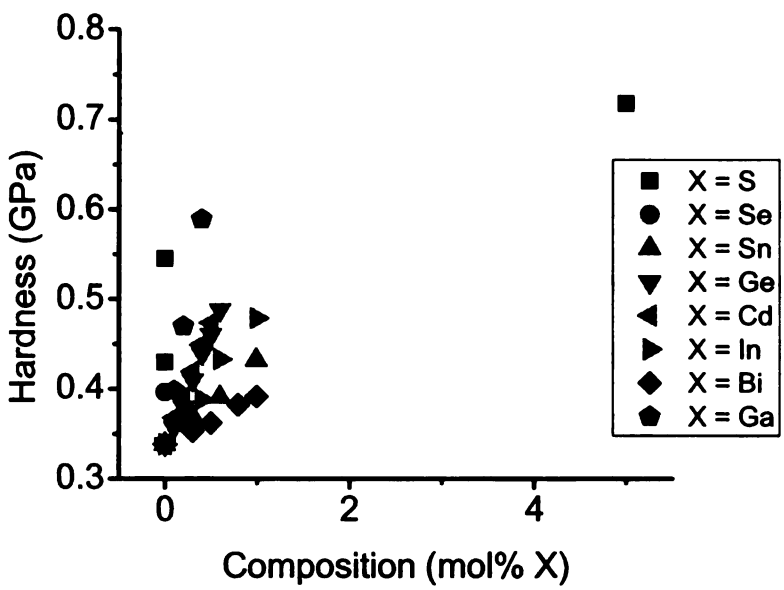

Figure 3-2—Hardness of lightly doped (<1 mol%) PbTe [25-26]. Notice that the addition of certain elements, especially sulfur and gallium, dramatically increased hardness [25-26].

materials is less than 80 GPa. Young's Modulus for SiGe is between 137 and 145 GPa [9]. From the aggregate data for single crystal PbTe, the Young's modulus was estimated to be 58 GPa [62]. For LAST, the reported values range from 24.6 to 71.2 GPa [23]. For Zn_4Sb_3, Young's modulus ranges from 57.9 to 76.3 GPa [27]. For Bi_2Te_3, the only reported Young's Modulus is 40.4 GPa [64].

Interestingly, the Young's modulus as a function of composition for LAST from Kosuga et al [29] and Ren et al [23] measurements compare relatively well (Figure 3-4). The values of Young's modulus reported by Kosuga et al [29] range between 27.6 and 54.2 GPa. From microindentation measurements, Ren et al [23] reported Young's modulus values between 24.5 and 68.5. From nanoindentation measurements, Ren et al reported Young's modulus values between 25.8 and 71.2 GPa [23].

Although their measurements are similar, there are important differences between the materials and techniques used in both papers. Kosuga et al's [29] specimens were prepared by hot pressing and measured by ultrasonic pulse-echo. Ren et al's specimens [23] were cast and measured by microindentation and nanoindentation. It is important to note that the data from Kosuga [29] is across a much smaller range of compositions than that the data from Ren [23]. The differences in composition range can be seen by comparing Figure 3-4 and Table 3-1.

3.3. Bend Strength

Bend strength data was found in the open literature for LASTT [21], LAST, Zn_4Sb_3 [27-28], and Bi_2Te_3 [31-32, 38, 64-72] (Figure 3-5). Despite extensive efforts, no information on the bend strength of PbTe was located in the open literature.

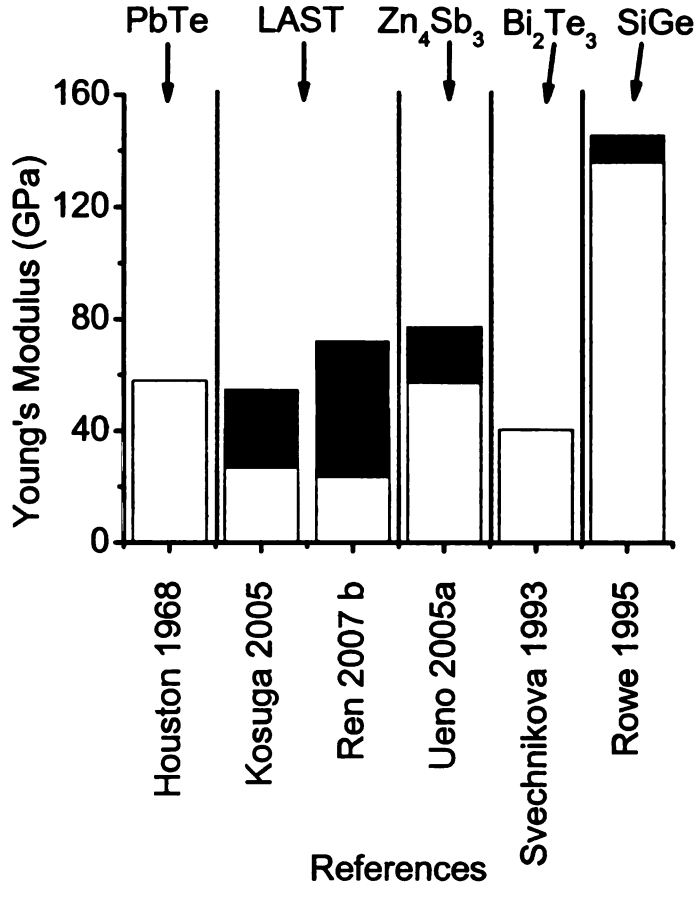

Figure 3-3—Young's modulus for different TE materials. The colored portions of the bars show the range in the reported data [9, 23, 27, 29, 63-64].

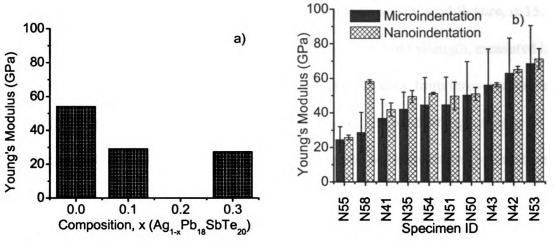

Figure 3-4—Young's modulus data from (a) Kosuga et al [29] and (b) Ren et al [23].

Table 3-1—Ingot compositions for specimens in [23]. Notice there is a wide compositional variation among the specimens.

Ingot	Ag	Pb	Sb	Te
N35	1.0	10	0.8	11.6
N41	0.4	22	1.0	24
N42	0.43	18	1.2	20
N43	0.43	18	1.2	20
N50	0.5	26	0.87	27.73
N51	0.5	14	1.067	16.13
N53	0.95	30	1.05	32.1
N54	1.0	20	0.8	11.6
N55	0.4	10	1.2	12.4
N58	0.43	18	1.2	20

The bend strength of TE materials ranges from less than 25 MPa [21] to more than 150 MPa [72]. For LASTT, the bend strength, measured by biaxial flexure, is 15.3 MPa [21]. For LAST (composition $Ag_{0.86}Pb_{19}Sb_{1.0}Te_{20}$), the bend strength, measured by biaxial flexure, is 51.6 MPa [62]. For Zn_4Sb_3, bend strength data, from three-point bend tests, ranges from 56.4 [27] to 83.4 [28] MPa. For Bi_2Te_3, the bend strength ranges broadly from 8 [65] (measured by three-point bend) to 166 MPa (measured by three-point bend) [72].

Figure 3-5 contains several points that warrant closer inspection. First, the LASTT data are from a Weibull study of ingot material [21]. In comparison, the LAST data are from hot pressed specimens. Like the LAST (composition $Ag_{0.86}Pb_{19}Sb_{1.0}Te_{20}$) data [62], the values reported for Zn_4Sb_3 are for hot pressed material [27-28]. Lastly, one may notice that there are very large ranges in the data for Bi_2Te_3 [31-32, 38, 65-69, 71-72]. These large ranges in data may be partly caused by the structure of Bi_2Te_3, which is layered and very anisotropic [60, 65, 67].

Some of the data from the literature demonstrates how reducing grain size can dramatically increase bend strength (Figure 3-6). In [32], the bend strength of Bi_2Te_3 increased from less than 20 MPa for zone melted ingots to roughly 80 MPa for spark plasma sintered specimens made from powders ranging in size from 96 to 120 microns in diameter. (Powder particle sizes between 96 and 120 microns are relatively large, though.)

Similar improvements are seen in $Bi_{85}Sb_{15}$ specimens tested at 77 K and 293 K [70]. For tests conducted at 77 K, polycrystalline $Bi_{85}Sb_{15}$ had a three-point bend strength of 90 MPa, compared to 10 MPa for single crystal specimens [70].

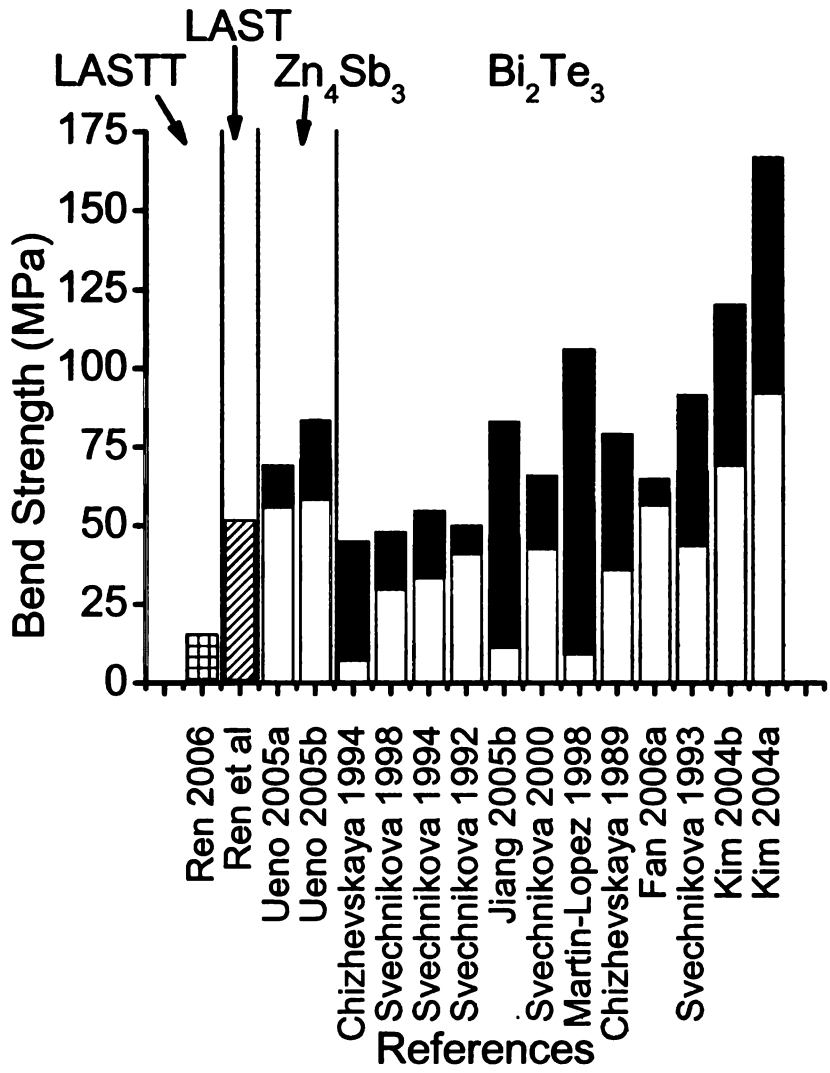

Figure 3-5—Bend strength of different TE materials. Colored portions of the bars show the range in the reported data [21, 27-28, 31-32, 38, 64-72].

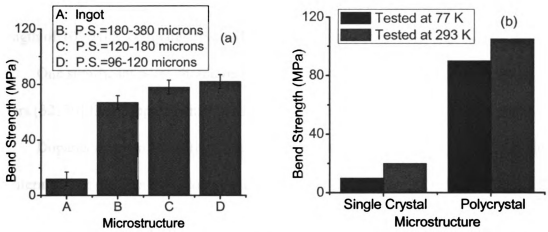

Figure 3-6—Bend strength versus microstructure for (a) Bi_2Te_3 [32] and (b) $Bi_{85}Sb_{15}$ [70] [32, 70].

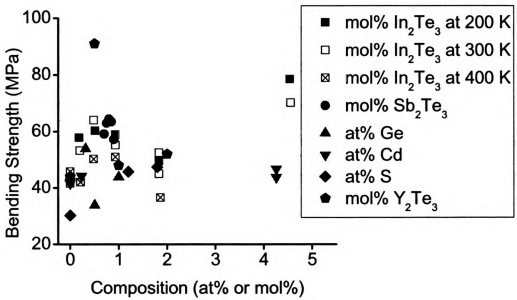

Figure 3-7—Effect of dopant concentration on the bend strength of Bi_2Te_3. Notice that bend strength either increases monotonically or goes through a maximum as doping increases [31, 64, 66-68, 71].

For tests conducted at 293 K, polycrystalline $Bi_{85}Sb_{15}$ had a three-point bend strength of 105 MPa, compared to 20 MPa for single crystal specimens [70].

One significant point should be noted for the data from [32] and [70]. Both papers [32, 70] fail to report a final grain size for the specimens tested.

Dopants can also affect the three-point bend strength of Bi_2Te_3 (Figure 3-7). In the literature, Bi_2Te_3 has been doped with In_2Te_3 [71], Sb_2Te_3 [31], Ge [67], Cd [68], S [66], and Y_2Te_3 [64]. Two trends with dopant addition are noticeable. First, as with the addition of S, the bend strength increases monotonically [66]. Second, as with the addition of Y_2Te_3, the bend strength goes through a maximum (91 MPa specifically) [64].

3.4. Fracture Toughness

The fracture toughness of hot pressed Zn_4Sb_3 ranges from 0.6 [27] to 1.5 [30] MPa-$m^{1/2}$ (Figure 3-8). Despite a thorough search of the open literature, Zn_4Sb_3 was the only TE material for which fracture toughness data could be found. The fracture toughness of Zn_4Sb_3 can vary significantly, as seen in the data from Ur [30]. In Ur [30], the data ranges from less than 0.8 to more than 1.5 MPa-$m^{1/2}$.

3.5. Comparing Mechanical Properties for Selected Semiconductors and TE's

As most thermoelectric materials currently in use are semiconductors [1-2], it is reasonable to compare the mechanical properties of TE's and other semiconductors. Table 3-2 summarizes the room temperature mechanical properties for four selected semiconductors and PbTe, LAST/LASTT, Zn_4Sb_3, and Bi_2Te_3.

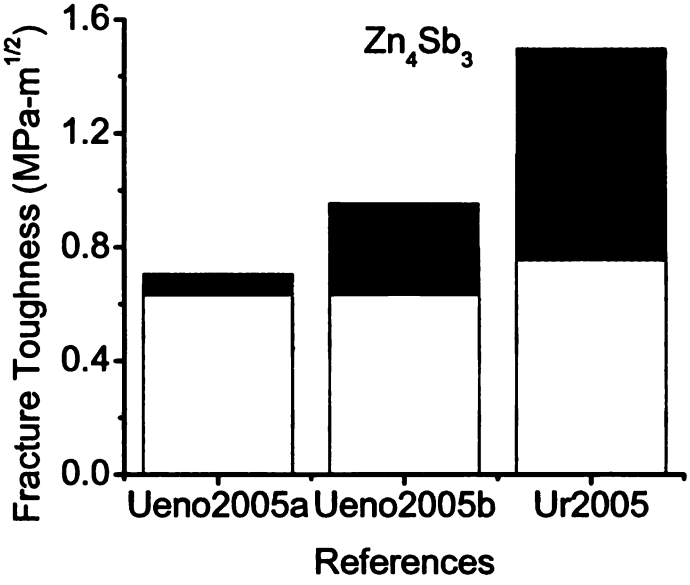

Figure 3-8—Fracture toughness of Zn_4Sb_3. The colored portions of the bars represent the range in the data. All of the data is for hot pressed material [27-28, 30].

The similarities and differences among the mechanical properties of selected TE materials can be significant (Table 3-2). All the mechanical properties for the first three semiconductors—Si, Ge, and GaAs—compare well. The only noteworthy discrepancies among the three are the maximum fracture strength of Ge [73] and the low fracture strength of GaAs [74]. However, when Si [75-78], Ge [73, 78-79] and GaAs [78-80] are compared to the common TE's discussed above [21-23, 26-28, 30, 59-60, 62, 64-65, 81], striking differences are seen. The hardness, Young's modulus, and fracture strength of PbTe, LAST/LASTT, Zn_4Sb_3, and Bi_2Te_3 [21-23, 26-28, 30, 59-60, 62, 64-65, 72] are much lower than for Si [75-77], Ge [73, 79], and GaAs [74, 79-80]. Also, the coefficients of thermal expansion for TE's (narrow band gap semiconductors) [81] are typically greater than for wide band gap semiconductors [78].

Despite the general dissimilarity in the mechanical properties of traditional semiconductors and TE's (Table 3-2), this is not always the case. ZnSe is a semiconductor whose mechanical properties more closely match those of TE's [82-84]. Though not exactly the same, the hardness [82], Young's modulus [83], and fracture strength [84] of ZnSe are within a factor of three to the values for PbTe [26, 59, 62], LAST/LASTT [21-23], Zn_4Sb_3 [27-28, 30] and Bi_2Te_3 [60, 64-65, 72]. Especially close are the values of hardness [22, 62], Young's modulus [23], and fracture strength [62] for LAST and ZnSe [82-84].

The selected semiconductors ZnSe and Si are widely used today. It is important to note that ZnSe is used in light emitting diodes (LEDs) [85-86], while Si is used in computers. As noted above, the elastic moduli [83], hardness [82], and fracture strength [84] of ZnSe are close (within a factor of three) to those for LAST [22-23, 62]. However,

Table 3-2—Room temperature mechanical properties for selected semiconductors and thermoelectrics [21-23, 26-28, 30, 59-60, 62-65, 72-84, 87].

Material	Hardness (GPa)	Young's modulus (GPa)	Poisson's ratio	Fracture Toughness (MPa-$m^{1/2}$)	Fracture Strength (MPa)	CTE (10^{-6}/K)
Si	9[75]	163[76]	0.22[76]	0.7[75]	247[77]	2.56[78]
Ge	9.2[79]	128[79]	0.21[73]	0.60[79]	231-392[73]	5.9[78]
GaAs	6.52[80]	117[79]	0.24[79]		66[74]	6.86[78]
PbTe	0.34[26]-0.45[59]	58[63]	0.26[77]			19.8[81] 20.4[81]
LAST, LASTT	0.53[22]-1.20[62]	24.6-71.2[23]	0.24-0.28[91]		15.3[21]-51.6[62]	20.6-23.4[91]
ZnSe	1[82]	76.1[83]	0.29[83]		~60[84]	8.5 (293-573 K)[87]
Zn_4Sb_3	2.24[30]	57.9-76.3[27]		0.64[27]-1.49[30]	56.6[30]-83.4[28]	
Bi_2Te_3	0.25-0.68[60]	40.4-46.8[64]			8[65]-166[72]	14.4 ($\perp$)[81] 21.3 ($\parallel$)[81]

ZnSe is not used in a thermal gradient or in environments with large thermal transients. As a result, the in-service mechanical stresses experienced by ZnSe are likely lower than those experienced by LAST.

Likewise, a point can be made with respect to the Weibull modulus of LASTT ingots and p-type Si wafers. (The Weibull modulus, m, is a measure of the scatter of fracture strengths within a specimen population [88].) The Weibull modulus for LASTT ingots was 3.2 [21], which is relatively low and indicates considerable scatter in strength. However, for commercial (100) p-type Si wafers, 525 microns, thick tested in air, the Weibull modulus was 3.5 [77]. The m-values for LASTT ingots [21] and Si wafers [77] are quite similar.

3.6. Conclusions

From this review of the mechanical properties for common thermoelectric materials, several important conclusions can be drawn. First, except for Zn_4Sb_3, the hardness of TE materials is less than 1 GPa (Figure 3-1, Table 3-2). Second, except for SiGe, the Young's modulus of TE materials is less than 80 GPa (Figure 3-3, Table 3-2). Third, TE materials typically have bend strengths, measured by three-point bend or biaxial flexure, between 25 MPa and 150 MPa (Figure 3-5, Table 3-2). Fourth, the hardness, Young's modulus, and bend strength of common TE materials are relatively low compared to many other brittle materials (Table 3-2).

In comparing the mechanical properties of LAST/LASTT to ZnSe and Si, some things should be noted. ZnSe [82-84] and LAST [22-23, 62] have similar mechanical properties, but ZnSe's application as an LED [85-86] is likely a mechanically less

demanding application than materials for thermoelectric generators. Similarly, the measured Weibull modulus for LASTT ingots [21] and commercial Si wafers [77] compare very well, but, again, the mechanical demands on TE generator materials are likely much more severe than experienced by Si wafers.

So, the mechanical properties of LAST and LASTT are similar, in some aspects, to widely used semiconducting materials (Table 3-2). Thus, the use of LAST and LASTT in real applications seems feasible. However, the demanding thermo-mechanical environment for thermoelectric generators is a challenge.

4. EXPERIMENTAL PROCEDURES

4.1. Materials

Ingots of LAST (lead-antimony-silver-tellurium) and LASTT (lead-antimony-silver-tellurium-tin) were prepared by Ed Timm (Mechanical Engineering Department, Michigan State University). LAST ingot production began by measuring the proper amounts of lead (four nines pure, Superpure Chemetals, Florham Park, NJ), antimony (five nines pure, Cerac, Milwaukee, WI), silver (four nines pure, Royal Canadian Mint, Ottawa), and tellurium (five nines pure, Cerac, Milwaukee, WI). For LASTT ingots, the tin was 99.999% pure and came from Kurt J. Lesker Company, of Pittsburgh, PA. The elemental materials were then placed into a silica ampoule 25 mm in diameter. With the raw materials inside the ampoule, it was evacuated and sealed.

The elemental materials were then melted and subsequently cooled in a three-zone split-tube rocking furnace (Applied Test systems, Inc. Butler, PA). The exact thermal profile used in the production of the ingots varied. Table 4-1 lists the ingots used to make the specimens referred to in this writing and the associated thermal profiles. Figure 4-1 is a plot of each of the thermal profiles listed in Table 4-1.

4.2. Specimen Preparation

4.2.1. Mounting in Epoxy

Before mounting a specimen in epoxy, the specimen's mass density was first determined. To calculate the mass density, the dimensions and mass of the parallelepiped specimens was measured. Nominally, these specimens were 5 mm x 5 mm x 7 mm. Each dimension was measured three times using calipers, and the mean was calculated. The mass for each leg was measured once using an electronic balance (OHAUS

Table 4-1—LAST and LASTT ingots used to make the specimens in this writing and each ingot's thermal profile.

Thermal Profile	Ingots	Composition
A	P20	$Ag_{0.5}Pb_6Sn_2Sb_{0.2}Te_{10}$
B	P41, P45	$Ag_{0.9}Pb_9Sn_9Sb0.6Te_{20}$
C	N59	$Ag_{0.43}Pb_{18}Sb_{1.2}Te_{20}$
D	N102	$Ag_{0.43}Pb_{18}Sb_{1.2}Te_{20}$
E	N104	$Ag_{0.43}Pb_{18}Sb_{1.2}Te_{20}$
F	N120	$Ag_{0.43}Pb_{18}Sb_{1.2}Te_{20}$
G	N124	$Ag_{0.43}Pb_{18}Sb_{1.2}Te_{20}$
H	N126, N129, N130	$Ag_{0.43}Pb_{18}Sb_{1.2}Te_{20}$
I	N155, N158	$Ag_{0.86}Pb_{19}Sb_{1.0}Te_{20}$
J	N156	$Ag_{0.86}Pb_{19}Sb_{1.0}Te_{20}$
K	N166	$Ag_{0.86}Pb_{19}Sb_{1.0}Te_{20}$
L	N170, N171, N172, N177, N182	$Ag_{0.86}Pb_{19}Sb_{1.0}Te_{20}$
M	P38	$Ag_{0.9}Pb_9Sn_9Sb0.6Te_{20}$

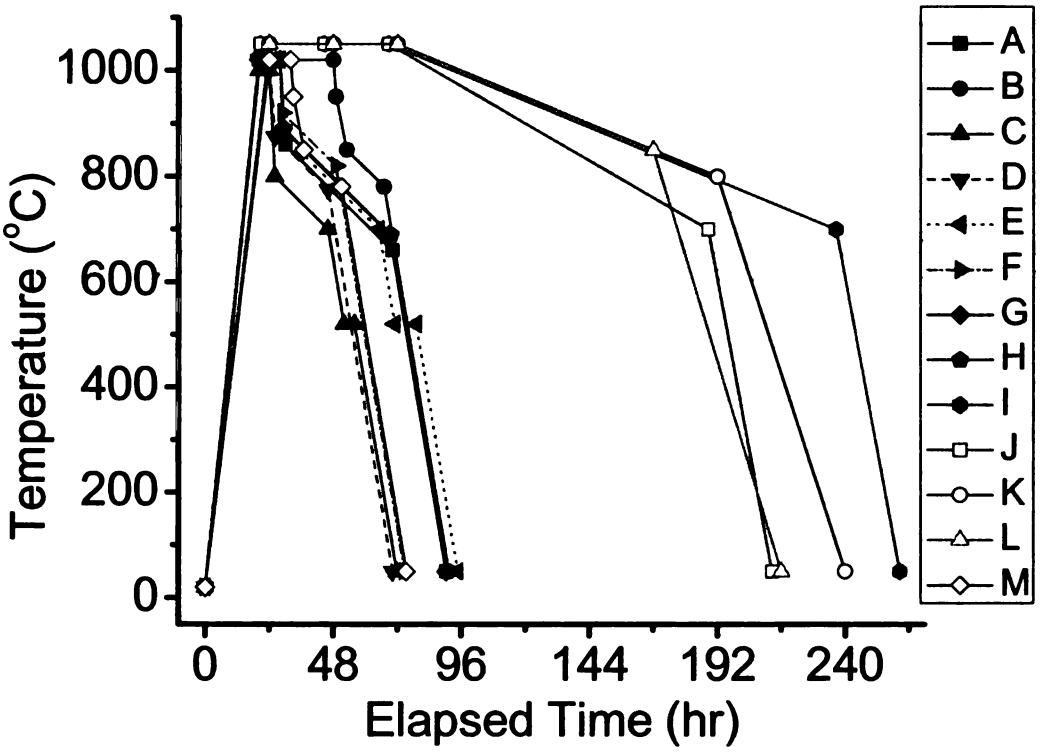

Figure 4-1—Plot of thermal profiles mentioned in Table 4-1.

Adventerer, AR2140, OHAUS Corp., Pine Brook, NJ). The mass density was then calculated by dividing the leg's mass by the specimen's volume in cubic centimeters. Lastly, each leg was labeled with a felt-tipped marker.

After computing the specimen density, the actual mounting process began. First, the surface where the epoxy is allowed to cure was scraped smooth using a razor blade. Then, one phenolic mounting ring, 2.5 cm in diameter and 2 cm long, (LECO Corporation, St. Joseph, MI) for each specimen was removed and placed near the curing surface. With preparations complete, the epoxy resin (Epoxicure Resin, 20-8130-032, Buehler Ltd., Evanston, IL) and hardener (Epoxicure Hardener, 20-8132-008, Buehler Ltd., Evanston, IL) were thoroughly mixed in a ratio, by weight, of five parts resin to one part hardener using a wooden tongue depressor. While mixing, care was taken not to stir any air bubbles into the epoxy. After mixing the epoxy, the curing surface was sprayed with release agent (Crown #3470 Reliable Release, North American Professional Products, Woodstock, IL). The specimens for mounting were placed on the curing surface, and phenolic rings were placed around the specimens so that the specimens were centered inside the rings. The specimens and phenolic rings were positioned on the curing surface so that a gap at least 0.5 cm wide existed between the phenolic rings. The epoxy was then poured into each phenolic ring so that the specimen was completely covered with epoxy. Once all the specimens were immersed in epoxy, any remaining epoxy was added to the phenolic rings. Finally, a weight with a flat side was placed on top of the phenolic rings and the epoxy was left to cure.

After the 24 hours, the weight was removed and the phenolic rings containing the hardened epoxy and specimens were torqued until they came free from the mounting

surface. Each specimen then had its designation written into the epoxy using a Dremel (Dremel 300 Series High Speed Rotary Tool, Robert Bosch Tool Corp., Racine, WI).

4.2.2. Polishing

Initial polishing was done on an Automet 3 Variable Speed Grinder-Polisher with a Automet 2 Power Head (Buehler, Ltd., Lake Bluff, IL) using 800 or 1200 grit sandpaper. The specimens were secured in a specimen holder and checked to be level by placing them on a tabletop. The polisher was run at a speed of 50 rpm, with the specimens spinning in a clockwise direction, while the polishing wheel to which the sandpaper was attached spun counterclockwise, and a downward force of 0 or 1 lbs, as set on the power head, was applied. Water was either pumped or poured onto the polishing surface to lubricate the process and prevent any dust produced from becoming airborne. This first step in polishing was done until the entire specimen surface was cleaned of epoxy and all the scratches on the specimen surface were parallel.

After initial polishing with sandpaper, the specimens were then polished on a LECO polisher (Vari/Pol VP-50, LECO Corp., St. Joseph, MI) using a sequence of diamond pastes with decreasing mean grit sizes. The sequence of diamond pastes began with paste having a mean grit size of 10 microns (Warren Diamond Powder Company, Inc., Saint-Bobain Industrial Ceramics, Inc., Olyphant, PA), proceeded to paste having a mean grit size of 6 microns (Warren Diamond Powder Company, Inc., Saint-Bobain Industrial Ceramics, Inc., Olyphant, PA), and concluded with paste having a mean grit size of 1 micron (Warren Diamond Powder Company, Inc., Saint-Bobain Industrial Ceramics, Inc., Olyphant, PA). Each diamond paste was used with one specific

aluminum polishing wheel, 30.5 cm in diameter, to which a polishing lap was adhered. With the 10 and 6 micron pastes, white polishing laps (White Technotron, 812-854, LECO Corp., St. Joseph, MI) were used, while red polishing laps (Red Technotron, 812-445, LECO Corp., St. Joseph, MI) were used with the 1 micron paste. To lubricate the polishing surface, prevent airborne dust, and prolong the effectiveness of the diamond paste, diamond extender was used (Microid Diamond Compound Diamond Extender, 811-004, LECO Corp., St. Joseph, MI).

The specimens were secured in a specimen holder that included a base to insure that the surfaces being polished were parallel to the plane of the specimen holder. Diamond paste, in dots approximately 2 mm in diameter spaced 2 cm apart, was put onto the surface of the polishing wheel. After the application of the diamond paste, the polishing wheel was wetted with diamond extender. Polishing was continued with each grit until all the scratches on the surface were parallel and generally the same size. (The size and orientation between the scratches was gauged by observation through an optical microscope.) After each step in the polishing process, the specimens were rinsed thoroughly with water and gently dabbed dry with Kimwipes (Kimberly-Clark Global Sales, Inc., Roswell, GA). Once the use of a polishing wheel was complete, it was wiped clean with damp paper towel and then dried with paper towel. The specimens were polished until a mirror-like surface was achieved.

To complete the polishing process, the specimens were cleaned in an ultrasonic bath (Ultramet III Sonic Bath, Buehler Ltd., Evanston, IL) for ten minutes The mounted and polished specimens were placed in a glass beaker that was filled with deionized water

so that the water level in the beaker matched that in the bath. During cleaning, the specimens were kept from contacting one another.

4.3. Milling

4.3.1. Dry Milling Scale-up

4.3.1.1. 50 g batch

Increasing the dry milling powder batch size to 50 g was investigated in two experiments. The feedstock powders for both experiments, and all milling experiments henceforth until otherwise noted, were crushed, ground, and reground using an alumina mortar and pestle.

One experiment was completed in two parts. First, 49.4 g of CGSR powder from ingot ETN158 (composition $Ag_{0.86}Pb_{19}SbTe_{20}$) was milled for 3 hr at 200 rpm in an Al_2O_3 milling jar with 280 g of D = 3 mm Al_2O_3 media in air. (CGSR means that the powder was crushed and ground using a mortar and pestle, sieved, and any material that did not pass through a 53 micron sieve was reground until it did pass through a 53 micron sieve.) Second, the powder was again milled for 3 hr at 100 rpm in an Al_2O_3 milling jar with 280 g of D = 3 mm Al_2O_3 media in air. The other 50 g batch size experiment also required two steps. First, 50.1 g of CGSR powder from ingot ETN166 (composition $Ag_{0.86}Pb_{19}SbTe_{20}$) was milled for 3 hr at 100 rpm in an Al_2O_3 milling jar with fourteen, D = 20 mm Al_2O_3 media in air. Second, the powder was further milled for 3 hr at 150 rpm in an Al_2O_3 milling jar with 280 g of D = 3 mm Al_2O_3 media in air.

4.3.1.2. 70 g batch

Increasing the dry milling powder batch size to 70 g was investigated in one experiment. CGSR powder from ingot ETN170 (composition $Ag_{0.86}Pb_{19}SbTe_{20}$) was milled for 3 hr at 150 rpm in an Al_2O_3 milling jar with 280 g of D = 3 mm Al_2O_3 media in air.

4.3.2. Reducing unexpectedly large powder particles

4.3.2.1. Remilling according to previously developed dry milling procedure

The first attempt to reduce the size of the largest powder particles was to return to the dry milling procedures described by Pilchak et al [42]. This original dry milling procedure required that the powder be milled in a batch of approximately 20 g for three hours at 100 rpm with ten 20 mm diameter Al_2O_3 spheres. Eighteen and four tenths g of powder from N172 batch 2 were milled according to the above procedure in Ar. This batch of powder was labeled "N172 batch 2.1."

The original dry milling procedure was then applied to seven other powder batches, which were labeled: N172 batch 2.2, N172 batch 3.1, N172 batch 3.2, N172 batch 1.1, N172 batch 1.2, and N172 batch 1.3. Table 4-2 lists the details of the re-milling of the powders from N172.

4.3.2.2. No longer using the 53 micron sieve

The powders from N172 that were remilled (see 4.3.2.1) were observed in the SEM. Micrographs from these powders showed that there were still large particles in the powder. Some of these large particles had dimensions that should not have been able to

pass through a 53-micron sieve. As a result, it was concluded that there was some kind of damage to the 53-micron sieve that allowed the passage of powder particles greater than 53 microns in diameter, so the usage of the 53-micron sieve was stopped. Instead, the 150 micron sieve and 75 micron sieve were used to sieve powders during the pre-milling process.

Again, the previously developed dry milling procedure as detailed in [42] was used. This new milling process was applied to four powder batches: P41 batch 1, P41 batch 2, P41 batch 3, and P41 batch 4. Ingot ETP41 had a composition of $Ag_{0.9}Pb_9Sb_{0.6}Sn_9Te_{20}$. The masses of batch 1, batch 2, batch 3, and batch 4 were 24.6, 25.0, 20.0, and 20.2 g respectively. All four powder batches were milled for 3 hr at 100 rpm with ten 20 mm diameter Al_2O_3 media in Ar.

4.3.2.3. Cleaning with alumina using D = 3 mm media

The next thought was that the milling jar and media were covered in a layer of LAST and/or LASTT. If that were the case, the residual powder accumulated on the grinding surfaces could hinder the milling process. To remove this residual powder a new cleaning process was attempted.

This new cleaning process was done in air involved the use of alumina powder (High Purity Alumina AKP-20, Sumitomo Chemical Company, Ltd., Tokyo, Japan) with a mean particle size of 0.5 microns. Specifically, the milling jar was loaded with 20.1 g of Al_2O_3 powder and 280 g of Al_2O_3 media. This mix was run in the mill for 10 minutes at a speed of 130 rpm.

After the cleaning run was complete, the media were removed from the jar. The jar was then wiped clean with 8 Kimwipes wetted with acetone (Mallicnckrodt Baker, Phillipsburg, NJ). The media were placed in the vibratory shaker (Retsch AS 200, Haan, Germany) for a total time of 15 minutes (three 5 minute long cycles) at a frequency of approximately 70 Hz.

The Al_2O_3 contaminated with LAST was collected in a small glass vial for proper disposal by ORCBS.

4.3.2.4. Cleaning with alumina using D = 20 mm media

After the cleaning process detailed in Section 4.3.2.3, the milling jar still appeared dirty. Another cleaning run was attempted. In air, the milling jar was loaded with 20.0 g of AKP-20 Al_2O_3 powder and ten D = 20 mm Al_2O_3 spherical grinding media. The milling jar and its contents were placed in the planetary mill, which ran for 10 minutes at 130 rpm.

Once the mill stopped, the milling jar was removed. One at a time, the media were rubbed clean of the Al_2O_3 powder with kimwipes and set aside. After all of the media were cleaned of the contaminated Al_2O_3 powder, all of the contaminated Al_2O_3 powder in the jar was collected. The milling jar's inner surface was then wiped clean with kimwipes wetted with acetone. The contaminated Al_2O_3 powder was placed in a small glass vial for proper disposal by ORCBS.

4.3.2.5. Cleaning with alumina using D = 20 mm media for a longer time

After two different cleanings with alumina, the inside of the mill jar still had the

Table 4-2—Details of the remilling of powder batches N172 batch 1.1 through N175 batch 4.1. All powders were of composition $Ag_{0.86}Pb_{19}Sb_{1.0}Te_{20}$. Also, all remilling was done for 3 hr at a speed of 100 rpm with ten 20 mm diameter spherical alumina media in Ar. For details on the milling procedure for the powders originally milled as 50 g batches, refer to Section 4.3.1.1. For details on the milling procedure for the powders originally milled as 75 batches, refer to Section 4.3.1.2.

Specimen	Previously Milled as	Remilling Mass (g)
N172 batch 1.1	75 g batch	25.1
N172 batch 1.2	75 g batch	25.0
N172 batch 1.3	75 g batch	24.9
N172 batch 2.1	75 g batch	18.4
N172 batch 2.2	75 g batch	18.8
N172 batch 3.1	50 g batch	25.0
N172batch 3.2	50 g batch	24.7

grey color of LAST/LASTT. As such, another cleaning run with alumina was attempted.

In air, the milling jar was loaded with 20.1 g of AKP-20 alumina powder and 10 alumina grinding spheres 20 mm in diameter. The mill was run for 1 hour at 130 rpm.

After the run finished, the milling jar was removed from the mill. As detailed above, in 4.3.2.3, the media were cleaned, the contaminated Al_2O_3 powder was collected for ORCBS, and the inside of the milling jar was cleaned.

4.3.2.6. Check with $Ag_{0.43}Pb_{18}Sb_{1.2}Te_{20}$ LAST

The problems with the powder particle size were first observed in powders from ingots with the composition $Ag_{0.86}Pb_{19}SbTe_{20}$. The previously developed dry milling procedure described by Pilchak et al [42] involved ingots having a composition of $Ag_{0.43}Pb_{18}Sb_{1.2}Te_{20}$, so the next thought was that the problem may have something to do with the change in composition of the powders being milled from $Ag_{0.43}Pb_{18}Sb_{1.2}Te_{20}$ to $Ag_{0.86}Pb_{19}Sb_{1.0}Te_{20}$.

Material from ingot N126, composition $Ag_{0.43}Pb_{18}Sb_{1.2}Te_{20}$, was crushed, ground, sieved, and reground in Ar inside the glove box. During the CGSR pre-milling treatment the powder passed through 150 micron, 75 micron, and 53 micron sieves. The powder from ingot N126 was milled according to the standard dry milling procedure: Approximately 20.0 g of powder with 10 spherical alumina media 20 mm in diameter in an alumina jar for three hours at a speed of 100 rpm. The milling was done in Ar.

4.3.2.7. N182 Experiments

After milling LAST with composition $Ag_{0.43}Pb_{18}Sb_{1.2}Te_{20}$ also showed large

particles within the powder, the next thought was to try mixing alumina media that was 20 mm in diameter and 3 mm in diameter. Because no milling had been done with material from a 400 g ingot, it was decided that all initial mixed media experiments would be done on material from ingot N182.

Three points about the crushing, grinding, sieveing, and regrinding of material from N182 should be emphasized. First, all powders from N182 were sieved through 150 micron, 75 micron, and 53 micron sieves. Second, all grinding and regrinding were done in porcelain mortars, 16.5 or 8.9 cm in diameter, and pestles, 22 or 15.3 cm long. Third, all pre-milling was done in an argon atmosphere.

4.3.2.7.1. Batch 3 (97.2 g D = 20 mm media + 97.6 g D = 3 mm media, 100 rpm)

The first batch of material milled at MSU was the third nominally 20 g batch of powder taken from N182. With five 20 mm diameter spherical alumina grinding media, having a mass of 97.2 g, and 97.6 g of 3 mm diameter spherical alumina grinding media, 20.1 g of powder from N182 was milled. Batch 3 was milled for 3 hrs at a speed of 100 rpm in the alumina milling jar designated for solely n-type material. The milling atmosphere was argon.

4.3.2.7.2. Batch 4 (97.2 g D = 20 mm media + 97.6 g D = 3 mm media, 150 rpm)

SEM micrographs of N182 batch 3 showed some decrease in both the in the number and size of large particles in the powder, but some particles with at least dimension that was 50 microns or greater were still present in the powder.

The next batch of powder from N182 milled was 20.0 g in mass. The powder was milled with five 20 mm diameter spherical alumina grinding media, having a mass of 97.2 g, and 97.6 g of 3 mm diameter spherical alumina grinding media in the n-type alumina milling jar. The mill ran for 3 hrs at 150 rpm . The milling atmosphere was argon.

4.3.2.7.3. Batch 5 (97.2 g D = 20 mm media + 97.6 g D = 3 mm media, 100 rpm, 24 hr, 25 cc hexane)

Again, SEM micrographs of the powder from N182 batch 4 showed a further decrease in both the in the number and size of large particles in the powder but large particles were still observed.

With five 20 mm diameter spherical alumina grinding media, having a mass of 97.2 g, 97.6 g of 3 mm diameter spherical alumina grinding media, and 25 cc of hexane, 20.0 g of powder from N182 was milled. Batch 5 was milled for 24 hrs at a speed of 150 rpm in the alumina milling jar designated for solely n-type material. The milling atmosphere was argon.

4.3.2.7.4. Batch 6 (139.9 g D = 20 mm media + 59.9 g D = 3 mm media, 100 rpm)

SEM micrographs of N182 batch 5 showed a further decrease in both the in the number and size of large particles in the powder. Additionally, the large powder particles had a more rounded shape, as is to be expected with the longer milling times. However, there were still large particles and agglomerates more than 30 microns across observed in the powder.

The next milling run used a different ratio of media than batches 3, 4, and 5. With seven 20 mm diameter spherical alumina grinding media, having a mass of 139.9 g, and 59.9 g of 3 mm diameter spherical alumina grinding media, 20.0 g of powder from N182 was milled. Batch 6 was milled for 3 hrs at a speed of 100 rpm in the alumina milling jar designated for solely n-type material. The milling atmosphere was argon.

4.3.2.7.5. Batch 7 (62.2 g D = 20 mm media + 141.6 g D = 3 mm media, 100 rpm)

SEM micrographs of N182 batch 6 showed improvement in number and size of large particles present in the powder. Eight powder particles with diameters of approximately 50 microns were observed in one SEM micrograph (Figure 5-20) of powder from N182 batch 6. Eleven powder particles with one dimension of 50 microns or greater were observed in an SEM micrograph of CGSR powder from N182 (Figure 5-12). (For a more thorough discussion of the results for powder batch 6 from ingot N182, please refer to Section 5.1.2.5.4.)

The next milling run used a third different ratio of media. With three 20 mm diameter spherical alumina grinding media, having a mass of 62.2 g, and 141.6 g of 3 mm diameter spherical alumina grinding media, 20.4 g of powder from N182 was milled. Batch 7 was milled for 3 hrs at a speed of 100 rpm in the alumina milling jar designated for solely n-type material. The milling atmosphere was argon.

4.3.2.7.6. Batch 8 (standard wet milling procedures, 25 cc hexane)

It was suggested that the next milling run be according to the standard wet milling procedure developed previously [43] because N182 batch 5 had been wet milled and

demonstrated a reduction in powder particle size.

The next milling run was a two step process. First, 20.0 g of material were dry milled for 3 hrs at 100 rpm with ten 20 mm diameter alumina spherical grinding media in alumina jar designated for solely n-type material. The milling atmosphere for this first step was argon. After the first step, 19.8 g of material were recovered in the glove box. These 19.8 g of powder were then milled for 24 hrs at 150 rpm with 25 cc of hexane. The wet milling was done in the n-type milling jar with 150 cc (364.4 g) of 3 mm diameter alumina spherical grinding media. The milling atmosphere for this second step was also argon.

4.3.2.7.7. Batch 9 (137.7 g D = 20 mm media + 58.8 g D = 3 mm media, 100 rpm, 6 hours)

The decrease in the number of and size of large particles in the powder with mixed media lead to the next thought which was to see what would happen when the milling time was increased.

Milling conditions like those for N182 batch 6 (4.3.2.7.4.) were chosen to have shown the most improvement, so the next milling run had similar conditions. With seven 20 mm diameter spherical alumina grinding media, having a mass of 137.7 g, and 58.8 g of 3 mm diameter spherical alumina grinding media, 20.0 g of powder from N182 was milled. Batch 9 was milled for 6 hrs at a speed of 100 rpm in the alumina milling jar solely for n-type material. The milling atmosphere was argon.

4.3.2.7.8.1. Batch 10, Dry Milled (137.8 g D = 20 mm media + 60.0 g D = 3 mm media, 100 rpm, two 3 hr cycles)

SEM micrographs from N182 batch 9 seemed to show very good improvement. Some agglomerates were visible, as well as some large powder particles. However, the number of large particles was significantly reduced.

When N182 batch 9 was collected, it was noted that all of the powder was either caked onto the sides and bottom of the milling jar or the 3 mm diameter alumina spherical grinding media. The next thought was to try milling with the same conditions as N182 batch 9 (4.3.2.7.7.), but to break the run into two three hour-long parts.

The next milling run was done in two parts. In the first part, 20.3 g of powder were milled with seven 20 mm diameter spherical alumina grinding media, having a mass of 137.8 g, and 60.0 g of 3 mm diameter spherical alumina grinding media in the alumina milling jar solely for n-type material. This first stage was for 3 hrs at 100 rpm. The milling atmosphere was argon.

After the first stage, the media was removed from the milling jar, and the milling jar's sides and bottom were scraped with a stainless steel laboratory spoon while inside the Ar atmosphere of the glove box. (The laboratory spoon has a total length of 22.9 cm, a shaft diameter of approximately 0.3 cm, and has a spoon at one end and a spatula at the other. The spoon on one end is 1.4 cm wide and 3.2 cm long, while the spatula end is 0.8 cm wide and 5.1 cm long.) Once the scraping was done, the media were returned to the milling jar. Then the second part of the milling run was completed. Like its predecessor, the second part was for 3 hrs at 100 rpm in an argon atmosphere.

4.3.2.7.8.2. Batch 10, Wet Milled (137.8 g D = 20 mm media + 60.0 g D = 3 mm media, 100 rpm, 6 hr, 25 cc hexane)

Powder from N182 batch 10 (Section 4.3.2.7.8.1.) that was dry milled for a total of 6 hrs was observed in the SEM. From the SEM micrographs, powder particles with one dimension equal to or greater than 50 microns were observed (e.g. six powder particles with one dimension equal to or greater than 50 microns are present in Figure 5-28). Also observed, were irregularly shaped agglomerates with sizes up to 60 microns long on the minor axis and 100 microns long on the major axis. (Refer to Section 5.1.2.5.8 for more details about the powder from N182 batch 10 after dry milling.) As such, the next thought was to try wet milling the powder.

The remaining powder was wet milled for 6 hrs at 100 rpm with 25 cc of hexane. The same media used to dry mill the powder were used to wet mill it, so the number and masses of the 20 mm diameter and 3 mm diameter spherical alumina grinding media were the same as above (Section 4.3.2.7.8.1.). However, only 17.5 g of powder were wet milled.

4.3.2.7.9. Batch 11 (Scale-up to 50 g Powder Charge)

After the success decreasing powder particle size with the combined dry and wet milling procedure derived from N182 batch 10 (Sections 4.3.2.7.8.1. and 4.3.2.7.8.2.), the next milling experiment with material from N182 was an attempt to increase the initial powder charge. Such a milling scale-up was important because the milling procedure derived from N182 batch 10 required 9 hours total of milling.

For N182 batch 11, 50.4 g of powder were dry milled with ten 20 mm diameter spherical alumina grinding media, having a mass of 198.7 g, and 90.0 g of 3 mm diameter spherical alumina grinding media in the alumina milling jar solely for n-type material. Initially, the powder was milled for 3 hrs at 100 rpm in argon. After the first three hours of milling, the milling jar was moved into an argon-filled glove box where 1.1 g of powder were removed for SEM observation and all the powder was scraped loose. The remaining 49.3 g of powder were then dry milled for a further 3 hrs at 100 rpm with the same media in the alumina milling jar solely for n-type material. The milling atmosphere for the second 3 hrs was also argon.

4.3.2.7.10. Batch 12 (Scale-up to 35 g Powder Charge)

SEM micrographs of the powders from N182 batch 11 dry milled for 6 hrs (4.3.2.7.9.) showed that the milling procedure was ineffective. In one SEM micrograph, seventeen powder particles with at least one dimension of approximately 50 microns or greater were observed (Figure 5-34 of Section 5.1.3.1). As such, a lesser increase in the powder charge was attempted next.

For N182 batch 12, the powder charge was 35.0 g. The powder was dry milled for 3 hrs at 100 rpm with ten 20 mm diameter spherical alumina grinding media, having a mass of 198.7 g, and 90.2 g of 3 mm diameter spherical alumina grinding media in the alumina milling jar solely for n-type material. The milling atmosphere was argon.

4.4. Milling Jar and Milling Media Cleaning

Milling jars and milling media were cleaned periodically (as described in Sections

4.4.1. and 4.4.2.) to prevent the accumulation of material on the sides of the milling jars or the media themselves with use. Milling jars and 20 mm diameter spherical alumina media were cleaned after two batches of powder were completely milled. The 3 mm diameter spherical alumina media were set aside after every batch of powder was completely milled. The "dirty" 3 mm diameter spherical alumina media were cleaned once 200 g or more of them accumulated.

4.4.1. Milling Jar and 20 mm Diameter Spherical Alumina Media Cleaning

Cleaning a milling jar and 20 mm diameter spherical alumina media was done outside the glove box, in air. Either the alumina milling jar used solely for n-type material with the 20 mm diameter spherical alumina media used solely for n-type material, or the other like set of alumina milling jar and 20 mm media for p-type material, were cleaned. Ten 20 mm diameter spherical alumina media were placed in the milling jar, and then approximately 100 g of glass beads (710-425 microns in diameter, Ballotini Ground Glass, Potters Industries, Inc., Valley Forge, PA) were poured into the milling jar. Next, the lid was placed on the milling jar, and the milling jar and its contents were loaded into the mill. The mill was set to run for 8 minutes at 130 rpm.

Once the mill finished running, the milling jar and its contents were moved to a fume hood. In the fume hood, the lid was removed from the milling jar. Each 20 mm 20 mm diameter alumina grinding sphere was individually removed from the jar and cleaned using acetone and Kimwipes. A 20 mm diameter alumina grinding sphere was sprayed with acetone and then buffed with a Kimwipe, which was repeated until the Kimwipe came away clean. Typically, the third Kimwipe used came away clean. After all the 20

mm diameter spherical alumina grinding media were cleaned, the contaminated glass beads were poured into a container for proper disposal. Next, the interior of the alumina milling jar was sprayed with acetone and then buffed with a Kimwipe. This was repeated ten times. Next, the two rubber o-rings on the milling jar lid were removed, a Kimwipe was wetted with acetone, and the alumina portion of the lid was buffed. The alumina portion of the milling jar lid was buffed with an acetone-wetted Kimwipe ten times. Each of the two rubber o-rings was wiped clean with a dry Kimwipe twice. After the channels in which rubber o-rings which sit were rubbed clean with a dry Kimwipe, the rubber o-rings were returned to their proper channels in the milling jar lid. The cleaning for the alumina milling jar and the associated 20 mm diameter spherical alumina media were then complete.

It should be noted that after the above cleaning procedure was completed, the inside of the milling jar and the 20 mm diameter spherical alumina media still appeared gray.

4.4.2. 3 mm Diameter Spherical Alumina Media

To clean the 3 mm diameter spherical alumina media, the 3 mm diameter spherical alumina media were first removed from the glove box and transported to a fume hood. Inside the fume hood, an appropriate amount of aqua regia (1 part nitric acid plus three parts hydrochloric acid, by volume) was prepared. Typically, at least 100 mL of aqua regia was prepared. The "dirty" 3 mm diameter spherical alumina media were placed in a 600 mL Pyrex beaker and the aqua regia was poured into the same beaker. The 3 mm diameter spherical alumina media sat in the aqua regia bath until the media

appeared white. While in the aqua regia bath, the 3 mm diameter spherical alumina media were stirred occasionally using a glass stirring rod. Once clean, the 3 mm diameter spherical alumina media and aqua regia were poured into a 5000 mL beaker filled with water. The diluted aqua regia was then poured into a container for proper disposal. Next, the 3 mm diameter spherical alumina media was rinsed thoroughly with water and then allowed to dry in ambient conditions.

4.4.2.1. Identification of Unknown Powder Resulting from Aqua Regia Cleaning

During the cleaning of the 3 mm diameter spherical alumina media, powder precipitated and collected in the bottom of the aqua regia bath. After the cleaning with aqua regia was complete, this unknown powder was collected for identification.

To identify the unknown powder, it was first observed via energy dispersive spectroscopy (EDS). The EDS was conducted at an accelerating voltage of 20 keV with a 15 mm working distance. The EDS spectrometry was conducted over 2 minutes.

After the EDS, 0.503 g of the unknown powder was sent to Dr. Rui Huang in the Chemistry Department at Michigan State University for x-ray diffraction (XRD) scanning. The XRD scan was conducted across a 2-theta of 10 to 80° with a step size of 0.05° using Cu $K_{\alpha 1}$ radiation.

4.5. Testing

4.5.1. Vickers hardness

Before the Vickers hardness of specimens could be measured, the specimens first had to be mounted and polished. Both the mounting and the polishing were done

according to the processes detailed above in 4.2.1. and 4.2.2.

After the specimens were properly prepared, hardness testing began. First, the Vickers indenter (M-400-G1, LECO Corporation, St. Joseph, MI) was turned on and calibrated. Nominally, calibration involved only three steps. The filars were moved together so that their two inner edges came into contact. Then the measurement readout was reset and the filars were moved apart. Finally, the filars were brought back together so that their inner edges came into contact again. If the measurement readout read within ±0.1 microns of zero, calibration was complete. If the measurement readout was outside the ±0.1 micron range, steps two and three were repeated until the measurement readout fell within the allowed range.

With calibration of the indenter complete, indentation started. The specimen was placed on the indenter's specimen stage and moved so that it was in focus through the indenter's optic. Next, a position was found at least 500 microns away from one specimen edge and at least 500 microns away from a specimen edge perpendicular to the first. Then, the specimen stage was rotated down a quarter turn and the indenter tip was rotated into position above the specimen. After positioning the indenter, an indent was made by pressing the "Start" button. Once the indenter completed the indent, the lens was returned to its position above the specimen and the specimen stage was rotated up a quarter turn. By moving the inner edges of the filars to opposite corners of the indent, the indent body diagonals were measured.

Once one indent was complete, the specimen stage was moved at least 500 microns laterally so that the next indent was at least 500 microns from the previous indent. The process was then repeated for the next indent and subsequent indents until at

least 20 viable indents had been measured. If lateral movement alone could not accommodate all the necessary indents, a second line of indents, parallel to the first, at least 500 microns distant, was made.

All Vickers hardness measurements were made with a load of 4.9 N, load time of 10 s, and load speed of 70 microns/s.

4.5.2. Thermomechanical Analysis

Thermomechanical analysis was performed at the High Temperature Materials Laboratory, Oak Ridge, Tennessee. Specimens used in thermal expansion measurements had at least two faces that parallel and opposite each other. Prior to testing, the specimen's mass and dimensions were measured.

The instrument—a TA Instruments Q400 Thermomechanical Analyzer (TMA)—was made ready. First, the specimen chamber was opened. Next, the specimen stand and probe were cleaned with acetone wetted cotton-tipped applicators until the applicator did not appear dirty. Then, the desired test program was entered into the operating software for the TMA. Hot pressed specimens were measured over five cycles, heating from 25 °C to 350 °C at 3 °C/min and cooling from 350 °C to 25 °C at 3 °C/min, followed by an isothermal hold for 15 minutes. Ingot specimens were measured over five cycles, heating from 25 °C to 400 °C at 3 °C/min and cooling from 400 °C to 25 °C at 3 °C/min, followed by an isothermal hold for 15 minutes. After the testing program was set, the testing atmosphere was selected. For these experiments, the atmosphere was argon flowing at 50 mL/min. Then a specimen name was entered into the software and a check was made to ensure that the name was saved.

The specimen was then loaded into the instrument. The specimen was placed on the center of specimen holder and the thermocouple was moved to within two millimeters, but not touching, the specimen. Next, the probe was lowered onto the specimen using the controls on the instrument or through the operating software. Before starting the test, a "pre-load" of 0.1 N was applied to the specimen. If the probe was not near the center of the specimen, the probe was raised, the specimen was moved, and the probe was lowered back down. With the specimen and probe properly situated, the specimen's initial length was measured by the instrument and recorded by the software. Then the specimen chamber was closed. While the chamber closed, the front of the furnace unit was gently lifted using one's hand to prevent any jarring of the specimen as the furnace settled. Finally, the run was started. While the test ran, the load on the specimen was 0.25 N.

4.5.3. Room Temperature Thermal Diffusivity

As was the case with the Thermomechanical analysis, room temperature thermal diffusivity measurements on LAST specimens also were performed at the High Temperature Materials Laboratory, Oak Ridge, Tennessee. The thickness of rectangular parallelepiped specimens approximately 10 mm long, 5 mm wide, and 3 mm thick were accurately measured using a digital micrometer (Digitrix II, Fowler, Nagai, Japan). This measurement was entered into the diffusivity measurement software. Similarly entered into the software was the number of measurements per second (500), the total number of measurements (1500), and the number of shot pulses (3). Because the specimens' 10 mm x 5 mm faces were highly polished, they were sprayed with graphite lubricant (Aerodag

G, Acheson Colloids Company, Port Huron, Michigan) inside a fume hood. One side was sprayed with graphite, the graphite was allowed to dry, and then the opposite side was sprayed and allowed to dry.

With the graphite coating in place, one specimen was loaded into the specimen holder directly over a hole in its center. This hole was surrounded by black clay. The specimen was pressed into the black clay by placing a kimwipe over it, and gently applying pressure with one's thumb. To ensure that there exist no gaps between the specimen's edges and the clay, the interface between them was inspected while shining a white light (I-150, Cuda Products Corporation, Jacksonville, Florida) behind the specimen. Any gaps in the interface were eliminated by using tweezers to push the clay against the specimen's side. With the specimen secured to the specimen holder, the iris on the holder was closed so that the specimen's corners were covered.

After securing the specimen to the holder, the specimen was then loaded into the instrument. First, the holder was secured in place by tightening a setscrew located on the holder's side. Next, the specimen was rotated approximately 90^{o} so that it was directly in front of a hole in the instrument. A dark curtain was placed so that the hole and specimen were covered.

Room temperature thermal diffusivity measurements were then taken. The diffusivity measurement software was started and the specimen was allowed to cool until its temperature was approximately at equilibrium. (The approach to equilibrium was monitored by the change in voltage of a thermocouple associated with the specimen. Specifically, the change in voltage was said to be approximately at equilibrium when the change in voltage was less than 0.001 V.) As the specimen cooled and the output voltage

det

tha

and

lan

sur

in s

thr

the

4.5

MS

cor

on

wa

wa

on

sp

Pe

su

po

M

detected by the instrument decreased, the offset in the measured voltage was adjusted so that the measurement was between ±10 V. Once the output voltage was less than -5.0 V and the change in voltage was less than 0.001 V, an optical pulse from a xenon flash lamp was fired by the instrument at the specimen. The pulse heated the specimen at the surface, and raised the specimen's temperature by no more than 2 °C [89]. This increase in specimen temperature changes the voltage detected by the instrument. For the next three seconds, the change in voltage was measured. Based on the time-voltage profile, the thermal diffusivity was calculated. This process was repeated twice more.

4.5.4. Biaxial Flexure Testing

Biaxial flexure testing (BFT) was done on hot pressed billets MSUHP-14 and MSUHP-16. Both specimens were made with powders from ingot N172, whose composition was $Ag_{0.86}Pb_{19}SbTe_{20}$.

Prior to testing, both specimens needed to be prepared, i.e. polished, but only on one side. The specimens were polished by hand because they were delicate. Polishing was done by moving back and forth on a polishing wheel set on a table. Gentle pressure was evenly applied to the billet with either three finger tips (thumb, index, and middle) on top of the specimen or two fingers (index, and middle) lying across the top of the specimen. The polishing wheels used were wetted with Microid Diamond Extender. Periodically, the specimen was turned 90°. A specimen was polished with one grit no surface defects were visible and all the scratches were parallel in one direction. The polishing grits used were 90 micron (Warren Superabrasives, Saint-Gobain Ceramic Materials, Anaheim, CA), 67 micron (Warren Superabrasives, Saint-Gobain Ceramic

Materials, Anaheim, CA), 35 micron (Warren Superabrasives, Saint-Gobain Ceramic Materials, Anaheim, CA), 10 micron, 6 micron, and 1 micron. When finished, the polished surface was mirror-like.

After polishing, the specimens were massed on an electronic balance and the specimen diameter was measured three times using a micrometer. The three diameter measurements were then averaged and the mean was used as the specimen diameter for calculations.

With all the preliminary work completed, the tests were conducted. The BFT measurements were taken on an Instron machine (Instron 4206, Instron Corporation, Norwood, MA). The normal attachments on the Instron were replaced with special ball-on-ring attachments (see Figure 4-2). Next, the Bluehill software that controlled the Instron was turned on. Once the Bluehill software was running, a test program created by Fei Ren, Jennifer Ni, and Bradley Hall was selected. Available specimen information—e.g. specimen name, mass, dimensions—and test parameters, such as loading rate (0.5 mm/min.), were entered into the software. The specimen was then placed polished side down over the center of the ring test fixture, so that the polished surface was the tensile surface during loading. With the specimen in place, the Instron was jogged down until it nearly touched the specimen. After checking that the specimen was centered, the test was started.

As soon as the specimen broke the test was stopped. The Instron was then jogged up and the fragments from the fracture specimen were taped down in a Petri dish. After the test, the thickness of all the pieces from the specimen was measured and averaged. The load, in N, at which the specimen fractured (P), the specimen radius (R), the

specimen thickness (t), the Poisson's ratio (ν) of the material tested, the support radius (a), and the effective contact radius between the specimen and the loading ball (b) were then used to calculate the fracture stress. (The effective contact radius between the specimen and the loading ball, b, was assumed to be approximately t/3 [90].) The equation to calculate the biaxial flexure strength is [90]

$$\sigma_b = \frac{3P(1+\upsilon)}{4\pi t^2}\left[1+2\ln\left(\frac{a}{b}\right)+\left(\frac{1-\upsilon}{1+\nu}\right)\left(1-\frac{b^2}{2a^2}\right)\left(\frac{a^2}{R^2}\right)\right] \quad (4.1)$$

In all calculations, Poisson's ratio was 0.2675 and the support radius, a, was 7.9 mm. A Poisson's ratio of 0.2675 is within the range of values reported in [91].

4.5.5. Brunauer-Emmett-Teller (BET) Surface Area Analysis

BET surface area measurements, conducted by Micromeritics Analytical Services (Norcross, GA), began by degassing the powder specimen to remove contaminants on its surface. All specimens were degassed for 6 hrs at a temperature of 200 °C. Following degassing, the sample was cooled under vacuum to a constant temperature. For specimens tested on our behalf, this temperature was that of liquid nitrogen. Once the powder specimen was cooled, either krypton or nitrogen gas, the adsorptive, was incrementally added to the sample chamber. (Krypton is used as the adsorptive gas for specimens having specific surface areas less than 0.5 m^2/g, and nitrogen is the adsorptive gas for specimens having specific surface areas more than 0.5 m^2/g.) The pressure inside the specimen chamber was then allowed to equilibrate. Following equilibration, the pressure inside the sample chamber was measured. Through a series of such pressure

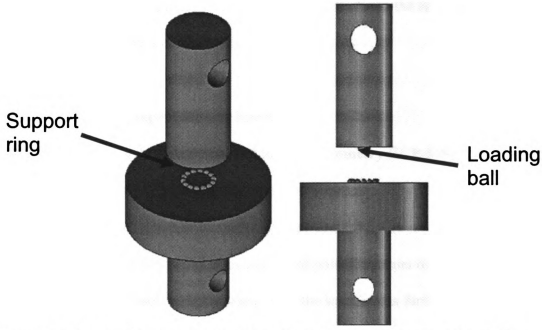

Figure 4-2—Schematic of the ball-on-ring fixture for biaxial flexure testing of hot pressed billets HPMSU-14 and HPMSU-16.

measurements, the adsorption isotherm was generated. From the adsorption isotherm, the specific surface area was determined.

4.5.6. Inductively Coupled Plasma Spectrometry

4.5.6.1. Inductively Coupled Plasma Mass Spectrometry (ICP-MS) at Shiva

Initial inductively coupled plasma mass spectrometries were conducted by Shiva Technologies, a subdivision of Evans Analytical Group LLC (Syracuse, NY). Sample preparation began by dissolving 50 to 100 mg of powder in aqua regia. After the powder sample completely dissolved in the aqua regia, the sample was further diluted using deionized water. (The exact dilution of each sample varies from sample to sample.) An internal standard was added to the sample, but specific standard was not stated. All internal standards used by Shiva Technologies are between Li and Tb and are provided by Inorganic Ventures (Lakewood, NJ). The mass spectrometer used was a Varian 820 (Palo Alto, CA).

4.5.6.2. Inductively Coupled Optical Emission Spectroscopy (ICP-OES) at Michigan State University

All specimen preparation was done at the Diagnostic Center for Population and Animal Health (Michigan State University, East Lansing, MI).

To begin, 1 g of powder was measured and leached overnight in a 95 °C oven with 5 mL of freshly prepared aqua regia. The next day, the sample was removed from the oven, allowed to cool to room temperature, and added to a 25 mL flask containing 1.25 mL of the internal standard yttrium. (The internal standard is used to correct for

viscosit

standar

be anal

Elevate

instrun

4.5.7.

Corpo

powd

the p

imag

4.5.7

spe

ana

the

co

Co

se

viscosity and matrix effects, or differences between the specimen and the calibration standard.) The mixture was then further diluted by a factor of 10, so that the solution to be analyzed had a dilution of 1:250. For comparison, NIST SRM 2711 Moderately Elevated Trace Element Concentration was prepared in a likewise fashion. The instrument used was a Varian Vista-Pro ICP-OES with a radial aligned torch.

4.5.7. Laser Scattering Particle Size Distribution Measurement

To size powders using a Saturn DigiSizer 5200 (Micromeritics Instrument Corporation, Norcross, GA), a suitable dispersion liquid is prepared. Then a sample of powder is dispersed in the dispersion liquid. Once properly dispersed, a test sample of the powder is placed in the machine and the analysis is done. Figure 4-3 is a labeled image of the Saturn DigiSizer indicating all the significant components.

4.5.7.1. Sample Analysis File Preparation

Prior to the actual sample analysis, a sample analysis file was created for the specimen. This file was made using the software associated with the Saturn. The sample analysis file contains all the information on the specimen to be tested, the dispersion, how the analysis is to be run, and what steps are to be completed automatically once testing is complete.

There are five sections to the sample analysis file: Sample Information, Analysis Conditions, Material Properties, Report Options, Collected Data. Only in the first three sections were changes from the default settings made.

In the sample information section of the sample analysis file, basic information was input. Specifically, what the sample was (LAST or LASTT), who the operator running the test was, and any pertinent comments (such as ingot number, batch number, and milling conditions) were entered.

Under the analysis conditions tab in the sample analysis file, the specifics on how the tests were to be run were entered. The flow rate was set to 8.0 L/min. Redispersion, to be done on the test sample by the internal ultrasonic probe after the test sample was introduced into the Saturn before the analysis had begun, was set at 100% power for 30 seconds. The minimum obscuration level was set to 5.0%, while the maximum obscuration level was set to 30.0%. Data collection, done at 5° intervals starting at 0°, was set to go to 45°. The total number of tests on the sample was set to 3. Lastly, the number of rinse cycles after the tests finished was set to 2.

Under the material properties section of the sample analysis file, details about the physical properties of the sample and dispersion liquid were input or selected. In the sample material section, the sample description (LAST powder), real portion of the refractive index (5.5), imaginary part of the refractive index (4.4) [92], and density (8.1 g/cm^3) input. (This input was entered only for the first time, and then saved. For subsequent tests, the sample description was selected from a list of saved data and the property values were input automatically.) In the analysis liquid section, the "40% Sucrose/Water" selection was made. The values of refractive index (1.4), viscosity (4.375 cp), and density (1.172 g/cm^3) were automatically input by the software. (The "40% Sucrose/Water" data for refractive index, viscosity and density was available in the

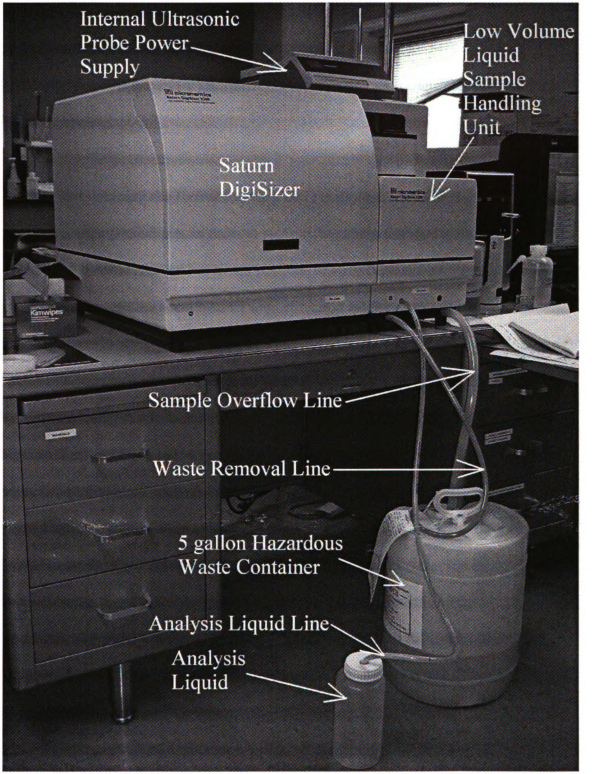

Figure 4-3—Image of the Saturn DigiSizer 5200 as it is setup for LAST or LASTT particle size analysis. All significant components labeled.

Saturn software package because a 40 wt% sucrose-water solution is a standard dispersion solution used by Micromeritics Analytical Services.)

With all the necessary information entered in the sample analysis file, the file was saved and closed.

4.5.7.2. Determining the Refractive Index of LAST and LASTT

As mentioned above, in order to measure a particle size distribution with a Saturn DigiSizer 5200, the real and imaginary portions of the refractive index are needed. The refractive index of LAST and LASTT are not readily available, so some effort was required.

The first step was to find papers that reported the complex refractive index for LAST or LASTT. Unfortunately, no papers that reported the complex refractive index for LAST or LASTT could be found. However, two papers [92-93] were found that do report n and k (the real and imaginary refractive index coefficients respectively) for PbS, PbSe, $Pb_xSn_{1-x}Te$ (x = 0.16, 0.35, 0.56, 0.78, and 1.00), as well as PbTe. Both papers [92-93] report the real and imaginary portions of the refractive index for energies between 1 and 5 eV. These energies are equivalent to wavelengths between 250 and 1240 nm. The data from these two papers [92-93] was judged to be acceptable since LAST is essentially doped lead telluride (where, for composition $Ag_{0.86}Pb_{19}Sb_{1.0}Te_{20}$, Ag and Sb constitute 4.6 mol% of the material).

Both papers [92-93] present the real and imaginary parts of the complex refractive index as functions of energy. As a result, the energy of the laser light used in the Saturn DigiSizer was calculated using Eq (4.1)

$$E = h\nu = hc/\lambda \quad (4.1)$$

where E is the energy, h is Planck's constant, υ is the frequency, c is the speed of light in a vacuum, and λ is the wavelength of the light (658 nm). From Eq (4.1), the energy was calculated to be 1.89 eV.

The data from [92] was calculated from measurements made by spectroscopic ellipsometry, while the data from [93] were simply calculations with no data measured. As such, only the data from [92] was considered. Even so, the data from both papers is comparable. Table 4-3 contains all the n and k data from [92-93] at an energy of 1.89 eV.

To begin, the two figures presenting the real part of the refractive index and the imaginary part of the refractive index were scanned and converted to .gif image files. The figure containing the data for the real part of the refractive index was then opened in Datathief, which is a computer program that accurately read figures so as to pull data from plots in published papers. Using Datathief, the exact value of the real part of the refractive index was read from the figure. This process was then repeated for the imaginary part of the refractive index, thus giving the complete complex refractive index for PbTe.

4.5.7.2.1. Comment on How the Complex Refractive Index is Applied

The Saturn uses the data on the complex refractive index to generate a model of light intensity versus angle based on Mie theory. To generate this model, the software begins by assuming a particle size. The software then uses the complex refractive index of the particle, the refractive index of the analysis liquid, and the wavelength of the light

used to calculate the scattering pattern for that particle. This process is then repeated for a spectrum of powder particles. The predicted scattering patterns for the spectrum of particle sizes are combined to generate a complete model of light intensity versus angle.

After the model is completely generated, light intensity versus angle for a powder specimen is measured. The software then determines what combination of particle models in what amounts will combine to best match the measured intensity versus angle data. With this information, a particle size distribution is generated.

If real portion, imaginary portion, or both portions of the complex refractive index are incorrect, the model and measured data will deviate from each other. As a result, the particle size distribution that is calculated will be erroneous. The only way to correct for errors in n or k are to replace the incorrect coefficient(s) with correct coefficient(s) and redo the particle size distribution measurement.

4.5.7.3. Dispersion Solution Preparation

A 28.6 wt% sucrose-deionized (DI) water solution was used as the dispersion liquid. To produce a 28.6 wt% sucrose solution, 1 L of DI water was measured into a one liter bottle. This 1 L of DI water was then degassed for at least 2 hours using an AquaPrep 055 (Micromeritics Instrument Corporation, Norcross, GA). (It should be noted that only pure water should be input to the AquaPrep 055 for degassing because anything else in the water, or any other liquid, would clog the filter through which the water passes to remove the gas in it.)

Degassing the DI water is a very important step in the particle sizing procedure. As discussed later, to successfully measure a particle size distribution, a background scan

must first be measured. If the water used to make the dispersing solution is not degassed, the background scan will be erroneous and so will the particle size distribution. The background scan will be erroneous if the dispersing solution is not degassed because air dissolved in the solution will form bubbles which will scatter light during the background scan and lower the intensity of laser light at a given angle. Furthermore, if the water to make the dispersing solution is not degassed, bubbles may form in the dispersing solution as the powder specimen is being analyzed. If that were to occur, the bubbles would also be sized with the powder specimen and the particle size distribution would be incorrect. (See Figure 4-4 for a schematic showing how bubbles during in a background scan alter the intensity versus angle plot.)

After the DI water was degassed, the mass of the degassed DI water was measured. The degassed DI water was then divided into two approximately equal halves (within ±5 g of equal) between the first one liter bottle and a second one liter bottle. To pour the degassed DI water between bottles, a funnel was used. (This funnel is used only with DI water and is labeled as such.)

Once the degassed DI water was divided between two 1 L bottles, the specific mass of the water in one bottle was determined. The mass of the degassed DI water in the bottle was multiplied by 0.4 to calculate the mass of sucrose to mix with that bottle of degassed DI water. The appropriate amount of sucrose was measured in two equal halves (within ± 0.1 g). The sucrose was subsequently added to the degassed DI water using a second funnel, exactly like the one used with for DI water. (This second funnel is used only with sucrose or water-sucrose solutions.)

Table 4-3—Real (n) and Imaginary (k) portions of the refractive indices of materials presented in [92-93]. The data from [92] was calculated from measurements made by Suzuki et al, while the data from [93] was simply calculations. All data for an energy of 1.89 eV.

Material	n	k	Reference
PbTe	5.5	4.4	[92]
$Pb_{0.84}Sn_{0.16}Te$	5.2	4.6	[92]
$Pb_{0.65}Sn_{0.35}Te$	4.8	4.8	[92]
$Pb_{0.44}Sn_{0.56}Te$	4.4	5.0	[92]
$Pb_{0.22}Sn_{0.78}Te$	4.1	5.4	[92]
SnTe	3.9	5.6	[92]
PbTe	4.6	5.3	[93]
PbSe	5.2	2.3	[93]
PbS	4.4	1.5	[93]

Two different kinds of sucrose were used to prepare the dispersion solution. One kind of sucrose was Domino Sugar: Pure Cane Granulated (Domino Foods, Inc., Yonkers, NY). The other sucrose was Sucrose, Crystal (Mallinckrodt Baker, Phillipsburg, NJ), which is an A.C.S. reagent. These specific kinds of sucrose were used because they come in plastic containers, not cloth or paper sacks. Sucrose packaged in cloth or paper sacks contains fibers that can clog the instrument or interfere with the particle size analysis (e.g. the fibers would be sized with the powders of interest).

After the entire amount of sucrose was added to the degassed DI water, the solution was mixed using a stainless steel laboratory spoon (like the one described above). The solution was stirred until no sucrose granules were visible on the bottom of the bottle and no improvement in the mixing was visibly obvious. When stirring, care was taken not to stir so vigorously as to introduce bubbles back into the water. The bottle was then sealed by screwing on its cap.

The entire sucrose determination, sucrose measurement, and sucrose addition process was repeated for second half of the degassed DI water in the other bottle. If two liters of solution were desired, the entire process detailed above was repeated for a second liter of DI water. A point was made to use the 28.6 wt% sucrose solution no more than 3 days after it was prepared because after such a time, air will likely have diffused back into the solution to a high enough concentration so that bubbles will form in the solution while it is in use. The problems encountered with the solution contains bubbles were mentioned above.

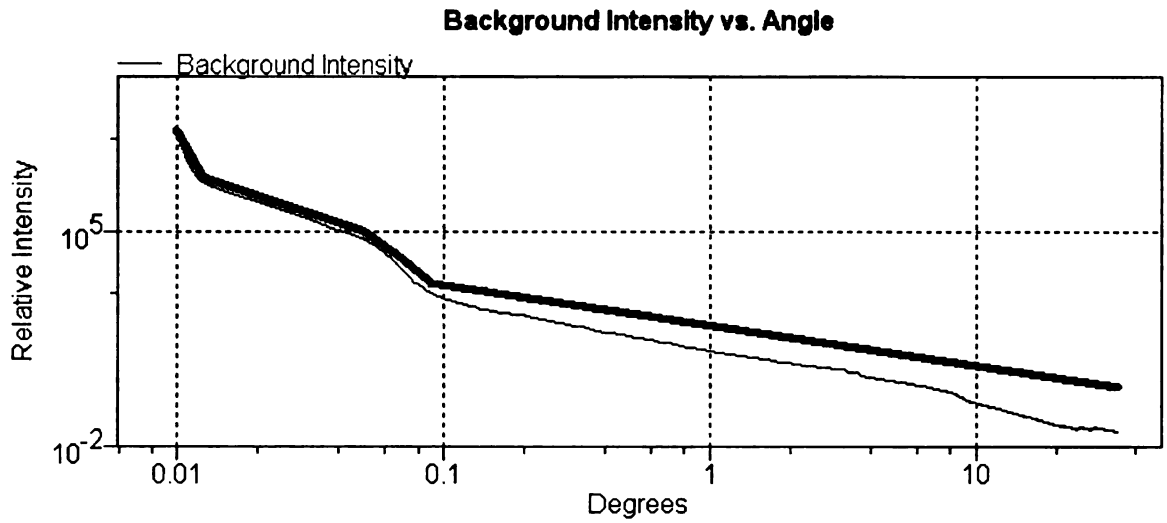

Figure 4-4—Schematic showing the effect of air bubbles resulting from improper solution degassing during a background scan. The thinner line shows a reasonable background scan. The heavier line shows the effect of air bubbles in the dispersion solution during a background scan: as the angle increases, the intensity becomes increasingly greater than the "good" background scan.

4.5.7.4. Sample Dispersion

After all of the necessary 28.6 wt% sucrose solution was prepared, the solution was combined in as few of the one liter bottles as possible. Approximately 40 mL of 28.6 wt% sucrose solution was then poured into a 100 mL Pyrex beaker and set aside.

A one liter bottle of solution was taken to the Saturn. The bottle's cap was removed, and the analysis liquid tube, connected to the Low Volume Liquid Sample Handling Unit, was placed in the bottle containing the 28.6 wt% sucrose solution. The tube was placed so that its end was less than 2.5 cm from the bottom of the bottle. With the analysis liquid tube properly located, the Saturn was rinsed once with the 28.6 wt% sucrose solution so that all the liquid inside the system was the dispersion solution. This rinse was accomplished by selecting "Unit1" from the menu bar, then selecting "Rinse" from the drop down menu, and then selecting "DigiSizer...". After selecting the proper command from the menu bar, a window opened where the number of rinses to be performed, between 1 and 9, was input (in this case, the number of rinses was 1), and Start button was chosen.

After the analysis liquid tube was moved to the one liter bottle containing the 28.6 wt% sucrose dispersion solution, the sample waste tube and sample overflow tubes were moved from their normal ten liter plastic jug to a 5 gallon hazardous waste jug.

Next, a background scan for the Saturn, without any sample in the system, was conducted. A background scan is a scan of the laser intensity as a function of angle when there is no sample in the Saturn. Without a background scan, the instrument cannot calculate how the light was scattered, thus preventing the calculation of the particle size distribution.

To complete the background scan, "Background..." was selected from the menu bar of the Saturn software. After selecting "Background...," a background measurement window was opened and the analysis liquid (in this case "40% Sucrose / Water") was selected. The "Next>>" button was then clicked, bringing up the next background measurement window. In the second background measurement window, the flow rate for the liquid, 8.0 L/min, was entered. The "Next>>" button was then clicked again, which began the actual scan.

The results of the background scan were checked to assess whether it was a "good" or "bad" background scan. A "good" background scan will show the lowest possible light intensities, which will decrease by approximately ten orders of magnitude; and sharp steps between beam angles will be present. A "bad" background scan will show higher light intensities at the higher angles and will be smoother (i.e. lacking sharp steps) [94].

After the background scan was completed, between 0.25 and 0.50 g of powder were added to the previously mentioned 40 mL of 40 wt% sucrose solution in the 100 mL Pyrex beaker. (This is a relatively wide range of mass. However, only a portion of the dispersed powder was put in the instrument and sized. For powders that were expected to be finer in size, the mass of powder that was dispersed was closer to 0.25 g. For powders that were anticipated to have larger particle sizes, the mass of powder that was dispersed was closer to 0.50 g.) Once the powder was added to the dispersion solution, it was stirred thoroughly using a laboratory spoon at a frequency less than 2 Hz for approximately 10 seconds. The beaker and its contents were then placed inside the ultrasonic bath (Ultramet III Sonic Bath, Buehler Ltd., Evanston, IL), containing

approximately 325 mL of deionized water, and ultrasonically dispersed for at least 7 minutes, but not longer than 10 minutes. As soon as the 7 minute ultrasonic dispersion was complete, the test sample was ready for analysis.

The powders were ultrasonicated to fully disperse, separate into individual and unattached particles, the powder sample. Ultrasonification is especially important to separate agglomerates, which are clusters of powder particles, into their constituent powder particles. Agglomerates come in two types: hard, which are dense and tightly packed, and soft, which are less dense and loosely packed. Soft agglomerates should readily be separated by ultrasonification, provided the source of ultrasonification is of sufficient power. Hard agglomerates may come apart during ultrasonification, but this may require very high energies and not all hard agglomerates are assured to separate.

4.5.7.5. Sample Analysis

With the sample dispersed by the Ultramet III Sonic Bath, the sample analysis began. First, "Sample Analysis..." was selected under the Unit1 dropdown menu in the Saturn software and the appropriate sample was chosen. After the analysis conditions were reviewed and approved, the Saturn was ready for the test sample to be placed in the sample handling unit.

To place the test sample in the Saturn, the ultrasonic bath was turned off and the 100 mL beaker containing the dispersed specimen was removed. The beaker and its contents were then carried to the Saturn. As the dispersed specimen was transported to the Saturn, it was continually stirred using a disposable plastic pipette 15.5 cm long (Samco Scientific, San Fernando, CA). Once at the Saturn, the test sample was placed in

the sample handling unit via the disposable pipette. Test sample from the beaker was added to the sample handling unit until the obscuration detected by the Saturn was approximately 15.0% (± 3%). (Obscuration refers to how much the light intensity measured by the Saturn has decreased relative to the background scan due to the light scattering caused by the powder sample in the instrument. The obscuration is read above an obscuration bar graph in the "Sample Analysis" window. As the majority of the powder particles sized are between 1 and 100 microns, a 15% obscuration is recommended by [94].) With the obscuration at acceptable levels, the actual measurement of the test sample started. The Saturn DigiSizer has the ability to automatically adjust the obscuration by adding analysis liquid to or draining analysis liquid containing powder sample from the sample chamber, but this feature was not used because it did not function properly.

4.5.7.6. After Sample Analysis (Station and Equipment Cleaning)

The test sample added to the Saturn was tested three times, which took approximately 15 minutes. (During these 15 minutes, the specimen was continuously cycled through the instrument while the laser light intensity was measured at each of the ten different angles three separate times.) As set in the sample analysis file, once all tests were completed, the Saturn automatically rinsed itself twice. These first two rinses were done with the 28.6 wt% sucrose-degassed DI water dispersion solution.

During a rinse, the ultrasonic probe in the Saturn first runs at maximum power for approximately 10 seconds. Then a valve at the bottom of the Low Volume Liquid Sample Handling Unit (LVLSHU) opened. Through this valve, the analysis liquid

flowed out the waste tube to the 5 gallon hazardous waste container. Once empty of liquid, the waste valve was closed and new liquid was pumped through the analysis liquid tube into the LVLSHU. This new analysis liquid/rinse solution filled the instrument from bottom to top.

Following the first two rinses with the 28.6 wt% sucrose dispersion solution, the analysis liquid tube was removed from the one liter bottle that contained the dispersion solution and rinsed with DI water from a squeeze bottle. DI water that collected on the floor was mopped up using paper towel. Once the analysis liquid tube was clean, it was placed in a ten liter jug containing degassed DI water. The Saturn was then rinsed at least nine more times, but with degassed DI water.

To rinse the Saturn with degassed DI water nine times, the analysis liquid tube was first removed from the 1 L bottle containing the analysis liquid and placed in another container. This other container held the degassed DI water. Then, in the Saturn software, under "Unit 1" on the menu bar, "Rinse" was highlighted and "DigiSizer..." was selected. This opened a DigiSizer rinse window, where the number of rinses to be performed was entered. The button labeled "Start" was then clicked, and the rinsing procedure, as detailed above, began, but with degassed DI water.

Next, any excess dispersed sample in the 100 mL beaker was poured into the 5 gallon hazardous waste jug. Typically, some residual powder-dispersion slurry was on the bottom of 100 mL beaker. This slurry was sprayed with approximately 20 mL of DI water from a squeeze bottle and the DI water-slurry mixture was also poured into the 5 gallon hazardous waste jug. The process of spraying the slurry and pouring it into the hazardous waste jug was repeated at least two more times. Any remaining slurry was

wiped out of the 100 mL beaker using kimwipes. Once all the powder was removed from the 100 mL beaker, the beaker was cleaned using Alconox detergent (Alconox, Inc., New York, NY) and DI water. After the cleaning, the beaker was dried using kimwipes and put away.

After cleaning the 100 mL beaker that contained the dispersed sample, both the sample waste tube and sample overflow tube were sprayed clean with DI water so that any dirt flowed into the 5 gallon hazardous waste jug. For extra measure, both tubes were then wiped clean with paper towel. Care was taken not to rip or damage the paper towel while the tubes were wiped clean to reduce the risk of introducing fibers into the Saturn. Once clean, both the sample waste tube and the sample overflow tube were returned to the ten liter waste jug.

4.6. Reevaluation of Laser Scattering Particle Size Distribution Measurements

After the particle size distribution measurements by light scattering using a Saturn DigiSizer 5200 were completed for the powders from N182 and others, an error was discovered. The degassed DI water plus 28.6 wt% sucrose dispersion solution, as detailed in Section 4.5.7.2., was not the intended 40 wt% sucrose solution. (The difference between the intended sucrose solution and the one that was used initially arose because forty percent of the solution's *total* mass was supposed to be sucrose. That is, if the solution was to have a mass of 100 g, 40 g would be sucrose and 60 g would be degassed DI water. Instead, sucrose equivalent to forty percent of the degassed DI water's mass was added. As such, if 100 g of DI water were degassed, 40 g of sucrose

were added. So, the ratio of sucrose mass to total solution mass would be 40 to 140, as opposed to 40 to 100 for the correct case.)

This mistake with respect to the dispersion solution did not affect the light intensity versus angle measurements. However, the mistake did affect the calculations made by the Saturn's software to calculate the particle size distribution. As noted in Section 2.3., the index of refraction for both a particle and that particle's *surrounding medium* are important to calculate light scattering according to Mie theory. The refractive index for the analysis liquid/dispersion solution used to calculate the particle size distributions in Figures 5-11, 5-13, 5-15, 5-17, 5-5-19, 5-21, 5-23, 5-25, 5-27, 5-30, and 5-33 was incorrect. Rather than being 1.400, the refractive index was approximately 1.379 [95].

Unfortunately, the problem could not be fixed by inputting the index of refraction for a 28.6 wt% sucrose solution in the Saturn's software and recalculating the particle size distribution. Instead, new particle size distributions had to be measured. The subsequent sections detail the procedures used to measure the particle size distributions using a 40 wt% sucrose solution.

4.6.1. Sample Analysis File Preparation

The sample analysis file was prepared as detailed in Section 4.5.7.1., but with a few changes. Redispersion by the Saturn's internal ultrasonic probe was deactivated. The total number of tests to be done on the sample was set to 8. Also, the circulation time for the sample—the time the test sample flows through the Saturn before the tests start—was set to 620 s.

Again, "40% Sucrose/Water" selection was made for the analysis liquid under the material properties tab in the sample analysis file. This time, though, the values for refractive index, viscosity, and density were correct for the analysis liquid supplied to the Saturn.

4.6.2. Dispersion Solution and Analysis Liquid Preparation

In a departure from the procedures detailed in Section 4.5.7.2., the dispersion solution and analysis liquid were different. The dispersion liquid was degassed DI water containing sodium pyrophosphate ($Na_4P_2O_7 \cdot 10H_2O$, Mallinckrodt Baker, Phillipsburg, NJ), a surfactant recommended by Micromeritics Analytical Services, at a concentration of 5 mg/L. The analysis liquid was 40 wt% sucrose in 60 wt% degassed DI water.

Preparation of the dispersion liquid began by degassing 1 L of DI water using the AquaPrep 055 for at least 2 hrs. After degassing, 5 mg of sodium pyrophosphate were measured using an electronic balance and then added to the liter of degassed DI water. The sodium pyrophosphate was then allowed to diffusively mix in the one liter of degassed DI water for approximately 2 hrs.

Preparation of analysis liquid followed the process detailed in Section 4.5.7.2. However, to determine the mass of sucrose to be added to the degassed DI water, a different multiplicative factor was used. Rather than multiply the mass of degassed DI water by 0.4, the mass of degassed DI water was multiplied by 2/3. The corresponding mass of Sucrose, Crystal from Mallinckrodt Baker was measured and then added to the degassed DI water.

4.6.3. Sample Dispersion

Sample dispersion for the most part followed the procedure detailed in Section 4.5.7.3., but with a few modifications.

As in the previously conducted measurements, the powder test sample was dispersed in a 100 mL Pyrex beaker. For the new measurements, though, the 100 mL Pyrex beaker was filled with approximately 50 mL of dispersion solution (degassed DI water plus 5 mg/L sodium pyrophosphate). Also, all test samples were nominally 0.50 g in mass. The ultrasonic bath contained approximately 375 mL of DI water and was used to ultrasonically disperse the test sample for approximately 10 minutes.

The analysis liquid (40 wt% sucrose solution) was introduced into the Saturn and a background scan was completed following the steps outlined in Section 4.5.7.3.

4.6.4. Sample Analysis

Sample analysis followed exactly the procedure detailed in Section 4.5.7.4.

4.6.5. After Sample Analysis

The steps taken after the sample analysis was completed followed the steps detailed in Section 4.5.7.5. However, the analysis took approximately 40 minutes because the sample was circulated for 620 s and eight tests were conducted on the test sample.

5. Results and Discussion

5.1. Milling

5.1.1. Dry Milling Scale-up

5.1.1.1. 50 g batch

Two methods were tried to increase the powder batch size for dry milling to 50 g. One methodology involved milling 50 g of powder for 3 hr at 200 rpm with 280 g of the 3 mm diameter Al_2O_3 media, which was applied to material from N158. The other methodology involved milling 50 g of powder for 3 hr at 100 rpm with fourteen 20 mm diameter Al_2O_3 spheres, then milling the 50 g of powder for a further 3 hr at 150 rpm with 280 g of 3 mm diameter Al_2O_3 media. This second methodology was applied to powder from ingot N166 was the more effective of the two methodologies.

Figures 5-1 and 5-4 are SEM micrographs showing a typical sample of the powder from N158 and N166 after all planetary milling. Figures 5-3 and 5-5 are particle size distributions, measured by Coulter Counter, of powder samples from N158 and N166 (respectively). The particle size distribution for N158, measured by Coulter Counter, had a mean of 5.15 microns and a median of 4.53 microns, while the particle size distribution for N166, measured by Coulter Counter, had a mean of 5.11 microns and a median of 4.45 microns.

The key difference between the powders from N158 and N166 is that N158 contained macroscopic agglomerates (Figure 5-2) that were approximately 5 mm long and 2 mm wide. The formation of the large agglomerates was likely caused by the high milling speed, 200 rpm, used with this powder, as opposed to the 150 rpm milling speed used with the powder from N166. The macroscopic agglomerates were collected using a

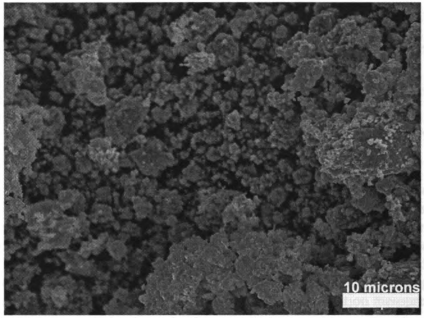

Figure 5-1—SEM micrograph of powder from N158 (composition $Ag_{0.86}Pb_{19}Sb_{1.0}Te_{20}$). The powder is the result of an experiment to increase the powder charge for dry milling to 50 g and was dry milled for 3 hr at 200 rpm with 280 g of 3 mm diameter alumina media in air, then further dry milled for 3 hr at 100 rpm with 280 g of 3 mm diameter alumina media in air. Notice that the powder particles in this SEM micrograph at 10 microns in diameter or smaller.

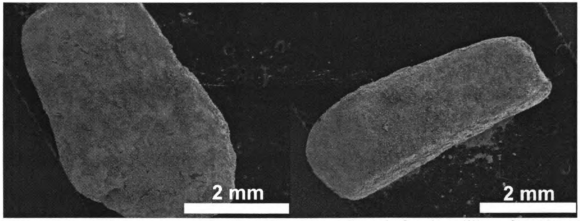

Figure 5-2—SEM "macrographs" of agglomerates collected after the milling of N158 (composition $Ag_{0.86}Pb_{19}Sb_{1.0}Te_{20}$). This powder was dry milled for 3 hr at 200 rpm with 280 g of 3 mm diameter alumina media in air, then further dry milled for 3 hr at 100 rpm with 280 g of 3 mm diameter alumina media in air. Notice that these agglomerates have dimensions on the order of *millimeters*.

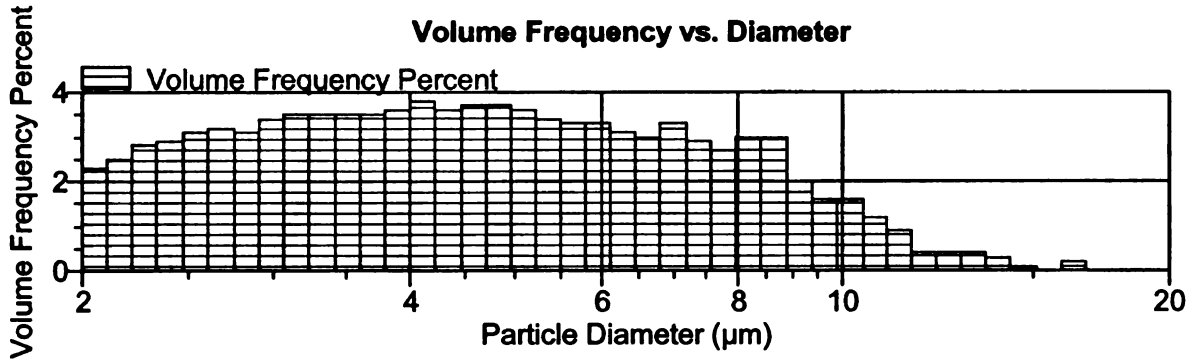

Figure 5-3—Particle size distribution, measured on a Coulter counter, of powder from N158 (composition $Ag_{0.86}Pb_{19}Sb_{1.0}Te_{20}$). This powder was dry milled for 3 hr at 200 rpm with 280 g of 3 mm diameter alumina media in air, then further dry milled for 3 hr at 100 rpm with 280 g of 3 mm diameter alumina media in air. The mean is 5.15 microns and median is 4.53 microns. The particle size distribution is not skewed, as would be expected because of the large agglomerates seen in Figure 5-2, because no agglomerates were included in the powder sample sent for particle size distribution measurement.

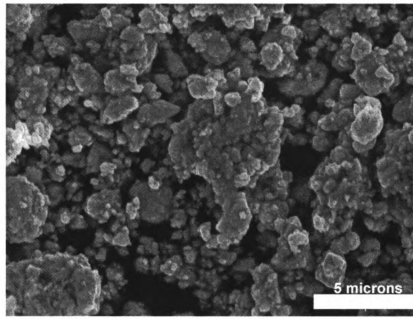

Figure 5-4—SEM micrograph of powder from N166 (composition $Ag_{0.86}Pb_{19}Sb_{1.0}Te_{20}$). The powder is the result of an experiment to increase the powder charge for dry milling to 50 g. The powder was dry milled for 3 hr at 100 rpm with fourteen 20 mm diameter alumina milling media in air, then dry milled for 3 hr at 150 rpm with 280 g of 3 mm diameter alumina milling media in air. In the micrograph, the largest powder particles appear to be approximately 5 microns in diameter.

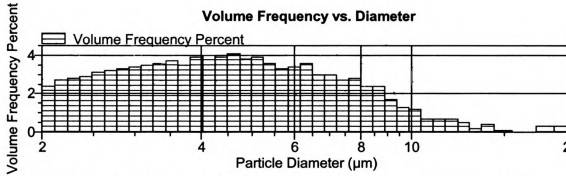

Figure 5-5—Particle size distribution, measured on a Coulter counter, of powder from N166 (composition $Ag_{0.86}Pb_{19}Sb_{1.0}Te_{20}$). The powder is the result of an experiment to increase the powder charge for dry milling to 50 g. The powder was dry milled for 3 hr at 100 rpm with fourteen 20 mm diameter alumina milling media in air, then dry milled for 3 hr at 150 rpm with 280 g of 3 mm diameter alumina milling media in air. The mean of the particle size distribution is 5.11 microns, while the median is 4.45 microns.

laboratory spoon and placed in a glass vial after the powder was milled for a second time for 3 hr at 100 rpm with 280 g of 3 mm diameter Al_2O_3 media, as detailed in 4.3.1.1., which was intended to break-up the large agglomerates. None of the macroscopic agglomerates were included in the powder specimen sent for particle size distribution measurement. As a result of excluding the agglomerates from the sample sent for Coulter Counter analysis, the particle size distribution for powder from N158, Figure 5-3, is not skewed because of the macroscopic agglomerates.

5.1.1.2. 70 g batch

After the apparent success in developing a 50 g powder charge dry milling procedure, a further scale-up in the dry milling powder batch size was attempted with material from ingot N170. Figures 5-6 and 5-7 are a typical SEM micrograph of powder from N170 and a particle size distribution for powder taken from N170 after planetary milling. The mean particle diameter and the median particle diameter determined from the Coulter Counter were 8.13 microns and 6.95 microns, respectively. Since neither SEM observation nor the Coulter Counter particle size distribution indicated the presence of any powder particles with diameters greater than 30 microns, it was concluded that the milling procedure detailed in 4.3.1.2. was a viable means to dry mill powder in 70 g batches.

5.1.2. Reducing unexpectedly large powder particles

5.1.2.1. Remilling according to standard dry milling procedure developed previously

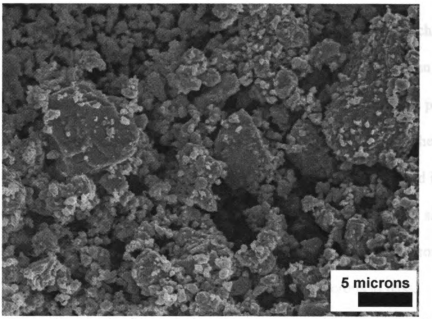

Figure 5-6—SEM micrograph of powder from N170 (composition $Ag_{0.86}Pb_{19}Sb_{1.0}Te_{20}$). The powder is the result of an experiment to increase the powder charge for dry milling to 70 g. The powder was dry milled for 3 hr at 150 rpm with 280 g of 3 mm diameter alumina milling media in air. Most of the powder particles are 5 microns in diameter or smaller, but there is one powder particle that has a major diameter of approximately 25 microns.

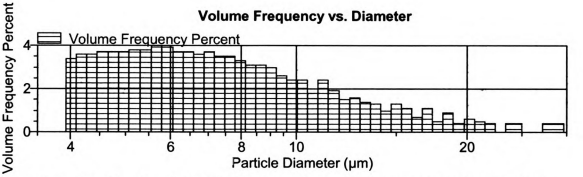

Figure 5-7—Particle size distribution, measured on a Coulter counter, of powder from N170 (composition $Ag_{0.86}Pb_{19}Sb_{1.0}Te_{20}$). The powder is the result of an experiment to increase the powder charge for dry milling to 70 g. The powder was dry milled for 3 hr at 150 rpm with 280 g of 3 mm diameter alumina milling media in air. The mean is 8.13 microns and the median is 6.95 microns. The largest powder particles sized were approximately 30 microns in diameter.

Figure 5-8 shows a typical sample of powder from N172 batch 2, which was initially milled according to the procedure detailed in Section 4.3.2.1., and then remilled according to the dry milling procedure developed previously [42]. Numerous powder particles with dimensions of approximately 50 microns, were still present in the powder despite the remilling the powders. Since the largest powder particles observed in the remilled powder from N172 should not have been able to pass the 53 microns sieve prior to milling, it was concluded that there was tear or other damage in the 53 micron sieve that allowed powder particles with dimensions exceeding 53 microns to pass.

5.1.2.2. No longer using the 53 micron sieve

Since it was believed that the 53 micron sieve was damaged, its use was stopped (Section 4.3.2.2.). It was hoped that no longer using the 53 micron would get rid of the powder particles that were approximately 50 microns in diameter.

Figure 5-9 is a SEM micrograph of powder from P41 batch 3. This powder was milled according to a previously developed dry milling procedure [42] except that only a 150 micron and a 75 micron sieve were used during the crushing, grinding, sieving, resieving prior to milling. Again, numerous powder particles with at least one dimension equal to or greater than 50 microns are observed. Some of these large powder particles are 80 microns by 120 microns in size or larger. Since the smallest sieve used with the powders was 75 microns, powder particle dimensions of up to approximately 75 microns are not necessarily unexpected. However, the fact that multiple powder particles with dimensions on the order of 80 microns or greater were

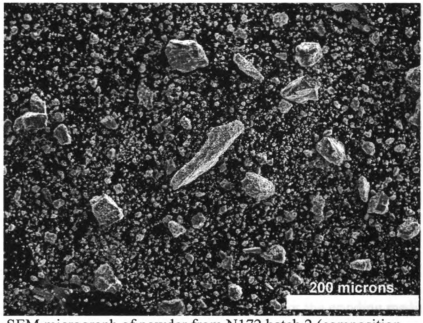

Figure 5-8—SEM micrograph of powder from N172 batch 2 (composition $Ag_{0.86}Pb_{19}Sb_{1.0}Te_{20}$) after remilling. The powder was remilled according to the previously developed milling procedure [42] (dry milled 3 hr at 100 rpm with ten 20 mm diameter alumina grinding media), but in Ar. In the SEM micrograph, there are approximately four powder particles with diameters approaching 50 microns or greater.

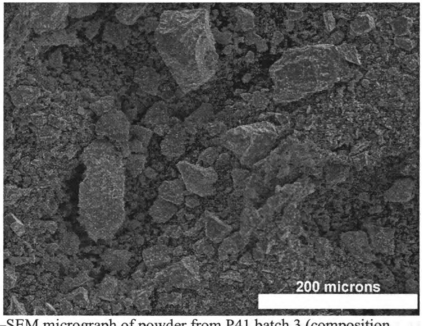

Figure 5-9—SEM micrograph of powder from P41 batch 3 (composition $Ag_{0.9}Pb_9Sb_{0.6}Sn_9Te_{20}$). The powder was dry milled according to the previously developed milling procedure [42] (dry milled 3 hr at 100 rpm with ten 20 mm diameter alumina grinding media in Ar). In the SEM micrograph there are approximately three powder particles with diameters of roughly 80 microns.

observed in the SEM micrograph suggested that this milling process was not completely effective.

5.1.2.3. Attempts to clean the mill jar and grinding media with AKP-20 alumina powders

The next three attempts to solve the problem of the large powder particles involved trying to clean the milling jar and media with alumina powder (as detailed in Sections 4.3.2.3., 4.3.2.4., and 4.3.2.5.). The thought was that LAST or LASTT had accumulated on the inner surfaces of the milling jar and/or the grinding media. If a sufficient layer of LAST or LASTT coated the mill jar and grinding media then the mill's effectiveness would have been decreased because LAST and LASTT have a much lower hardness than alumina.

Observations of the milling jar and media after all three experiments indicated that using alumina to clean the inner surfaces of the milling jar was ineffective. (Refer to Sections 4.3.2.3-4.3.2.5 for the details of these experiments). The inner surfaces of the milling jar remained dark and gray, as opposed to returning to the pale, dingy white color the alumina in the milling jar had when it was brand new.

Attempts to clean the media had results similar to the effort to clean the milling jar; that is the media used in the alumina cleaning experiments did not become clean. The 20 mm diameter spherical alumina media did not become white from the cleaning, but instead maintained the silver or gray color observed after use milling LAST. Likewise, despite three successive attempts to clean the 3 mm diameter spherical alumina

media with alumina powder, the 3 mm diameter media did not become white, or even cease to be gray.

5.1.2.4. A return to milling $Ag_{0.43}Pb_{18}Sb_{1.2}Te_{20}$ LAST

All of the difficulties with powders containing particles greater than 30 microns in diameter were observed in powders with a composition of $Ag_{0.86}Pb_{19}Sb_{1.0}Te_{20}$. However, the previously developed milling procedure was developed with material having a composition of $Ag_{0.43}Pb_{18}Sb_{1.2}Te_{20}$. The next experiment involved milling material from ingot N126, which had a composition of $Ag_{0.43}Pb_{18}Sb_{1.2}Te_{20}$. This powder, from N126, was also the first powder to use the new 53 micron sieve in the milling process.

Figure 5-10 and a SEM micrograph of powder from ingot N126 milled following the previously developed milling procedure [42]. Figure 5-11 is a particle size distribution, measured by light scattering using a Saturn DigiSizer, of powder from N126.

Both Figures 5-10 and 5-11 demonstrate the presence of powder particles ranging from 30 to almost 100 microns in diameter in the powder from N126. In Figure 5-10, twenty-two powder particles, in an area approximately 550 microns by 415 microns, with at least one dimension greater than 30 microns are observed, with the largest approaching 100 microns in diameter. Similarly, the particle size distribution, measured by light scattering using a Saturn DigiSizer, has a mean of 8.3 microns and a median of 4.6 microns. Comparatively, the mean for similarly milled powder reported in [42] is 6.4 microns.

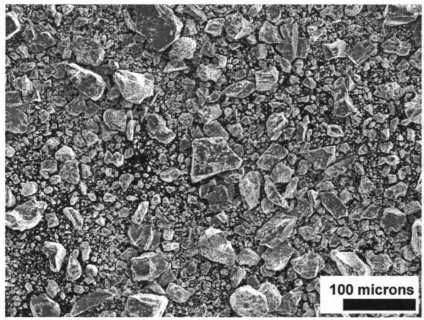

Figure 5-10—SEM micrograph of powder from N126 (composition $Ag_{0.43}Pb_{18}Sb_{1.2}Te_{20}$). During the premilling treatment of the powder, the smallest sieve used was 53 microns. The powder was dry milled 3 hr at 100 rpm with ten 20 mm diameter alumina grinding media in Ar. Twenty-two powder particles with dimensions ranging between 30 and 100 microns are present in the SEM micrograph.

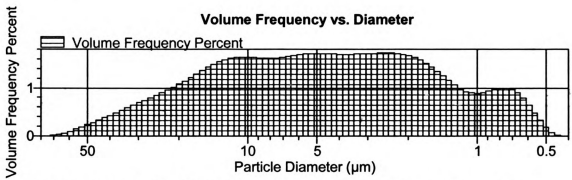

Figure 5-11—Particle size distribution, measured by light scattering using a Saturn DigiSizer, of powder from N126 (composition $Ag_{0.43}Pb_{18}Sb_{1.2}Te_{20}$). During the premilling treatment of the powder, the smallest sieve used was 53 microns. The analysis liquid used was a 28.6 wt% sucrose/degassed DI water solution. The powder was dry milled 3 hr at 100 rpm with ten 20 mm diameter alumina grinding media in Ar. The mean is 8.3 microns and the median is 4.6 microns. The mean reported in [42] for a powder of the same composition milled according to the same procedure is 6.4 microns.

5.1.2.5. N182 Experiments

Figure 5-12 is an SEM micrograph of CGSR powder from ingot N182, and Figure 5-13 is a particle size distribution, measured by light scattering using a Saturn DigiSizer, for CGSR powder from ingot N182. In Figure 5-12, many powder particles with dimensions of approximately 50 microns are observed. For Figure 5-13, the particle size distribution's mean is 17.8 microns, and the median is 12.1 microns, as determined with a Saturn DigiSizer by light scattering. The results of the particle size reduction experiments with material from N182 will be compared to Figures 5-12 and 5-13.

5.1.2.5.1. Batch 3 (97.2 g D = 20 mm media + 97.6 g D = 3 mm media, 100 rpm)

Figure 5-14 is an SEM micrograph of powder from N182 batch 3 and Figure 5-15 is a particle size distribution, measured by light scattering using a Saturn DigiSizer, for powder from N182 batch 3. The particle size distribution in Figure 5-15 has a mean of 10.0 microns and a median of 3.2 microns, as determined with a Saturn DigiSizer by light scattering.

Comparing Figures 5-14 and 5-15 to Figures 5-12 and 5-13, changes in the powder are apparent. In Figure 5-14, there are roughly eighteen powder particles that have one dimension that is approximately 50 microns or greater. For a similar area, roughly 1100 microns by 800 microns, in Figure 5-12, there are approximately thirty-four powder particles with at least one dimension that is 50 microns or greater. Likewise, the particle size distributions, both measured using a Saturn DigiSizer, for the powder from N182 batch 3 and the CGSR powder from N182 respectively contained 4.4 and 7.9 volume percent particles that were 50 microns in diameter or greater.

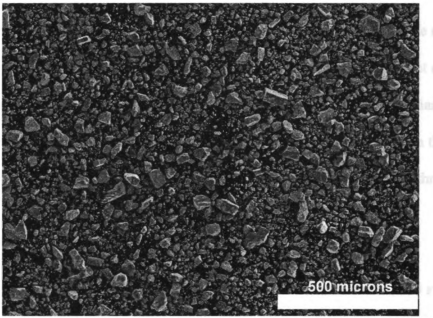

Figure 5-12—SEM micrograph of powder from N182 (composition $Ag_{0.86}Pb_{19}Sb_{1.0}Te_{20}$) that has been crushed, ground, sieved, and reground (CGSR). This powder was not milled. Approximately forty-five powder particles with one dimension that is approximately 50 microns or greater are present in the SEM micrograph.

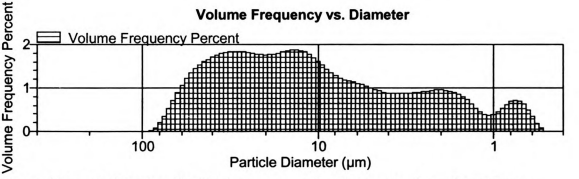

Figure 5-13—Particle size distribution, measured by light scattering using a Saturn DigiSizer, of CGSR powder from N182 (composition $Ag_{0.86}Pb_{19}Sb_{1.0}Te_{20}$). The analysis liquid used was a 28.6 wt% sucrose/degassed DI water solution. This powder was not milled. The mean is 17.8 microns and the median is 12.1 microns. Approximately 7.9 volume percent of the powder sized had a diameter of 50 microns or greater.

The factor of three difference, which is somewhat unusual, between the mean and median size is likely caused by the long tail in the particle size distribution that extends up to 100 microns. This factor of three difference between the mean and median could also be affected by a lack of repeatability between the three tests conducted on the powder sample (see Section 4.5.7.1.). (The lack of repeatability between the three tests on a powder sample will be discussed in Section 5.1.4.)

5.1.2.5.2. Batch 4 (97.2 g D = 20 mm media + 97.6 g D = 3 mm media, 150 rpm)

Figure 5-16 is an SEM micrograph of powder from N182 batch 4 and Figure 5-17 is a particle size distribution, measured by light scattering using a Saturn DigiSizer, for powder from N182 batch 4. The particle size distribution in Figure 5-17 has a mean of 3.8 microns and a median of 2.2 microns, as determined by a Saturn DigiSizer by light scattering.

Comparing Figures 5-16 and 5-17 to Figures 5-12 and 5-13, changes in the powder are apparent. In Figure 5-16, there are roughly sixteen powder particles that have one dimension that is approximately 50 microns or greater. For a similar area, roughly 1200 microns by 900 microns, in Figure 5-12, there are approximately thirty-nine powder particles with at least one dimension that is 50 microns or greater. Likewise, the particle size distributions, both measured using a Saturn DigiSizer, for the powder from N182 batch 4, Figure 5-17 and the CGSR powder from N182, Figure 5-13 respectively contained 0.0 and 7.9 volume percent particles that were 50 microns in diameter or greater. The largest powder particles in Figure 5-17 are just under 30 microns in diameter.

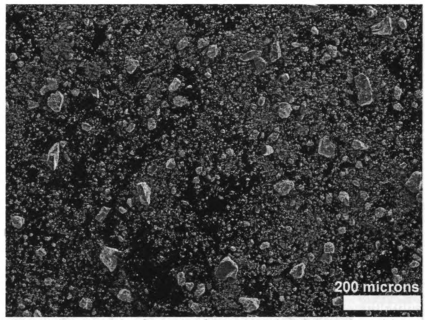

Figure 5-14—SEM micrograph of powder from N182 batch 3 (composition $Ag_{0.86}Pb_{19}Sb_{1.0}Te_{20}$). The analysis liquid used was a 28.6 wt% sucrose/degassed DI water solution. The powder was milled 3 hr at 100 rpm with a combination of mixed media (97.2 g of 20 mm diameter alumina media and 97.6 g of 3 mm diameter alumina media) in Ar. Eighteen powder particles with one dimension that is 50 microns or greater are present in the SEM micrograph.

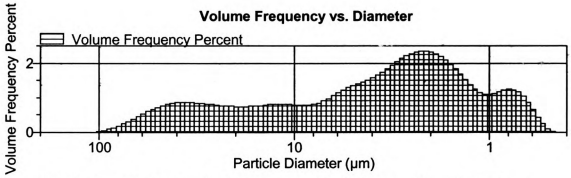

Figure 5-15—Particle size distribution, measured by light scattering using a Saturn DigiSizer, of powder from N182 batch 3 (composition $Ag_{0.86}Pb_{19}Sb_{1.0}Te_{20}$). The analysis liquid used was a 28.6 wt% sucrose/degassed DI water solution. The powder was milled 3 hr at 100 rpm with a combination of mixed media (97.2 g of 20 mm diameter alumina media and 97.6 g of 3 mm diameter alumina media) in Ar. The mean is 10.0 microns and the median is 3.2 microns. Approximately 4.4 volume percent of the powder sized had a diameter of 50 microns or greater.

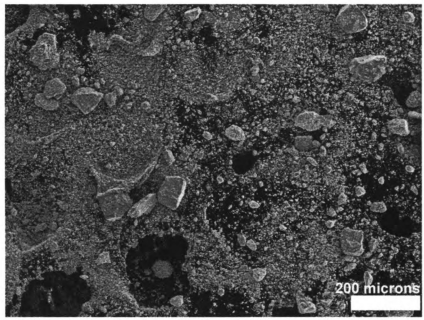

Figure 5-16—SEM micrograph of powder from N182 batch 4 (composition $Ag_{0.86}Pb_{19}Sb_{1.0}Te_{20}$). The powder was milled 3 hr at 150 rpm with a combination of mixed media (97.2 g of 20 mm diameter alumina media and 97.6 g of 3 mm diameter alumina media) in Ar. Sixteen powder particles with one dimension that is 50 microns or greater are present in the SEM micrograph.

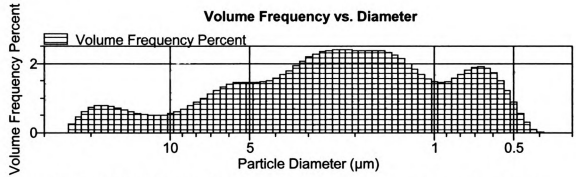

Figure 5-17—Particle size distribution, measured by light scattering using a Saturn DigiSizer, of powder from N182 batch 4 (composition $Ag_{0.86}Pb_{19}Sb_{1.0}Te_{20}$). The analysis liquid used was a 28.6 wt% sucrose/degassed DI water solution. The powder was milled 3 hr at 150 rpm with a combination of mixed media (97.2 g of 20 mm diameter alumina media and 97.6 g of 3 mm diameter alumina media) in Ar. The mean is 3.8 microns and the median is 2.2 microns. No powder particles were sized that have a diameter of 50 microns, suggesting the 50 micron diameter particles observed in Figure 5-16 were agglomerates that broke apart during the ultrasonification step in the sizing procedure.

The fact that the particle size distribution, measured by light scattering using a Saturn DigiSizer, for the powder from N182 batch 4 contains no particles that are 50 microns or greater in diameter suggests that the 50 micron or greater particles observed in Figure 5-16 were agglomerates. Any similar agglomerates in the powder specimen used to measure the particle size distribution with the Saturn DigiSizer were likely broken apart into their smaller constituent particles during the dispersion step (via ultrasonification) in the particle size analysis process (See Section 4.5.7.4.).

5.1.2.5.3. Batch 5 (97.2 g D = 20 mm media + 97.6 g D = 3 mm media, 100 rpm, 24 hr, 25 cc hexane)

Figure 5-18 is an SEM micrograph of powder from N182 batch 5 and Figure 5-19 is a particle size distribution, measured by light scattering using a Saturn DigiSizer, for powder from N182 batch 5. The particle size distribution in Figure 5-19 has a mean of 2.8 microns and a median of 1.6 microns.

Both Figure 5-18 and Figure 5-19 demonstrate that the powder particle size was reduced compared to the CGSR feedstock. In Figure 5-18, there is only one powder particle with a dimension that is 50 microns or greater. In Figure 5-12, for an area equivalent to that shown in Figure 5-18, which is approximately 300 microns by 200 microns, there are four powder particles that are have at least one dimension that is approximately 50 microns or greater.

Reduction in powder particle size can also be observed when comparing the particle size distributions, both measured using a Saturn DigiSizer, for the powder from N182 batch 5

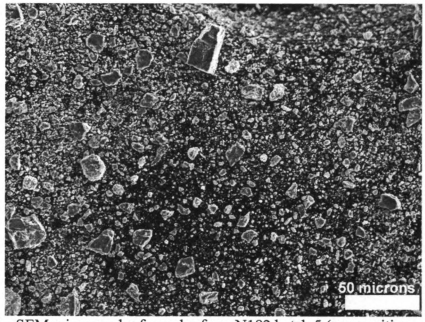

Figure 5-18—SEM micrograph of powder from N182 batch 5 (composition $Ag_{0.86}Pb_{19}Sb_{1.0}Te_{20}$). The powder was wet milled for 24 hr at 100 rpm in 25 cc of hexane with a combination of mixed media (97.2 g of 20 mm diameter alumina media and 97.6 g of 3 mm diameter alumina media) in Ar. One powder particle with one dimension that is 50 microns or greater is present in the SEM micrograph. Otherwise, virtually all the powder particles are less than 50 microns in diameter.

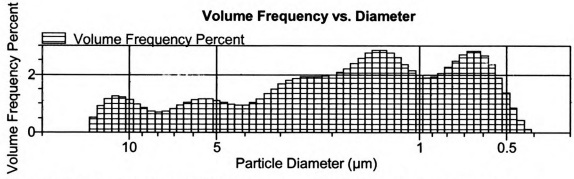

Figure 5-19—Particle size distribution, measured by light scattering using a Saturn DigiSizer, of powder from N182 batch 5 (composition $Ag_{0.86}Pb_{19}Sb_{1.0}Te_{20}$). The analysis liquid used was a 28.6 wt% sucrose/degassed DI water solution. The powder was wet milled for 24 hr at 100 rpm in 25 cc of hexane with a combination of mixed media (97.2 g of 20 mm diameter alumina media and 97.6 g of 3 mm diameter alumina media) in Ar. The mean is 2.8 microns and the median is 1.6 microns. The particle size distribution ranged from 20 to 0.4 microns.

and the N182 CGSR feedstock. As noted above, the mean and median for the powder from N182 batch 5 are 2.8 and 1.6 microns respectively. For the N182 CGSR feedstock, the mean and median are 18.2 and 12.4 microns respectively. Also, the range of powder particles measured in Figure 5-19 is from approximately 20 microns to 0.4 microns, while the powder particles in Figure 5-13 range from nearly 100 microns to 0.5 microns.

The milling procedure applied to N182 batch 5 required 24 hours of milling. The previously developed milling procedure [42], required only 3 hours to mill. As a result, the usefulness of the milling procedure applied to N182 batch 5 is debatable.

5.1.2.5.4. Batch 6 (139.9 g D = 20 mm media + 59.9 g D = 3 mm media, 100 rpm)

Figure 5-20 is an SEM micrograph of powder from N182 batch 6 and Figure 5-21 is a particle size distribution, measured by light scattering using a Saturn DigiSizer, for powder from N182 batch 6. The particle size distribution in Figure 5-21 has a mean of 6.3 microns and a median of 3.1 microns.

Figures 5-20 and 5-12 both demonstrate that the powder particle size has been reduced in N182 batch 6. In Figure 5-20, there are approximately eight powder particles that one dimension that is roughly 50 microns. For a similar area to that shown in Figure 5-20, 700 microns by 525 microns, in Figure 5-12, there are approximately eleven powder particles that have one dimension that is roughly 50 microns or greater.

Particle size reduction is also found when comparing particle size distributions, measured using a Saturn DigiSizer, for the powder from N182 batch 6 and the CGSR powder from N182. In Figure 5-13, the particle size distribution for the N182 CGSR powder, the mean and median are 18.2 microns and 12.4 microns respectively, while the

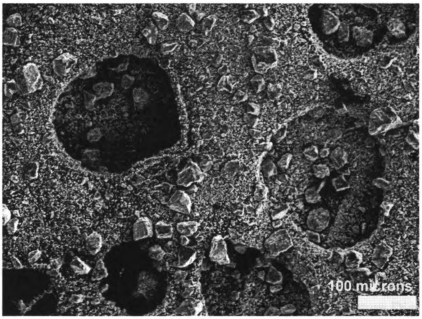

Figure 5-20—SEM micrograph of powder from N182 batch 6 (composition $Ag_{0.86}Pb_{19}Sb_{1.0}Te_{20}$). The powder was dry milled for 3 hr at 100 rpm with a combination of mixed media (139.9 g of 20 mm diameter alumina media and 59.9 g of 3 mm diameter alumina media) in Ar. The crater-like features shown in this SEM micrograph are from the carbon tape used to make the SEM specimen. Eight powder particles with one dimension that is roughly 50 microns are present in the SEM micrograph.

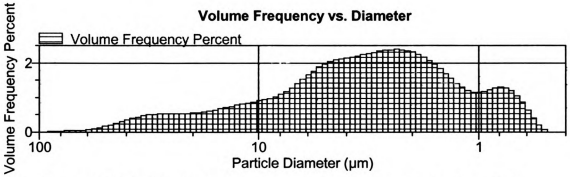

Figure 5-21—Particle size distribution, measured by light scattering using a Saturn DigiSizer, of powder from N182 batch 6 (composition $Ag_{0.86}Pb_{19}Sb_{1.0}Te_{20}$). The analysis liquid used was a 28.6 wt% sucrose/degassed DI water solution. The powder was dry milled for 3 hr at 100 rpm with a combination of mixed media (139.9 g of 20 mm diameter alumina media and 59.9 g of 3 mm diameter alumina media) in Ar. The mean is 6.3 microns and the median is 3.1 microns. Approximately 0.8 volume percent of the powder sized had a diameter of 50 microns or greater.

mean and median for the powder from N182 batch 6, Figure 5-21, are 6.3 and 3.1 microns respectively. Additionally, 7.9 volume percent the CGSR N182 powder was powder particles that were 50 microns or greater in diameter, but only 0.8 volume percent of the powder from N182 batch 6 was powder particles that were 50 microns in diameter or greater.

5.1.2.5.5. Batch 7 (62.2 g D = 20 mm media + 141.6 g D = 3 mm media, 100 rpm)

Figure 5-22 is an SEM micrograph of powder from N182 batch 7 and Figure 5-23 is a particle size distribution, measured by light scattering using a Saturn DigiSizer, for powder from N182 batch 7. The particle size distribution in Figure 5-23 has a mean of 5.8 microns and a median of 2.7 microns.

Looking at both figures, it is apparent that the powder particle size has been reduced. By comparing Figure 5-22 and a similar area in Figure 5-12, which is for powder that is only CGSR, the number of powder particles with at least one dimension with a length greater than 50 microns has been reduced from approximately six powder particles in Figure 5-12 to approximately four in Figure 5-22. Figure 5-23, the particle size distribution measured by light scattering using a Saturn DigiSizer, shows that after this milling procedure applied to N182 batch 7, there are no powder particles 50 microns in diameter or larger. However, there is still a tail in the particle size distribution, totaling 3.8 volume percent, comprised of powder particles greater than 30 microns in diameter, but less than 50 microns in diameter (Figure 5-23).

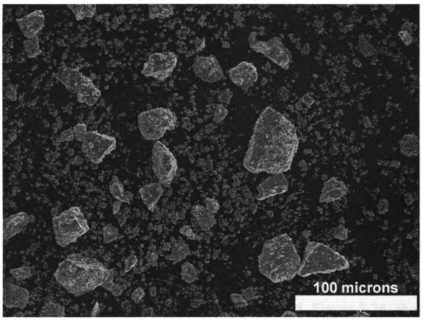

Figure 5-22—SEM micrograph of powder from N182 batch 7 (composition $Ag_{0.86}Pb_{19}Sb_{1.0}Te_{20}$). The powder was dry milled for 3 hr at 100 rpm with a combination of mixed media (62.2 g of 20 mm diameter alumina media and 141.6 g of 3 mm diameter alumina media) in Ar. Four powder particles with one dimension that is roughly 50 microns or greater are present in the SEM micrograph, compared to six powder particles with one dimension that is 50 microns or greater for a similar area in Figure 5-12 (approximately 350 by 250 microns).

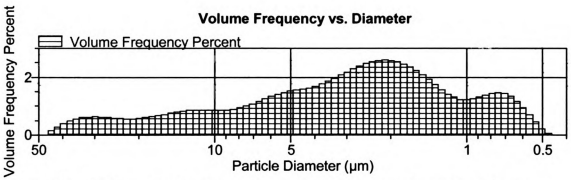

Figure 5-23—Particle size distribution, measured by light scattering using a Saturn DigiSizer, of powder from N182 batch 7 (composition $Ag_{0.86}Pb_{19}Sb_{1.0}Te_{20}$). The analysis liquid used was a 28.6 wt% sucrose/degassed DI water solution. The powder was dry milled for 3 hr at 100 rpm with a combination of mixed media (62.2 g of 20 mm diameter alumina media and 141.6 g of 3 mm diameter alumina media) in Ar. The mean is 5.8 microns and the median is 2.7 microns. Approximately 3.8 volume percent of the powder sized had a diameter between 30 and 50 microns.

5.1.2.5.6. Batch 8 (previously developed wet milling procedure, 25 cc hexane)

Figure 5-24 is an SEM micrograph of powder from N182 batch 8 and Figure 5-25 is a particle size distribution, measured by light scattering using a Saturn DigiSizer, for powder from N182 batch 8. The particle size distribution in Figure 5-25 has a mean of 4.4 microns and a median of 1.8 microns. (The variation between the mean and median, which is almost a factor of three, could partly be caused by a lack of repeatability between the individual tests conducted on a powder sample. See Section 5.1.4. for a discussion on the lack of repeatability between tests.)

The SEM micrograph of powder from N182 batch 8, Figure 5-24, shows one particle with dimensions on the order of hundreds of microns and at least ten other powder particles that have one dimension that is approximately 50 microns. For a similar area, 1500 microns by 1100 microns, in Figure 5-12, an SEM micrograph of powder that is only CGSR, there are forty-five powder particles that have one dimension that is at approximately 50 microns or more.

The particle size distribution for powder from N182 batch 8, Figure 5-25, measured by light scattering using a Saturn DigiSizer, disagrees with what was observed via SEM. In Figure 5-25, the largest powder particle measured is approximately 30 microns in diameter. This difference in largest powder particle size may be the result of population sampling, i.e. the powder specimen dispersed for particle size measurement using the Saturn DigiSizer may not have included any powder particles with a diameter greater than 30 microns. Another possibility is that the largest powder particles are agglomerates, and the dispersion process for particle size analysis broke these agglomerates into their smaller constituent particles.

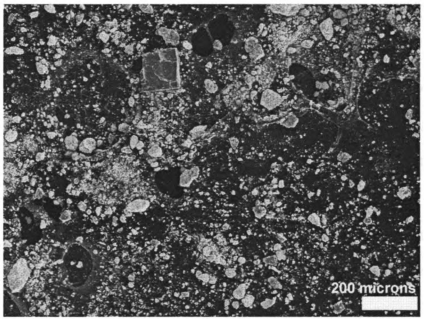

Figure 5-24—SEM micrograph of powder from N182 batch 8 (composition $Ag_{0.86}Pb_{19}Sb_{1.0}Te_{20}$). The powder was dry milled for 3 hr at 100 rpm with ten 20 mm diameter alumina media in Ar, then wet milled for 24 hr at 150 rpm in 25 cc hexane with 250 cc of 3 mm diameter alumina media in Ar. Ten powder particles with one dimension that is approximately 50 microns, and one powder particle with dimensions on the order of hundreds of microns are present in the SEM micrograph. The craters observed in the SEM micrograph are naturally occurring features of the carbon tape used to make the SEM specimen.

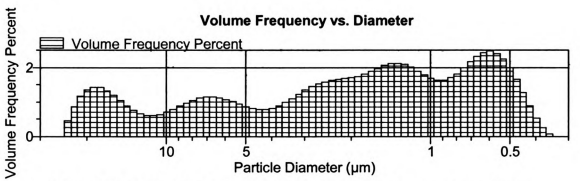

Figure 5-25—Particle size distribution, measured by light scattering using a Saturn DigiSizer, of powder from N182 batch 8 (composition $Ag_{0.86}Pb_{19}Sb_{1.0}Te_{20}$). The analysis liquid used was a 28.6 wt% sucrose/degassed DI water solution. The powder was dry milled for 3 hr at 100 rpm with ten 20 mm diameter alumina media in Ar, then wet milled for 24 hr at 150 rpm in 25 cc hexane with 150 cc of 3 mm diameter alumina media in Ar. The mean is 4.4 microns and the median is 1.8 microns. The largest powder particle measured had a diameter of approximately 30 microns.

Regardless of the discrepancies between SEM observations and the particle size distribution, the powder particle size has been reduced. As mentioned above, the number of powder particles 50 microns across or larger has been reduced to approximately ten in Figure 5-24, compared to forty-five particles 50 microns across or larger in Figure 5-12. Also, the particle size distribution has a largest particle of approximately 30 microns, a mean of 4.4 microns, and a median of 1.8 microns. For powder that was only CGSR, the largest particle, mean, and median of the particle size distribution were approximately 90 microns, 18.2 microns, and 12.4 microns, respectively. However, it should be noted that this powder batch required a total milling time of 27 hours.

5.1.2.5.7. Batch 9 (137.7 g D = 20 mm media + 58.8 g D = 3 mm media, 100 rpm, 6 hours)

Figure 5-26 is an SEM micrograph of powder from N182 batch 9 and Figure 5-27 is a particle size distribution, measured by light scattering using a Saturn DigiSizer, for powder from N182 batch 9. The particle size distribution in Figure 5-27 has a mean of 6.8 microns and a median of 4.1 microns.

Comparing Figures 5-26 and 5-12 demonstrates that the powder particle size has been reduced in N182 batch 9. In Figure 5-26, there are approximately nine powder particles with one dimension that is at least 50 microns. For a similar area to that shown in Figure 5-26, roughly 1200 microns by 900 microns, in Figure 5-12, there are approximately thirty-nine powder particles that have one dimension that is roughly 50 microns or greater.

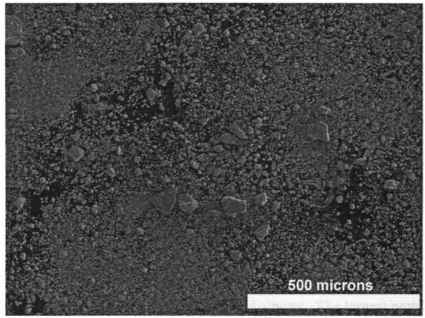

Figure 5-26—SEM micrograph of powder from N182 batch 9 (composition $Ag_{0.86}Pb_{19}Sb_{1.0}Te_{20}$). The powder was dry milled for 6 hr at 100 rpm with a combination of mixed media (137.7 g of 20 mm diameter alumina media and 58.8 g of 3 mm diameter alumina media) in Ar. Nine powder particles with one dimension that is at least 50 microns are present in the SEM micrograph.

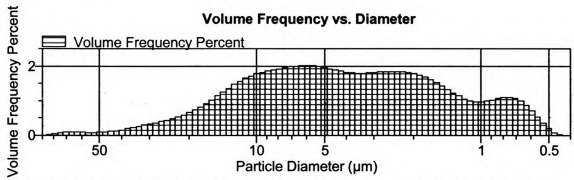

Figure 5-27—Particle size distribution, measured by light scattering using a Saturn DigiSizer, of powder from N182 batch 9 (composition $Ag_{0.86}Pb_{19}Sb_{1.0}Te_{20}$). The analysis liquid used was a 28.6 wt% sucrose/degassed DI water solution. The powder was dry milled for 6 hr at 100 rpm with a combination of mixed media (137.7 g of 20 mm diameter alumina media and 58.8 g of 3 mm diameter alumina media) in Ar. The mean is 6.8 microns and the median is 4.1 microns. Approximately 0.8 volume percent of the powder sized had a diameter of 50 microns or greater. The largest powder particles measured were approximately 80 microns in diameter.

Powder particle size reduction is found when comparing particle size distributions, measured using a Saturn DigiSizer, for the powder from N182 batch 9 and the CGSR powder from N182. In Figure 5-13, the particle size distribution for the N182 CGSR powder, the mean and median are 18.2 microns and 12.4 microns respectively, while the mean and median for the powder from N182 batch 9, Figure 5-27, are 6.8 and 4.1 microns respectively. Additionally, the CGSR N182 powder contained 7.9 volume percent powder particles that were 50 microns or greater in diameter, while 0.8 volume percent of the powder particles measured in the particle size distribution, using a Saturn DigiSizer, from N182 batch 9 were 50 microns in diameter. The largest powder particles measured in the powder from N182 batch 9 were approximately 80 microns in diameter.

5.1.2.5.8. Batch 10, Dry Milled (137.8 g D = 20 mm media + 60.0 g D = 3 mm media, 100 rpm, two 3 hr cycles)

Figure 5-28 is an SEM micrograph of dry milled powder from N182 batch 10, Figure 5-29 is an SEM micrograph of an agglomerate from N182 batch 10 after dry milling, and Figure 5-30 is shows a particle size distribution, measured by light scattering using a Saturn DigiSizer, for powder from dry milled N182 batch 10. The particle size distribution in Figure 5-30 has a mean of 8.4 microns and a median of 3.9 microns.

At first glance, the powder observed in Figure 5-28 is unremarkable. The area shown in Figure 5-28, which is approximately 275 microns by 225 microns, contains approximately six powder particles that have one dimension that approaches 50 microns or is greater than 50 microns. Adding to the seemingly less than enthusiastic results is the fact that some of these "large" powder particles seen in Figure 5-28 may be hard

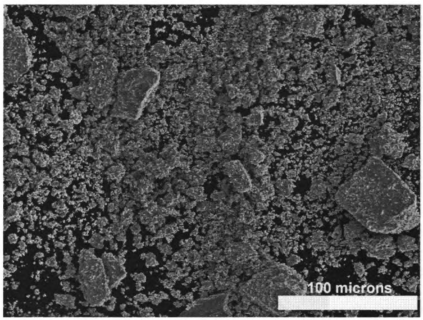

Figure 5-28—SEM micrograph of powder from N182 batch 10 (composition $Ag_{0.86}Pb_{19}Sb_{1.0}Te_{20}$) that was only dry milled. The powder was dry milled for a total time of 6 hr (separated into two 3 hr long segments) at 100 rpm with a combination of mixed media (137.8 g of 20 mm diameter alumina media and 60.0 g of 3 mm diameter alumina media) in Ar. Between milling segments, the powder caked to the sides of the milling jar was scraped loose. Six powder particles with one dimension that is at least 50 microns are present in the SEM micrograph. Some of these powder particles with dimensions of 50 microns or greater may be hard agglomerates.

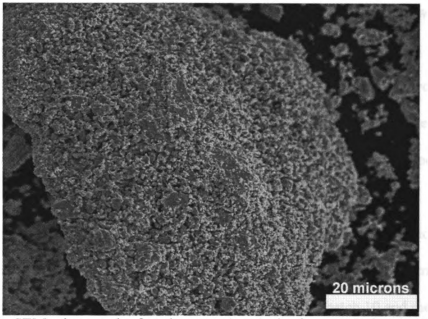

Figure 5-29—SEM micrograph of agglomerate in powder from N182 batch 10 (composition $Ag_{0.86}Pb_{19}Sb_{1.0}Te_{20}$) that was only dry milled. The powder was dry milled for a total time of 6 hr (separated into two 3 hr long segments) at 100 rpm with a combination of mixed media (137.8 g of 20 mm diameter alumina media and 60.0 g of 3 mm diameter alumina media) in Ar. Between milling segments, the powder caked to the sides of the milling jar was scraped loose. This agglomerate appears to be a hard agglomerate and has dimensions that exceed 50 microns.

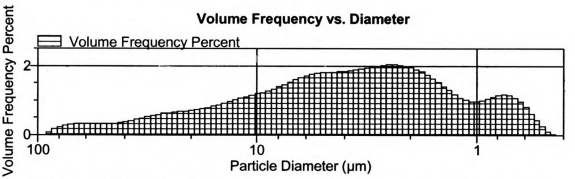

Figure 5-30—Particle size distribution, measured by light scattering using a Saturn DigiSizer, of powder from N182 batch 10 (composition $Ag_{0.86}Pb_{19}Sb_{1.0}Te_{20}$) that was only dry milled. The analysis liquid used was a 28.6 wt% sucrose/degassed DI water solution. The powder was dry milled for a total time of 6 hr (separated into two 3 hr long segments) at 100 rpm with a combination of mixed media (137.8 g of 20 mm diameter alumina media and 60.0 g of 3 mm diameter alumina media) in Ar. Between milling segments, the powder caked to the sides of the milling jar was scraped loose. The mean is 8.4 microns and the median is 3.9 microns. Approximately 3.1 volume percent of the powder sized had a diameter of 50 microns or greater.

agglomerates with dimensions greater than 50 microns. A hard agglomerate with dimensions exceeding 50 microns is observed in Figure 5-29.

Hard agglomerates are detrimental to a bulk specimen made from powders because during sintering, the hard agglomerate densifies more quickly than the non-agglomerated powder surrounding. As a result, internal stresses, cracks, and pores can be generated in the sintered body [96-97].

Despite the qualitative analysis of the SEM micrographs, some reduction in the powder particle size is observed by comparing the particle size distributions, measured using a Saturn DigiSizer, of the dry milled powder from N182 batch 10 and the N182 CGSR feedstock. The particle size distribution for the powder after dry milling N182 batch 10, Figure 5-30, has a mean of 8.4 microns, a median of 3.9 microns, and shows 3.1 volume percent of the powder specimen sized had a diameter equal to or greater than 50 microns. Figure 5-13, the particle size distribution for the N182 CGSR feedstock has a mean of 18.2 microns, a median of 12.4 microns, and shows that 7.9 volume percent of the powder specimen sized had a diameter equal to or greater than 50 microns.

5.1.2.5.9. Batch 10, Wet Milled (137.8 g D = 20 mm media + 60.0 g D = 3 mm media, 100 rpm, 6 hr, 25 cc hexane)

Figure 5-31 is an SEM micrograph of wet milled powder from N182 batch 10, Figure 5-32 (an SEM micrograph) features an agglomerate from N182 batch 10 after wet milling, and Figure 5-33 is a particle size distribution, measured by light scattering using a Saturn DigiSizer, for powder from wet milled N182 batch 10. The particle size distribution (Figure 5-33) has a mean of 2.2 microns and a median of 1.6 microns.

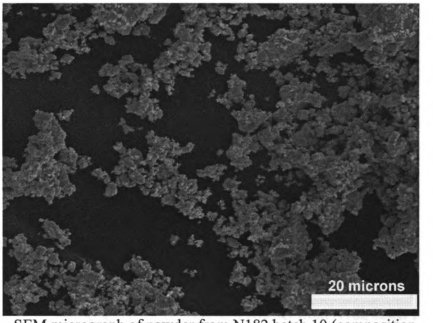

Figure 5-31—SEM micrograph of powder from N182 batch 10 (composition $Ag_{0.86}Pb_{19}Sb_{1.0}Te_{20}$) that was dry milled and then wet milled. The powder was dry milled for a total time of 6 hr (separated into two 3 hr long segments) at 100 rpm with a combination of mixed media (137.8 g of 20 mm diameter alumina media and 60.0 g of 3 mm diameter alumina media) in Ar, then wet milled for 6 hr at 100 rpm with 25 cc of hexane using the same media in Ar. Between milling segments, the powder caked to the sides of the milling jar was scraped loose. Most of the powder particles observed are smaller than 20 microns in diameter, and more than half the powder particles appear to be 4 microns in diameter or smaller.

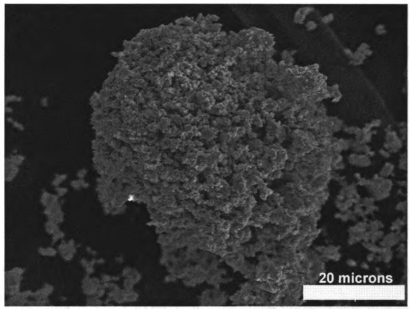

Figure 5-32—SEM micrograph of agglomerate in powder from N182 batch 10 (composition $Ag_{0.86}Pb_{19}Sb_{1.0}Te_{20}$) that was dry milled and then wet milled. The powder was dry milled for a total time of 6 hr (separated into two 3 hr long segments) at 100 rpm with a combination of mixed media (137.8 g of 20 mm diameter alumina media and 60.0 g of 3 mm diameter alumina media) in Ar, then wet milled for 6 hr at 100 rpm with 25 cc of hexane using the same media in Ar. Between milling segments, the powder caked to the sides of the milling jar was scraped loose. The agglomerate appears to be softer than the agglomerate in Figure 5-29, meaning it is likely less detrimental to the sintered material.

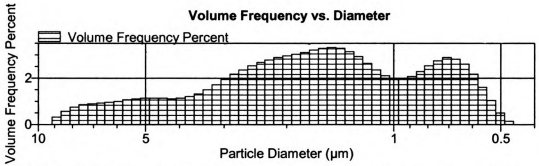

Figure 5-33—Particle size distribution, measured by light scattering using a Saturn DigiSizer, of powder from N182 batch 10 (composition $Ag_{0.86}Pb_{19}Sb_{1.0}Te_{20}$) after 6 total hours of dry milling and 6 hours of wet milling in 25 cc hexane. The analysis liquid used was a 28.6 wt% sucrose/degassed DI water solution. The powder was dry milled in two 3 hr long segments at 100 rpm with a combination of mixed media (137.8 g of 20 mm diameter alumina media and 60.0 g of 3 mm diameter alumina media) in Ar, then wet milled for 6 hr at 100 rpm with 25 cc of hexane using the same media in Ar. Between milling segments, the powder caked to the sides of the milling jar was scraped loose. The mean is 2.2 microns and the median is 1.6 microns. The largest particle sized was approximately 9 microns in diameter, suggesting that the largest particles in the powder are agglomerates that break up during ultrasonification.

Most of the powder particles from N182 batch 10 after wet milling are smaller than 20 microns in diameter (Figure 5-31). In fact, over half the powder particles observed in Figure 5-31 appear to be 4 microns in diameter or smaller, which is roughly consistent with a median powder particle size of 1.6 microns as determined by the Saturn DigiSizer.

Although most of the powder particles from N182 batch 10 after wet milling is less than 20 microns in diameter, some particles with dimensions exceeding 20 microns are present. Figure 5-32 is an SEM micrograph of an agglomerate that is roughly 60 microns long along one axis and 40 microns wide along the perpendicular axis. Besides being smaller than the agglomerate in Figure 5-29, the agglomerate in Figure 5-32 also appears to be a softer agglomerate, since the agglomerate included in Figure 5-32 exhibits considerably greater surface-breaking porosity than is apparent in the agglomerate included in Figure 5-29. Soft agglomerates are not as detrimental to a sintered component's strength because their densification rate does not differ greatly from the powder that surrounds them, so large pores do not form from soft agglomerates. Also, soft agglomerates tend to deform when pressed, allowing for a uniformly dense green body to be formed prior to sintering [98].

Figure 5-33, the particle size distribution for N182 batch 10 after wet miling, measured using a Saturn DigiSizer, presents very encouraging results. As noted above, the particles size distribution's mean is 2.2 microns and the median is 1.6 microns. Additionally, the largest particle measured by the Saturn was approximately 9 microns in diameter. This suggests that the particles greater than 10 microns in diameter observed in

the SEM were likely agglomerates that broke apart during the dispersion step in the particle size analysis.

5.1.3. Milling Scale-up with Mixed Media

5.1.3.1. N182 Batch 11 (Scale-up to 50 g Powder Charge)

Figure 5-34 is an SEM micrograph of powder from N182 batch 11 after six hours of dry milling. Figure 5-34 contains approximately twenty-one powder particles with one dimension that is approximately 50 microns. In a similar area, 900 microns by 1200 microns, from Figure 5-12 there are approximately thirty-nine powder particles with one dimension that is at least 50 microns. For this reason, it is concluded that limited powder particle size reduction was caused by this milling treatment.

A particle size distribution, measured by light scattering using a Saturn DigiSizer was measured for N182 batch 11, but because of a lack of repeatability between tests conducted on the sample, it will not be further discussed.

5.1.3.2. N182 Batch 12 (Scale-up to 35 g Powder Charge)

Figure 5-35 is an SEM micrograph of powder from N182 batch 12. In Figure 5-35, there are twenty-seven powder particles with one dimension that is approximately 50 microns or greater. Comparatively, in Figure 5-12, which is for the CGSR feedstock, in an area 1000 microns by 1400 microns, there are forty-three powder particles with one dimension that is approximately 50 microns or greater. The milling procedure applied to N128 batch 12 is concluded to be ineffective because limited reduction in powder particle size indicated by comparing SEM micrographs.

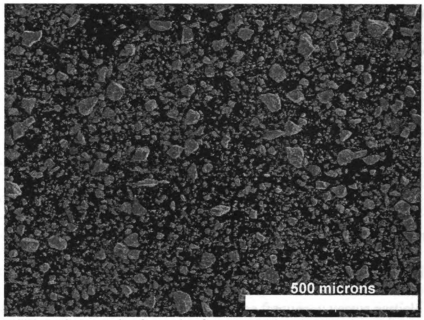

Figure 5-34—SEM micrograph of powder from N182 batch 11 (composition $Ag_{0.86}Pb_{19}Sb_{1.0}Te_{20}$). The powder is an attempt to increase the powder batch size to 50 g with mixed media. The powder was dry milled for a total of 6 hr (broken into two 3 hr segments) at 100 rpm with mixed media (198.7 g of 20 mm diameter alumina media and 90.0 g of 3 mm diameter alumina media) in Ar. Between milling segments, the powder caked to the sides of the milling jar was scraped loose. In the area shown in this SEM micrograph, which is approximately 1200 microns x 900 microns, there are approximately 20 powder particles with at least one dimension that is approximately 50 microns or greater.

A particle size distribution, measured by light scattering using a Saturn DigiSizer was measured for N182 batch 12, but because of a lack of repeatability between tests conducted on the sample, it will not be further discussed.

5.1.4. Comment on Test Repeatability During Particle Size Distribution Measurement Using Saturn DigiSizer

In Section 4.5.7.1., it is stated that during the particle size measurements made with a Saturn DigiSizer via light scattering, three tests were conducted on a given powder sample. In a perfect world, plots of powder volume frequency versus particle diameter for each test would be identical and directly on top of one another. This is not the case, though. For all the particle size distributions above, the powder volume frequency versus particle diameter plots for the different tests lack repeatability. This lack of repeatability is more severe for some powder samples than others, but it is present in all the measurements shown above.

Figure 5-36 is a powder volume frequency versus particle diameter plot from the particle size distribution measurement of powder from N182 batch 3. Figure 5-36, while not a representation of the lack of repeatability for all the particle size distribution measurements above, clearly demonstrates the general trends in the lack of repeatability seen in the volume frequency versus particle diameter plots from all the particle size distributions. Between Test 1 and Test 3, the number of powder particles 50 microns in diameter decreases, while the number of 3 micron diameter powder particles increases. Such behavior is indicative of agglomerates in the powder sample separating into their

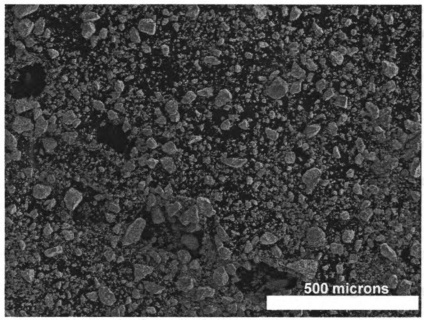

Figure 5-35—SEM micrograph of powder from N182 batch 12 (composition $Ag_{0.86}Pb_{19}Sb_{1.0}Te_{20}$). The powder is an attempt to increase the powder batch size to 35 g with mixed media. The powder was dry milled for 3 hr at 100 rpm with mixed media (198.7 g of 20 mm diameter alumina media and 90.3 g of 3 mm diameter alumina media) in Ar. In the area shown in this SEM micrograph, which is approximately 1375 microns x 1025 microns, there are approximately 26 powder particles with at least one dimension that is approximately 50 microns or greater.

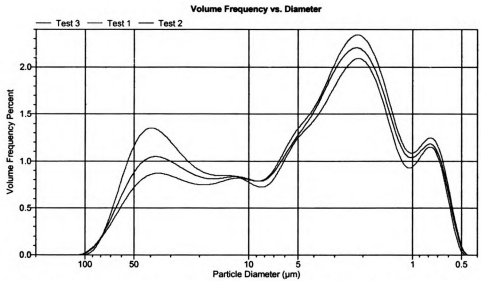

Figure 5-36—Frequency plot from particle size analysis of powder from N182 batch 3. Notice that between Test 1 and Test 3, the number of powder particles approximately 50 microns in diameter decreases and the number of powder particles approximately 3 microns in diameter increases. This increase in "small" particles with time in the Saturn, along with the concurrent decrease in "large" particles suggests that agglomerates in the powder are separating as the powder sample circulates through the Saturn.

smaller constituent powder particles as the powder circulates through the Saturn during particle size distribution measurement.

5.1.5. Reevaluation of Laser Scattering Particle Size Distribution Measurements

Figure 5-37 through Figure 5-42 are particle size distributions measured via light scattering using a Saturn DigiSizer with a 40 wt% sucrose/degassed DI water as the analysis liquid. Figures 5-37 through 5-42 are particle size distributions for selected powders from the N182 milling experiments (Section 4.3.2.7.). Figure 5-37 is for CGSR feedstock from N182. Figure 5-38 is for powder from N182 batch 4. Figure 5-39 is for powder from N182 batch 5. Figure 5-40(a-c) is for powder from N182 batch 6. Figure 5-41 is for powder from N182 batch 9. Figure 5-42(a-b) is for powder from N182 batch 10 after both dry and wet milling.

Table 5-1 compares the means and medians from the particle size distributions for the selected powders from the N182 milling experiments on the basis of the analysis liquids used (28.6 wt% sucrose or 40 wt% sucrose). Based on the comparisons between the various means and medians, it appears that particle size distributions are comparable. No clear trend is apparent as to how having the analysis liquid and index of refraction correctly paired alters the particle size distributions. In some cases, when the analysis liquid and refractive index are correctly paired, the mean and median are increased, while in other cases the mean and median are reduced.

If the particle size distribution from Figure 5-40a, which seems slightly anomalous, is ignored in Table 5-1, it appears that the differences between the particle size distributions based on the different analysis liquids are a result of the change in the

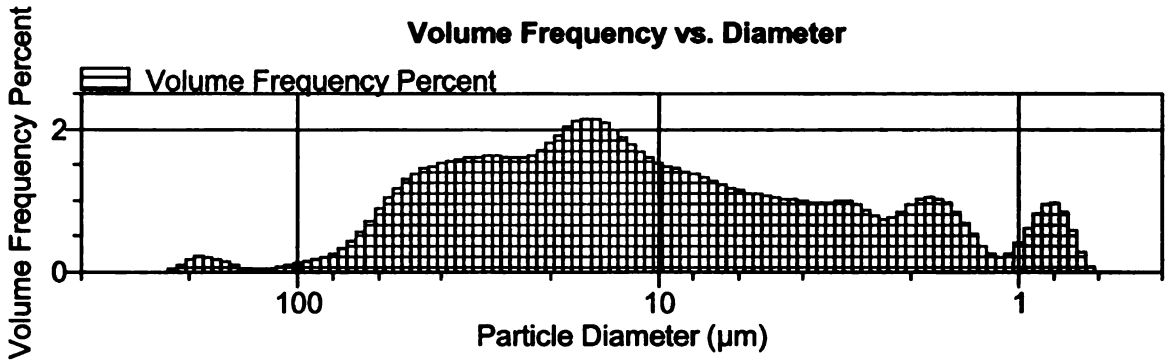

Figure 5-37—Particle size distribution, measured by light scattering using a Saturn DigiSizer, of CGSR powder from N182 (composition $Ag_{0.86}Pb_{19}Sb_{1.0}Te_{20}$). The analysis liquid used was a 40 wt% sucrose/degassed DI water solution. This powder was not milled. The mean is 20.1 microns and the median is 12.4 microns.

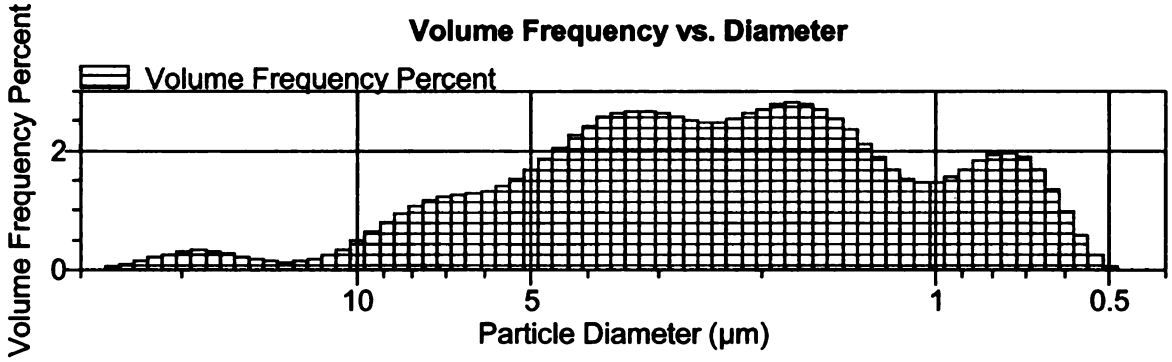

Figure 5-38—Particle size distribution, measured by light scattering using a Saturn DigiSizer, of powder from N182 batch 4 (composition $Ag_{0.86}Pb_{19}Sb_{1.0}Te_{20}$). The analysis liquid used was a 40 wt% sucrose/degassed DI water solution. The powder was milled 3 hr at 150 rpm with a combination of mixed media (97.2 g of 20 mm diameter alumina media and 97.6 g of 3 mm diameter alumina media) in Ar. The mean is 3.3 microns and the median is 2.3 microns. No powder particles were sized that have a diameter of 50 microns, suggesting the 50 micron diameter particles observed in Figure 5-16 were agglomerates that broke apart during the ultrasonification step in the sizing procedure.

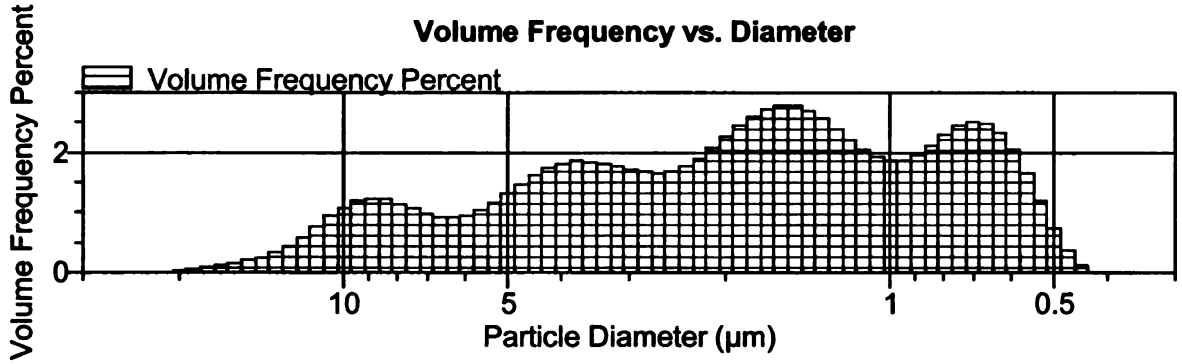

Figure 5-39—Particle size distribution, measured by light scattering using a Saturn DigiSizer, of powder from N182 batch 5 (composition $Ag_{0.86}Pb_{19}Sb_{1.0}Te_{20}$). The analysis liquid used was a 40 wt% sucrose/degassed DI water solution. The powder was wet milled for 24 hr at 100 rpm in 25 cc of hexane with a combination of mixed media (97.2 g of 20 mm diameter alumina media and 97.6 g of 3 mm diameter alumina media) in Ar. The mean is 3.0 microns and the median is 1.8 microns. The particle size distribution ranged from 20 to 0.4 microns.

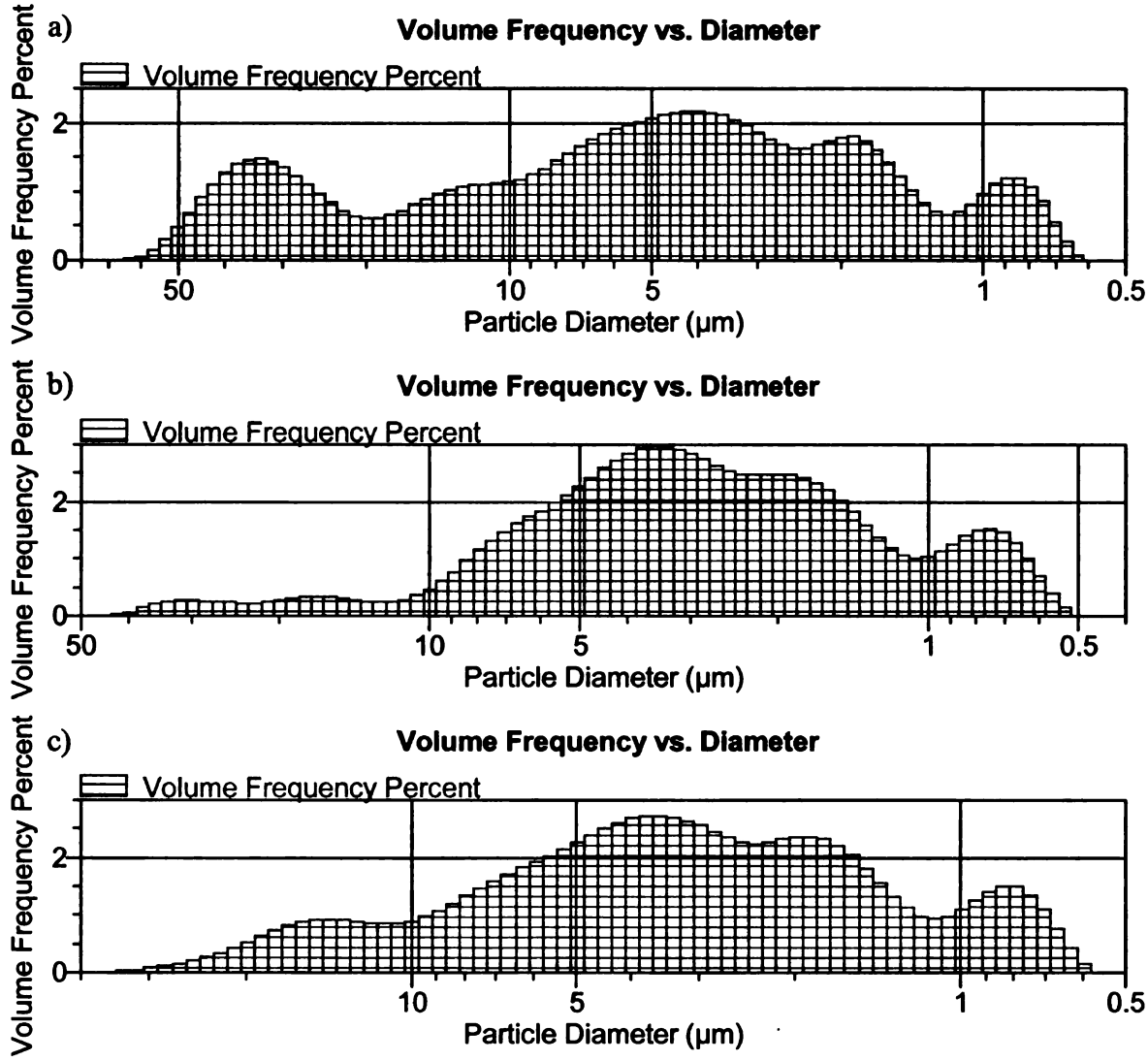

Figure 5-40—Particle size distributions, measured by light scattering using a Saturn DigiSizer, of powder from N182 batch 6 (composition $Ag_{0.86}Pb_{19}Sb_{1.0}Te_{20}$). The analysis liquid used was a 40 wt% sucrose/degassed DI water solution. The powder was dry milled for 3 hr at 100 rpm with a combination of mixed media (139.9 g of 20 mm diameter alumina media and 59.9 g of 3 mm diameter alumina media) in Ar. The means are: a)10.2 microns, b)4.3 microns, and c)4.9 microns. The medians are: a)4.8 microns, b)2.9 microns, and c)3.3 microns.

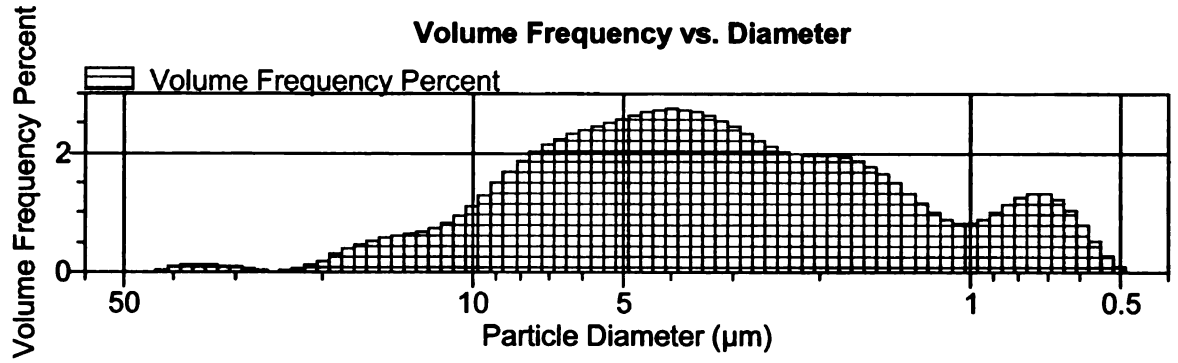

Figure 5-41—Particle size distribution, measured by light scattering using a Saturn DigiSizer, of powder from N182 batch 9 (composition $Ag_{0.86}Pb_{19}Sb_{1.0}Te_{20}$). The analysis liquid used was a 40 wt% sucrose/degassed DI water solution. The powder was dry milled for 6 hr at 100 rpm with a combination of mixed media (137.7 g of 20 mm diameter alumina media and 58.8 g of 3 mm diameter alumina media) in Ar. The mean is 4.6 microns and the median is 3.4 microns.

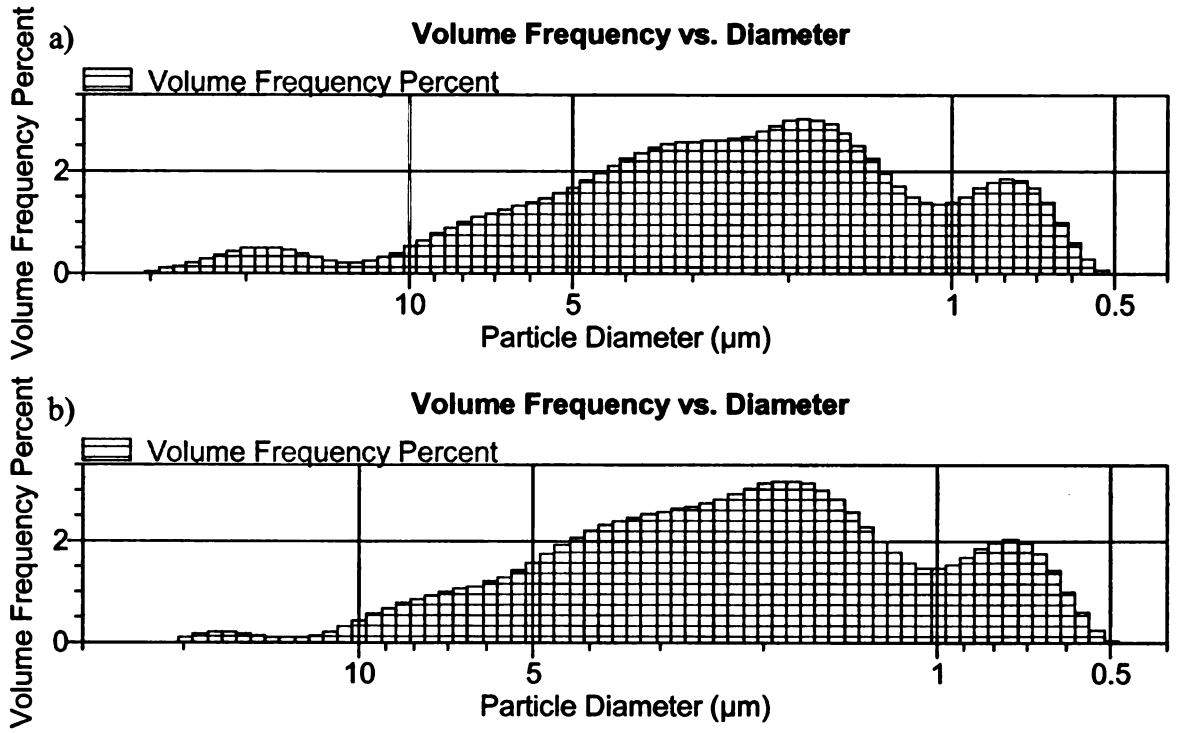

Figure 5-42—Particle size distribution, measured by light scattering using a Saturn DigiSizer, of powder from N182 batch 10 (composition $Ag_{0.86}Pb_{19}Sb_{1.0}Te_{20}$) after 6 total hours of dry milling and 6 hours of wet milling in 25 cc hexane. The analysis liquid used was a 40 wt% sucrose/degassed DI water solution. The powder was dry milled for a total time of 6 hr (separated into two 3 hr long segments) at 100 rpm with a combination of mixed media (137.8 g of 20 mm diameter alumina media and 60.0 g of 3 mm diameter alumina media) in Ar, then wet milled for 6 hr at 100 rpm with 25 cc of hexane using the same media in Ar. Between milling segments, the powder caked to the sides of the milling jar was scraped loose. The means are: a)3.8 microns, and b)2.9 microns. The medians are: a)2.4 microns, and b)2.1 microns.

Table 5-1—Comparison of means medians from particle size distributions (measured by light scattering using a Saturn DigiSizer) for selected powders from the N182 (composition $Ag_{0.86}Pb_{19}Sb_{1.0}Te_{20}$) milling experiments. Recall that the particle size distributions measured with a 28.6 wt% sucrose/degassed DI water solution as the analysis liquid are the average of three tests, while the particle size distributions measured with a 40 wt% sucrose/degassed DI water solution as the analysis liquid are the average of eight tests.

Powder Batch	28.6 wt% Sucrose Measurements		40 wt% Sucrose Measurements	
	Mean (microns)	Median (microns)	Mean (microns)	Median (microns)
CGSR	18.2	12.4	20.1	12.4
4	3.9	2.2	3.3	2.3
5	2.8	1.6	3.0	1.8
6	6.4	3.1	a) 10.2 b) 4.3 c) 4.9	4.8 2.9 3.3
9	6.9	4.2	4.6	3.4
10	2.2	1.6	a) 3.8 b) 2.9	2.4 2.1

refractive index. The differences between the particle size distributions for a given powder batch, when compared across the different analysis liquids, are typically more than one micron. When comparing particle size distributions between different test samples, but using the same analysis liquid, the differences are less than one micron.

5.2. Milling Jar and Milling Media Cleaning

5.2.1. Identification of Unknown Powder Resulting from Aqua Regia Cleaning

Figure 5-43 is an EDS spectrum for the unknown white powder that was collected off the 3 mm diameter alumina media after cleaning with aqua regia. Based on the EDS spectrum, the unknown powder was comprised of lead and chlorine. EDS was conducted so that identifying the appropriate JCPDS file for the unknown white powder would be easier.

Figure 5-44 is an XRD pattern for the unknown white powder that was collected off the 3 mm diameter alumina media after cleaning with aqua regia. The referenced XRD pattern is from the JCPDS data for $PbCl_2$. It was concluded that the unknown white powder was $PbCl_2$ based on the agreement between the XRD pattern for the unknown powder and the given JCPDS data for $PbCl_2$.

The question then becomes: where did the Pb and Cl come from to make the $PbCl_2$? The Cl likely came from the HCl after the H^+ ions dissociated to create the acid. The Pb likely came from the LAST or LASTT being cleaned from the 3 mm diameter alumina media. As the aqua regia dissolved the LAST or LASTT covering the media, it is not unreasonable to think that some of the Pb from the LAST/LASTT was available to react with the Cl.

After white powder was identified as $PbCl_2$, a material safety data sheet (MSDS) was found for $PbCl_2$. The MSDS states that $PbCl_2$ is corrosive and is capable of causing corneal damage, blindness, skin blistering, and irritation of the gastro-intestinal tract or respiratory tract [99]. In response, $PbCl_2$ will only be worked with inside a fume hood while wearing at least goggles, a lab coat, and gloves.

It should also be noted that $PbCl_2$ is an n-type dopant for PbTe.

5.3. Testing

5.3.1. Vickers hardness

Table 5-2 shows the Vickers hardness of selected specimens. MSUHP-1E, MSUHP-1F, MSUHP-3-1, and MSUHP-3-2 were legs from n-type hot pressed billets of the composition $Ag_{0.43}Pb_{18}Sb_{1.2}Te_{20}$. MSUHP-4B and MSUHP-4C were specimens from a p-type hot pressed billet of composition $Ag_{0.9}Pb_9Sb_{0.6}Sn_9Te_{20}$. JPL HP was a specimen from a billet, of composition $Ag_{0.43}Pb_{18}Sb_{1.2}Te_{20}$, hot pressed at Jet Propulsion Laboratories in Pasadena, CA. N155 B6 and N156 D2 were slow-cooled ingot specimens from two different ingots, both of which had the composition $Ag_{0.86}Pb_{19}Sb_{1.0}Te_{20}$. Some of the hardness data presented in Table 5-2 is reported in a paper accepted for publication in an MRS proceedings [62], but additional results for specific legs are reported in this thesis.

The Vickers hardness values for MSUHP-1E, MSUHP-1F, MSUHP-3-1, MSUHP-3-2, JPL HP, N155 B6, and N156 D2 all compare well to those reported for LAST ingot material [22]. In [22], the Vickers hardness for LAST ingots of a variety of compositions ranged from 0.526 to 0.922 GPa. All of the Vickers

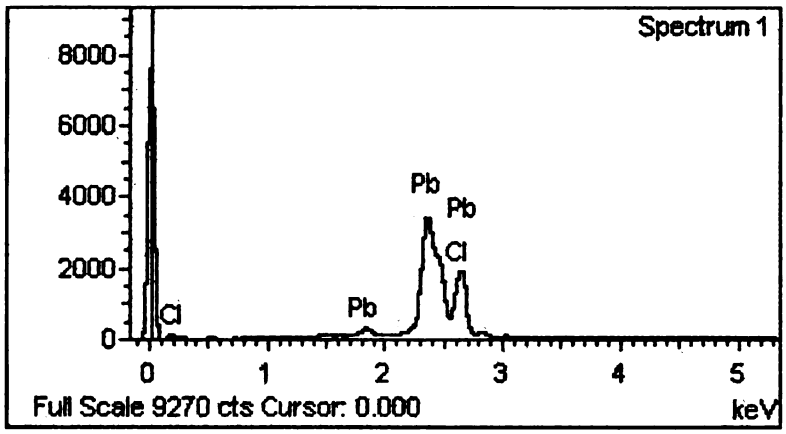

Figure 5-43—EDS spectrum for a specimen of the unknown white powder resulting from the cleaning of the 3 mm diameter spherical alumina media with aqua regia. The EDS was conducted using a 20 keV accelerating voltage and a working distance of 15 mm over 2 min. The elements detected are lead and chlorine.

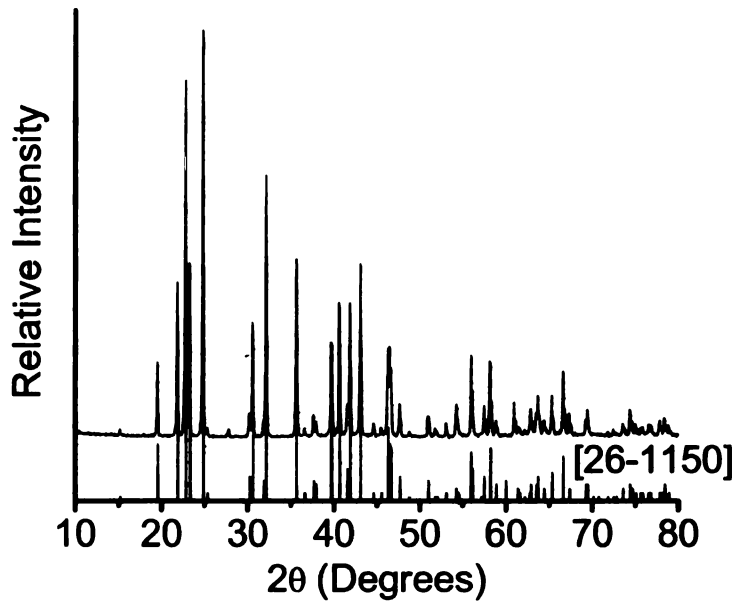

Figure 5-44—XRD pattern from a specimen of the unknown white powder resulting from the cleaning of the 3mm diameter spherical alumina media with aqua regia and the XRD pattern for $PbCl_2$ from JCPDS data. The XRD scan was conducted across a 2-theta of 10 to 80° with a step size of 0.05° using Cu $K_{\alpha 1}$ radiation. It was concluded the unknown white powder is $PbCl_2$.

hardness data measured for the hot pressed LAST specimens ranged from 0.701 to 0.879 GPa which fall within the range of Vickers hardness values reported in [22]. Likewise, the Vickers microhardness values for N155 B6 and N156 D2, which are 0.630 and 0.570 GPa also fall within the values reported in [22].

The Vickers hardness for the LASTT hot pressed specimens, MSUHP-4B and MSUHP-4C, differ slightly from the hardness data presented in [22]. As noted above, the maximum hardness reported in [22] is 0.922 GPa. The hardness of MSUHP-4B and MSUHP-4C is 1.145 and 1.140 GPa respectively, which exceeds the maximum value from [22].

Hardness is a function of composition and grain size. The effects of composition and grain size can be seen in the data reported in Table 5-2. However, the effects can be made clearer by expanding the data set that is considered. Table 5-3 is an expansion of data reported in Table 5-2 and contains data for ingot and hot pressed LAST (both the $Ag_{0.43}Pb_{18}Sb_{1.2}Te_{20}$ and $Ag_{0.86}Pb_{19}Sb_{1.0}Te_{20}$ composition) and LASTT specimens. The LASTT ingot specimens are from ingot P29 (composition $Ag_{0.5}Pb_6Sb_{0.2}Sn_{2.0}Te_{8.65}$) and ingot P30 (composition $Ag_{0.9}Pb_5Sb_{0.7}Sn_3Te_{9.6}$), while both LASTT hot pressed specimens are from MSUHP-4 (composition $Ag_{0.9}Pb_9Sb_{0.6}Sn_9Te_{20}$).

Figure 5-45 is a plot of the Vickers hardness data from Table 5-3 as a function of composition. From Figure 5-45, the trends with changes in grain size and composition become more obvious. By comparing the hot pressed specimens (which have smaller grain sizes) to the ingot specimens, one can see that reducing the grain size for a given composition can slightly increase the Vickers hardness. The increase is said to be small because the error bars for the ingot and hot pressed specimens overlap. Changing the

composition, however, can lead to more significant changes in Vickers hardness. An example of a larger change in Vickers hardness can be seen by comparing the values for the ingot LAST specimens (composition $Ag_{0.86}Pb_{19}Sb_{1.0}Te_{20}$) and the LASTT ingots. The Vickers hardness of the LAST (composition $Ag_{0.86}Pb_{19}Sb_{1.0}Te_{20}$) and LASTT ingots are different by approximately 0.2 GPa and the error bars between the two sets of specimens do not come close to overlapping.

5.3.2. Thermomechanical Analysis

Thermomechanical analyses were conducted on five specimens: 1)P45C, 2) P45D, 3) ETP20-HP1, 4) HPMSU-18, and 5) HPMSU-20. P45C and P45D were LASTT ingot specimens of composition $Ag_{0.9}Pb_9Sb_{0.6}Sn_9Te_{20}$. ETP20-HP1 and HPMSU-18 were both hot pressed LASTT specimens, but ETP20-HP1 had a composition of $Ag_{0.5}Pb_6Sb_{0.2}Sn_2Te_{20}$, while HPMSU-18 had a composition of $Ag_{0.9}Pb_9Sb_{0.6}Sn_9Te_{20}$. HPMSU-18 was a hot pressed LAST specimen of composition $Ag_{0.86}Pb_{19}Sb_{1.0}Te_{20}$.

All the data from the thermomechanical analyses conducted is being used in an article being written for publication in a journal. The article is titled "Temperature dependent thermal expansion of cast and hot pressed LAST (Pb-Sb-Ag-Te) thermoelectric materials," and the authors are F. Ren, B. D. Hall, E. D. Case, E. J. Timm, R. M. Trejo, R. Meisner, and E. Lara-Curzio. Please refer to this article for the results of the thermomechanical analyses, but note that, at the time of this writing, the paper is still in preparation and has yet to be published.

5.3.3. Room Temperature Thermal Diffusivity

Table 5-4 contains room temperature thermal diffusivity data for selected LAST and LASTT ingot specimens. The thermal diffusivities for the LAST specimens are slightly lower than those for the LASTT specimens, ranging from 0.0145 to 0.0170 cm^2/s, compared to a range of 0.0176 to 0.0190 cm^2/s for the LASTT specimens. These values compare well with the value of 0.0162 cm^2/s reported for another LAST ingot [91].

Thermal diffusivity, α, can be calculated as [100]

$$\alpha = \frac{\kappa}{C_p \rho} \tag{5.1}$$

where is the thermal diffusivity, C_p is the heat capacity when pressure is constant, and ρ is the density. This means that a specimen's thermal conductivity can be calculated from thermal diffusivity data, if the heat capacity and density are known. Thermal conductivity can be calculated as [100]

$$\kappa = \alpha C_p \rho \tag{5.2}$$

5.3.4. Biaxial Flexure Testing

Table 5-5 biaxial flexure strength for selected hot pressed LAST specimens. These biaxial flexure strength results are reported in a paper accepted for publication in an MRS proceedings, but additional results on grain size are reported in this thesis.

Strength data are available for specimens HPMSU-14 and HPMSU-16, and their respective values are 52.9 and 50.3 MPa. No strength value is available for HPMSU-13 because the specimen broke while it was being polished. These values represent a factor

Table 5-2—Vickers hardness of selected specimens. Indentations were made using a load of 0.3 kg at a loading speed of 70 μm/s for a loading time of 10 s. The Vickers hardness for all the LAST specimens fit within the range of values reported for LAST ingots in [22]. The Vickers hardness data for the LASTT hot pressed specimens, HPMSU-4B and HPMSU-4C, was greater than the any value reported in [22].

Specimen	Composition	Vickers Hardness (GPa)
HPMSU-1E	$Ag_{0.43}Pb_{18}Sb_{1.2}Te_{20}$	0.783 ± 0.043
HPMSU-1F	$Ag_{0.43}Pb_{18}Sb_{1.2}Te_{20}$	0.818 ± 0.035
HPMSU-3-1	$Ag_{0.43}Pb_{18}Sb_{1.2}Te_{20}$	0.872 ± 0.035
HPMSU-3-2	$Ag_{0.43}Pb_{18}Sb_{1.2}Te_{20}$	0.879 ± 0.035
HPMSU-4B	$Ag_{0.9}Pb_9Sb_{0.6}Sn_9Te_{20}$	1.145 ± 0.055
HPMSU-4C	$Ag_{0.9}Pb_9Sb_{0.6}Sn_9Te_{20}$	1.140 ± 0.048
JPL HP	$Ag_{0.43}Pb_{18}Sb_{1.2}Te_{20}$	0.701 ± 0.040
N155 B6	$Ag_{0.86}Pb_{19}Sb_{1.0}Te_{20}$	0.630 ± 0.019
N156 D2	$Ag_{0.86}Pb_{19}Sb_{1.0}Te_{20}$	0.570 ± 0.023

Table 5-3—Expanded set of Vickers hardness data for ingot and hot pressed LAST and LASTT materials, including the data from Table 5-2. Notice that there data for both ingot and hot pressed specimens of the composition $Ag_{0.43}Pb_{18}Sb_{1.2}Te_{20}$ and $Ag_{0.86}Pb_{19}Sb_{1.0}Te_{20}$. The LASTT ingot data are for two specimens having two different compositions, while the hot pressed data are for specimens of the $Ag_{0.9}Pb_9Sb_{0.6}Sn_9Te_{20}$ composition. The data not contained Table 5-2 comes from Jennifer Ni, Fei Ren, and [22].

	Specimen	Composition	Vickers Hardness (GPa)
Ingot, $Ag_{0.43}$	N42	$Ag_{0.43}Pb_{18}Sb_{1.2}Te_{20}$	0.855 ± 0.186
	N43	$Ag_{0.43}Pb_{18}Sb_{1.2}Te_{20}$	0.641 ± 0.071
HP, $Ag_{0.43}$	JPL HP	$Ag_{0.43}Pb_{18}Sb_{1.2}Te_{20}$	0.701 ± 0.040
	HPMSU-1E	$Ag_{0.43}Pb_{18}Sb_{1.2}Te_{20}$	0.783 ± 0.043
	HPMSU-1F	$Ag_{0.43}Pb_{18}Sb_{1.2}Te_{20}$	0.818 ± 0.035
	HPMSU-3-1	$Ag_{0.43}Pb_{18}Sb_{1.2}Te_{20}$	0.872 ± 0.035
	HPMSU-3-2	$Ag_{0.43}Pb_{18}Sb_{1.2}Te_{20}$	0.879 ± 0.035
Ingot, $Ag_{0.86}$	N155 B6	$Ag_{0.86}Pb_{19}Sb_{1.0}Te_{20}$	0.630 ± 0.019
	N156 D2	$Ag_{0.86}Pb_{19}Sb_{1.0}Te_{20}$	0.570 ± 0.023
HP, $Ag_{0.86}$	MSUHP-8	$Ag_{0.86}Pb_{19}Sb_{1.0}Te_{20}$	0.792 ± 0.046
	MSUHP-11	$Ag_{0.86}Pb_{19}Sb_{1.0}Te_{20}$	0.898 ± 0.062
	MSUHP-12	$Ag_{0.86}Pb_{19}Sb_{1.0}Te_{20}$	0.964 ± 0.062
Ingot (LASTT)	P29-C3	$Ag_{0.5}Pb_6Sb_{0.2}Sn_{2.0}Te_{8.65}$	0.917 ± 0.048
	P30-C3	$Ag_{0.9}Pb_5Sb_{0.7}Sn_3Te_{9.6}$	1.058 ± 0.065
HP, $Ag_{0.9}$	HPMSU-4B	$Ag_{0.9}Pb_9Sb_{0.6}Sn_9Te_{20}$	1.145 ± 0.055
	HPMSU-4C	$Ag_{0.9}Pb_9Sb_{0.6}Sn_9Te_{20}$	1.140 ± 0.048

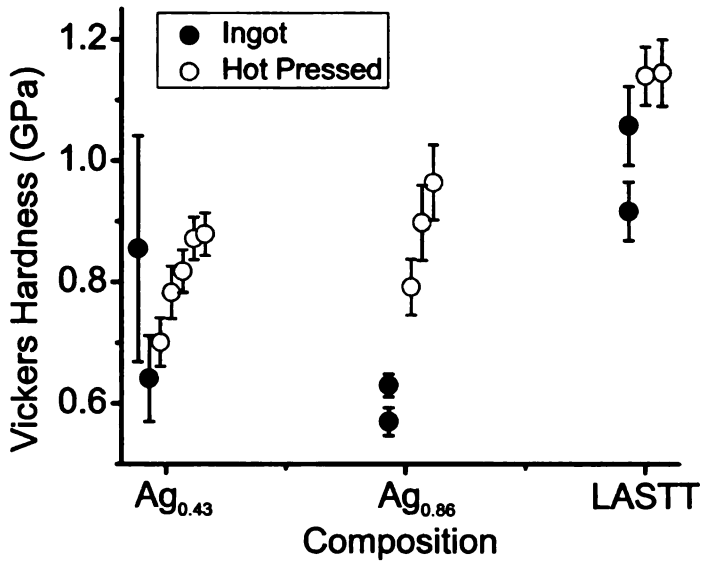

Figure 45—Vickers hardness as a function of composition for the ingot and hot pressed specimens listed in Table 5-3. Notice that the reduction in grain size between the ingot and hot pressed specimens leads to a small increase in Vickers hardness, while the changes in composition result in larger changes in Vickers hardness.

Table 5-4—Room temperature thermal diffusivities for selected LAST and LASTT specimens. The room temperature thermal diffusivity data for the LAST and LASTT specimens compares well with the value of 0.0162 cm^2/s reported for another LAST ingot [91]. Also, the thermal diffusivities for the LAST specimens are slightly lower than those for the LASTT specimens.

Specimen	Composition	Density (g/cm^3)	α_{avg} (cm^2/s)
N177B	$Ag_{0.86}Pb_{19}Sb_{1.0}Te_{20}$	7.95	0.0170
N177D	$Ag_{0.86}Pb_{19}Sb_{1.0}Te_{20}$	7.92	0.0164
N177A	$Ag_{0.86}Pb_{19}Sb_{1.0}Te_{20}$	7.95	0.0149
N177C*	$Ag_{0.86}Pb_{19}Sb_{1.0}Te_{20}$	8.06	0.0145
P45D	$Ag_{0.9}Pb_9Sb_{0.6}Sn_9Te_{20}$	7.34	0.0190
P45A	$Ag_{0.9}Pb_9Sb_{0.6}Sn_9Te_{20}$	7.19	0.0183
P45C	$Ag_{0.9}Pb_9Sb_{0.6}Sn_9Te_{20}$	7.37	0.0180
P45D	$Ag_{0.9}Pb_9Sb_{0.6}Sn_9Te_{20}$	7.34	0.0176

of more than three increase over the fracture strength reported for LASTT ingots, which was 15.3 MPa [21]. This increase was likely achieved by reducing the grain size of the bulk specimens via powder processing.

However, the strength values for the hot pressed specimens were not quite as high as anticipated. To check, the small powder specimens from remnants of the powder batches from which the billets were produced were observed in the SEM. In the SEM, powder particles on the order of 50 microns and larger were observed. The observation that powder particle sizes were larger than those reported earlier by Pilchak et al. [42] was the motivation for much of the work reported in this thesis.

The grain sizes of HPMSU-14 and HPMSU-16 were calculated using the linear intercept method. For each specimen, one micrograph was used and more than 250 intercepts were counted. The grain size for HPMSU-14 was approximately 7 microns and the grain size for HPMSU-16 was approximately 8 microns. However, the grain size distributions for these specimens are atypical. Figure 5-46 is an SEM micrograph of HPMSU-16 after fracture and after undergoing a thermal anneal to reveal the grains, and is characteristic of both specimens. The material has a bimodal grain size distribution, which is composed of a matrix of grains less than 10 microns across, and a second "phase" of larger grains having dimensions on the order of tens of microns.

The largest grains are approximately 60 microns across on their major axis. This means that the grain size for the largest grains has been reduced by a factor of approximately 10, as compared to ingot material [21]. This factor of ten decrease in the grain size means that the three-fold increase in strength observed in HPMSU-14 and HPMSU-16 is not unreasonable.

Table 5-5—Biaxial flexure strength for selected hot pressed HPMSU specimens. All specimens were 22 mm in diameter. No data is reported for HPMSU-13 because the specimen broke during polishing. The biaxial flexure strength for a LASTT ingot was 15.3 MPa, meaning HPMSU-14 and HPMSU-16 have a fracture strength that is more than a factor of three increase.

Specimen	Composition	Density (g/ cm^3)	Biaxial Flexure Strength (MPa)
HPMSU-13	$Ag_{0.86}Pb_{19}Sb_{1.0}Te_{20}$	8.01	
HPMSU-14	$Ag_{0.86}Pb_{19}Sb_{1.0}Te_{20}$	7.64	52.9
HPMSU-16	$Ag_{0.86}Pb_{19}Sb_{1.0}Te_{20}$	7.65	50.3

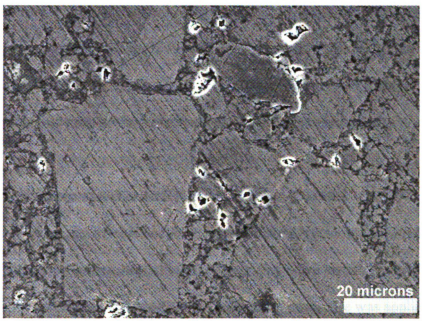

Figure 5-46—SEM micrograph of thermally annealed surface from HPMSU-16 (composition $Ag_{0.86}Pb_{19}Sb_{1.0}Te_{20}$) for grain size calculation. Using a total of 270 intercepts, the grain size from this micrograph was calculated to be approximately 8 microns. Notice grain size population: there are a few grains with dimensions on the order of tens of microns, and there are numerous smaller grains (with sizes less than ten microns) surrounding these larger grains. As such, the validity of the grain size calculated from this micrograph is questionable. This micrograph is characteristic of HPMSU-14 as well.

It is important to note that more recent hot pressed specimens have a different microstructure than that shown in Figure 5-46. (No fracture strength data is available for more recent hot pressed specimens because all recent hot pressed billets have been used for TEG module development and testing.) Figure 5-47 is an SEM micrograph of a fracture surface from MSUHP-36 (composition $Ag_{0.86}Pb_{19}Sb_{1.0}Te_{20}$) grain size annealed at 500 °C for 2 hrs. The powder used to make HPMSU-36 was milled using a process similar to that for the wet milled N182 batch 10 (Section 4.3.2.7.8.2.), except that the powder was dry milled for only one 3 hr segment. From visual inspection of Figure 5-47, the grain size of MSUHP-36 can be estimated to be approximately 5 microns. Also, the grain size distribution does not have two noticeably different modes.

5.3.5. Brunauer-Emmett-Teller (BET) Surface Area Analysis

Table 5-6 contains the BET specific surface areas for a variety of LAST powders, all of which have composition $Ag_{0.43}Pb_{18}Sb_{1.2}Te_{20}$. The powders can be divided into three groups: 1) powders to which a CGM-t dry milling procedure was applied (CGM-t meaning that the powder was crushed, ground, and then milled for a time t) [42], 2) powders to which a CGSRM-t dry milling procedure was applied (CGSRM-t meaning that the powder was crushed, ground, sieved, reground until all of it passed through a 53 micron sieve, and then milled for a time t) [42], and 3) powders to which a wet milling procedure was applied (CGSRM-180 first, then wet milled for a length of time with some amount of hexane) [43]. The CGM-t powder specimens are samples G, H, and F. The CGSRM-t powder specimens are samples E and A. The wet milled powder specimens are the remaining samples presented in Table 5-6.

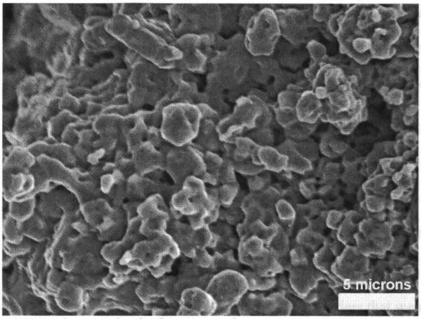

Figure 5-47—SEM micrograph of a fracture surface on MSUHP-36 (composition $Ag_{0.86}Pb_{19}Sb_{1.0}Te_{20}$) after a grain size anneal (2 hrs at 500 °C). From visual inspection, the grain size can be estimated to be approximately 5 microns.

The specific surface areas of the different powder specimens make sense; with increased powder processing time, the powders became finer, so the specific surface areas increased. The CGM-t powders had specific surface areas that ranged from 0.047 to 0.32 m^2/g. For the CGSRM-t powders, the specific surface areas were 0.21 m^2/g for Sample E (t = 30 min) and 0.55 m^2/g for Sample A (t = 180 min). The wet milled powders had specific surface areas that ranged between 1.43 and 2.71 m^2/g.

Figure 5-48 is a plot of specific surface area as a function of wet milling time. Figure 5-49 is a plot of equivalent spherical particle diameter, calculated from the specific surface area, as a function of wet milling time. The powders that were milled with 0 cc hexane were milled according to the same procedure as those that were wet milled, but no hexane was added to the milling jar prior to milling, so the powder milled with 0 cc hexane was actually dry milled.

Like the data in Table 5-6, Figures 5-48 and 5-49 also demonstrate that with increasing powder processing time, a powder becomes finer. In both figures, as milling time increases, the data approaches two asymptotes; one asymptote is for the dry milled powders and the other asymptote is for the wet milled powders. These asymptotes represent the grindability limits of the powder for wet and dry milling. The grindability limit for a dry milled powder is higher (larger diameter particles, smaller specific surface area) than that for a wet milled powder. However, the grindability limit for a dry milled powder is reached faster than that for a wet milled powder. In Figure 5-48, the dry milled powder looks to reach its grindability limit of approximately 1.45 m^2/g after 8 hours of

Table 5-6—Brunauer-Emmett-Teller (BET) specific surface areas, and calculated equivalent spherical particle diameters, of selected LAST powders. The powders underwent various premilling treatments, and some powders were dry milled, while others were both dry and wet milled. All specimens were degassed for 6 hrs at 200 °C. The specific surface area data ranges between 0.0472 and 2.71 m^2/g.

Sample	Ingot No.	Processing History	Adsorption Gas	Size from Coulter Counter (μm)	Specific Surface Area from MAS (m^2/g)	Equivalent Particle Diameter (μm)
G	N59	CGM-30	Kr	66 ± 38	0.0472	15.69
H	N112	CGM-75	Kr	14 ± 8	0.0922	8.034
E	N104	CGSRM-30	Kr	7.2 ± 3.6	0.2091	3.542
F	N102	CGM-420	Kr	7.4 ± 3.9	0.3189	2.323
A	N130	CGSRM-180	N_2	6.4 ± 3.3	0.5510	1.344
C	N124	CGSRM-180, WM 24 hr 5 cc hexane	N_2	4.4 ± 2.3	1.9140	0.386
D	N129	CGSRM-180, WM 24 hr 25 cc hexane	N_2	TBD	2.3061	0.321
B	N129	CGRSM-180, WM 24 hr 50 cc hexane	N_2	TBD	2.7107	0.273
H0-T480	N129	CGSRM-180, WM 8 hr 0 cc hexane	N_2	TBD	1.4634	0.506
H0-T960	N129	CGSRM-180, WM 16 hr 0 cc hexane	N_2	TBD	1.4459	0.512
H0-T1440	N129	CGSRM-180, WM 24 hr 0 cc hexane	N_2	TBD	1.5244	0.486
H10-T480	N129	CGSRM-180, 8 hr 10 cc hexane	N_2	TBD	1.4330	0.517
H10-T960	N129	CGSRM-180, WM 16 hr 10 cc hexane	N_2	TBD	1.9694	0.376

Table 5-6 (cont'd)

Sample	Ingot No.	Processing History	Adsorption Gas	Size from Coulter Counter (μm)	Specific Surface Area from MAS (m^2/g)	Equivalent Particle Diameter (μm)
H10-T1440	N129	CGSRM-180, WM 24 hr 10 cc hexane	N_2	TBD	2.6686	0.278
H25-T480	N129	CGSRM-180, WM 8 hr 25 cc hexane	N_2	TBD	1.6134	0.459
H25-T960	N129	CGSRM-180, WM 16 hr 25 cc hexane	N_2	TBD	1.9859	0.373
H30-T480	N130	CGSRM-180, WM 8 hr 30 cc hexane	N_2	TBD	1.7491	0.424
H30-T960	N130	CGSRM-180, WM 16 hr 30 cc hexane	N_2	TBD	2.1642	0.342
H30-T1440	N130	CGSRM-180, WM 24 hr 30 cc hexane	N_2	TBD	2.6386	0.281
H50-T480	N129	CGSRM-180, WM 8 hr 50 cc hexane	N_2	TBD	1.6819	0.440
H50-T960	N129	CGSRM-180, WM 16 hr 50 cc hexane	N_2	TBD	2.1360	0.347

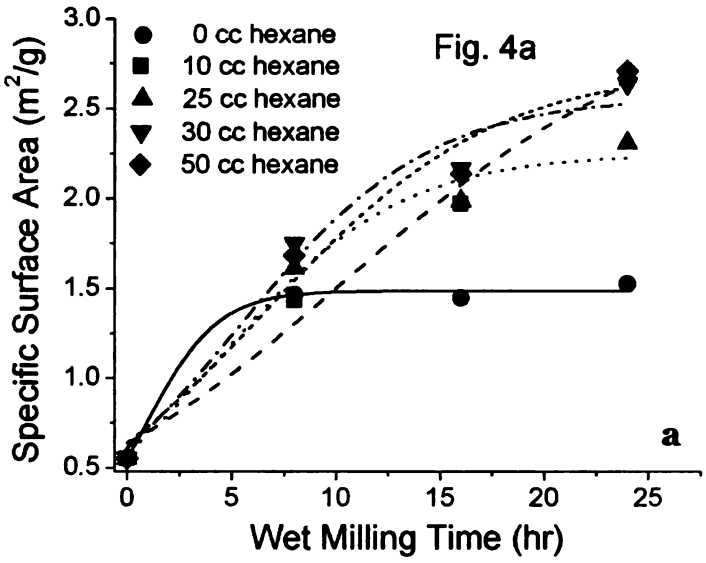

Figure 5-48—Plot of specific surface area versus wet milling time. The grindability limit for the 0 cc hexane (dry milled) powders was reached after approximately 8 hrs, while the wet milled powders appeared to reach their grindability limit after 24 hrs. The dry milling grindability limit is approximately 1.45 m^2/g, while the wet milling grindability limit is approximately 2.5 m^2/g.

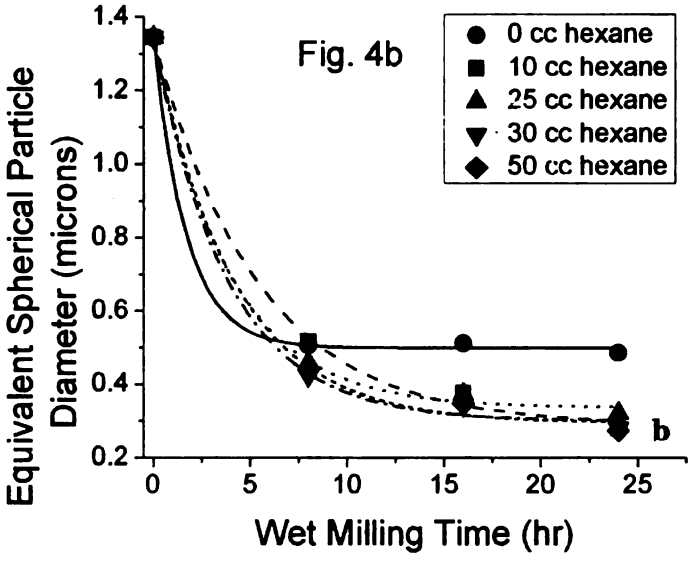

Figure 5-49—Plot of equivalent spherical particle diameter versus wet milling time. The grindability limit for the 0 cc hexane powders was reached after approximately 8 hrs, while the wet milled powders appeared to reach their grindability limit after 24 hrs. The dry milling grindability limit is approximately 0.5 microns, while the wet milling grindability limit is approximately 0.3 microns.

milling. Conversely, the wet milled powder looks to just reach its grindability limit of approximately 2.5 m^2/g after 24 hours of milling. From Figures 5-48 and 5-49, it is also apparent that the final powder particle size is unaffected by the exact amount of hexane added for wet milling. However, as noted in [43], the nature of the agglomerates that form in the powder during wet milling is affected by the amount of hexane added—with hexane additions greater than or equal to 25 cc, the agglomerates formed are soft rather than hard.

5.3.6. Inductively Coupled Plasma Spectroscopy

5.3.6.1. Inductively Coupled Plasma Mass Spectroscopy (ICP-MS) at Shiva

Monitoring contamination of the produced powders is an important concern and this can be achieved via ICP-MS. Table 5-8 presents ICP-MS data for selected powder specimens, and Table 5-7 gives the processing details of the powder specimens present in Table 5-8. All of the measurements presented in Table 5-8 were made by Shiva Technologies (subdivision of Evans Analytical Group, Syracuse, NY). Some of the data in Table 5-8 was previously presented in [42].

The impurities monitored were B, Na, Al, Si, P, K, Ca, Fe, and Sn. Except for specimen 1, the impurity concentrations measured were typically less than 35 ppm. These relatively low impurity concentrations were observed in specimens that were milled for total times of 3 hours (specimens 2 and 5) and specimens that were milled for total times of 27 hours (specimens 3 and 4). Since powders milled for times totaling 27 hours did not contain high concentrations of impurities, it was concluded that milling did not introduce unacceptably high levels of contamination into the powders. Specimen 1,

Table 5-7—ICP-MS and ICP-OES specimen labels and compositions included in this study. All milling was done in a milling jar lined with 99.7% pure alumina. The impurities in the alumina liner of the milling jar were SiO_2 (0.075%), Fe_2O_3 (0.010%), CaO (0.070%), MgO (0.075%), and Na_2O (0.010%). All dry milling was done at 100 rpm with ten 99.64% pure 20 mm diameter alumina spheres. All wet milling was done at 150 rpm with 150 cc of 99.64% pure 3 mm diameter alumina spheres. The impurities in the 20 mm diameter alumina spheres and the 3 mm diameter alumina spheres were SiO_2 (0.100%), Fe_2O_3 (0.020%), CaO (0.040%), MgO (0.150%), Na_2O (0.040%), and K_2O (0.010%).

	Label	Milling	Composition
1	N120-CGSRM-180	Dry: 3 hr	$Ag_{0.43}Pb_{18}Sb_{1.2}Te_{20}$
2	EAG-H0-T1440	Dry: 3 hr	$Ag_{0.43}Pb_{18}Sb_{1.2}Te_{20}$
3	EAG-H10-T1440	Dry: 3 hr, Wet: 24 hr	$Ag_{0.43}Pb_{18}Sb_{1.2}Te_{20}$
4	EAG-H30-T1440	Dry: 3 hr, Wet: 24 hr	$Ag_{0.43}Pb_{18}Sb_{1.2}Te_{20}$
5	EAG-N175-B1	Dry: 3 hr	$Ag_{0.86}Pb_{19}Sb_{1.0}Te_{20}$

Table 5-8—ICP-MS results for selected LAST powders. Specimens were tested by Shiva Technologies. For specimens 2-5, most impurities have a concentration of 35 ppm or less. Specimen 1, however, has higher concentrations of B, Na, Sn, and K, as well as an extremely high concentration of Si (1.1 wt%). This high concentration of Si may be from a glass bead, used to clean the milling jar, getting into the powder.

	Concentration (ppm by weight)				
Element	**1**	**2**	**3**	**4**	**5**
Si	1.1×10^4	<25	<10	<10	<10
B	92	<0.1	1.4	<0.1	<0.1
Na	55	<0.1	22	26	22
Sn	44	2.2	9.5	220	17
Al	35	7.3	7.2	0.8	2.1
P	16	<10	<10	<10	<10
Ca	5.6	35	32	20	37
Fe	15	<10	1.9	14	26
K	55	--	<10	<10	<10

the first specimen on which an ICP-MS analysis was conducted, however, was anomalous from the other specimens. Specimen 1 had higher impurity concentrations for B (92 ppm), Na (55 ppm), Sn (44 ppm), K (55 ppm), and especially Si (1.1×10^4 ppm). Based on the fact that Si was present in an extremely high concentration (more than 1 wt%) and the other impurities with dissimilarly high concentrations can be found in glass, the uniqueness of this specimen was attributed to a glass bead from the milling jar cleaning (Section 4.4.1.) getting into the powder.

5.3.6.2. Inductively Coupled Plasma Optical Emission Spectroscopy (ICP-OES) at Michigan State University

Table 5-9 presents impurity concentrations measured by ICP-OES in selected samples that mirror some of those tested by Shiva Technologies. The ICP-OES measurements were made at Michigan State University by Kirk Stuart. Analyses were performed on specimens from the same powder batches as those previously tested by Shiva Technologies to investigate how well the results compared.

In looking at Tables 5-9 and 5-8, the results compare relatively well. In Table 5-9, only data for the elements B, Na, Al, Si, P, K, Ca, and Fe are presented because the equipment available at Michigan State University has difficulty getting Sn into solution. The values reported in Table 5-9 are all around 35 ppm or less, which agrees with the data presented in Table 5-8. However, Na concentrations for all three specimens presented in Table 5-9 are high, with the values for specimens 3 and 4 exceeding the values in Table 5-8. No explanation is currently available for this disagreement in among specimens in terms of the ICP-measured Na concentration. Even so, the ICP facilities at

Michigan State University match Shiva Technologies' facilities well enough for the purposes of this work.

Table 5-9—ICP-OES results for selected LAST powders. Specimens were tested by Kirk Stuart at Michigan State University. Sn was omitted from these scans as it is difficult to get into solution. The results from MSU and Shiva Technologies generally are comparable, but the Na concentration in all three specimens is high.

	Concentration (ppm)		
Element	1 (N120)	3 (H10)	4 (H30)
Si	<25	<25	<25
B	<25	<25	<25
Na	46.7	105	81.4
Sn	*	*	*
Al	<25	<25	<25
P	<25	<25	<25
Ca	<25	<25	<25
Fe	1.56	2.35	8.99
K	<50	<50	<50

6. Summary and Conclusions

Much of the work reported in this thesis is focused on powder processing experiments. The goal of these experiments was to produce fine grained powders from which fine grained bulk specimens could be fabricated. By reducing the grain size of the material, mechanical properties such as the material's strength could be improved.

The first experiments were concerned with scaling-up the powder batch size. The powder batch size was effectively increased to 50 g by milling CGSR feedstock for 3 hr at 100 rpm with fourteen alumina spheres 20 mm in diameter, and then milling the powder for an additional 3 hr at 150 rpm with 280 g of 3 mm diameter alumina media. The powder produced in this 50 g batch had a mean of 5.15 microns and a median of 4.53 microns. Further scaling-up of the powder batch size to 70 g was achieved by milling CGSR feedstock for 3 hr at 150 rpm with 280 g of 3 mm diameter alumina media. The powder produced in this 70 g batch had a mean of 5.11 microns and a median of 4.45 microns.

After the success of the scale-up experiments, it was discovered that the previously developed milling procedures, including the just developed scaled-up procedures, did not reduce the powder particle size. Initial efforts to solve this problem were centered on cleaning the alumina milling jar and alumina media (both the 20 mm and the 3 mm diameter media). Cleaning experiments included the use of alumina powder as an abrasive, which was ineffective, and cleaning the media in aqua regia, which did remove LAST/LASTT accumulated on the media.

Following the work to find an effective cleaning procedure, the next experiments were concerned with developing a new milling procedure that would reduce the powder

particle size. These new procedures included mixtures of the 20 mm diameter and 3 mm diameter alumina media, combining dry and wet milling (in hexane), and varying the milling speed and milling time. The feedstock for these experiments was CGSR powder that had a mean of 20.1 microns and a median of 12.4 microns.

The milling procedure that was found to be the most effective began by dry milling the powder for 3 hr at 100 rpm with, nominally, 140 g of the 20 mm diameter alumina media and 60 g of the 3 mm diameter alumina media, in Ar. After dry milling, the powder caked to the sides of the milling jar was scraped loose, 25 cc of hexane was added to the milling jar, and the powder was milled for 6 hr at 100 rpm in Ar using the same media as in the previous dry milling step. This milling procedure produced powders with a mean diameter of 3.4 microns, a median diameter of 2.3 microns.

Next, two new attempts were made to scale-up the powder size. The first experiment tried to increase the powder batch size to 50 g, while the second experiment tried to increase the powder batch size to 35 g. Both experiments were ineffective at decreasing the powder particle size.

Concurrent to the powder processing experiments, tests to measure the properties of bulk specimens and characterize powders were conducted. Bulk specimens were tested by Vickers indentation to measure hardness, a flash method to measure room temperature thermal diffusivity, and biaxial flexure to measure strength. Powders were characterized by BET analysis to determine their specific surface area and ICP spectroscopy to measure the concentration of impurities in the powders from their processing.

The Vickers hardness for LAST ingot and hot pressed specimens were between 0.57 and 0.88 GPa, while values for LAST ingots from [22] ranged from 0.53 to 0.92 GPa. The Vickers hardness for LASTT hot pressed specimens, 1.14 and 1.15 GPa, exceeded any previously reported values. The room temperature thermal diffusivities for LAST (0.0170-0.0145 cm^2/s) and LASTT (0.0190-0.0176 cm^2/s) ingot specimens compared well to the value reported for another LAST ingot in [91] (0.0162 cm^2/s). The biaxial flexure strengths of two hot pressed LAST specimens were 52.9 and 50.3 MPa, while the biaxial flexure strength for LASTT ingots was 15.3 MPa [21]. BET specific surface areas for powders ranged from 0.0472 m^2/g for CGM-*t* powder to 2.71 m^2/g for wet milled for 24 hr in 50 cc hexane after being dry milled according to the previously developed dry milling procedure [42]. ICP spectroscopy was conducted by both Shiva Technologies (Syracuse, NY) and Kirk Stuart from Michigan State University (East Lansing, MI). Both labs found that impurity (Si, B, Na, Sn, Al, P, Ca, Fe, and K) concentrations were typically less than 35 ppm.

In this work, much was learned about powder processing LAST and its agglomeration. Large powder particles—powder particles with dimensions on the order of 50 microns—typically resulted when only dry milling was utilized. By combining dry milling with wet milling, powders containing no particles greater than 20 microns in diameter were produced. Both dry and wet milled powders contained agglomerates. However, the wet milled powders contained agglomerates that appeared softer in nature and were smaller than the agglomerates formed in dry milled powder, making the soft agglomerates less detrimental to the sintered component.

References

[1] D. M. Rowe in: D. M. Rowe (Ed.), CRC Handbook of Thermoelectrics, CRC Press, LLC, Boca Raton, 1995, pp. 1-5.

[2] G. Mahan, B. Sales, and J. Sharp, "Thermoelectric Materials: New Approaches to an Old Problem," Physics Today, 50 (1997), pp. 42-47

[3] D. D. Pollock in: D. M. Rowe (Ed.), CRC Handbook of Thermoelectrics, CRC Press, LLC, Boca Raton, 1995, pp. 7-17.

[4] G. S. Nolas, J. Sharp, and H. J. Goldsmid, Thermoelectrics: Basic Principles and New Materials Developments, Springer-Verlag, Berlin, 2001.

[5] B. C. Sales, "Critical overview of recent approaches to improved thermoelectric materials," International Journal of Applied Ceramic Technology, 4 (2007), pp. 291-296.

[6] C. Kittel, Introduction to Solid State Physics, John Wiley & Sons, Inc., 2005, p. 156.

[7] H. Scherrer, S. Scherrer in: D. M. Rowe (Ed.), CRC Handbook of Thermoelectrics, CRC Press, LLC, Boca Raton, 1995, pp. 211-237.

[8] E. A. Skrabek and D. S. Trimmer in: D. M. Rowe (Ed.), CRC Handbook of Thermoelectrics, CRC Press, LLC, Boca Raton, 1995, pp. 267-275.

[9] C. B. Vining in: D. M. Rowe (Ed.), CRC Handbook of Thermoelectrics, CRC Press, LLC, Boca Raton, 1995, pp. 329-337.

[10] K. F. Hsu, S. Loo, F. Guo, W. Chen, J. S. Dyck, C. Uher, T. P. Hogan, E. K. Polychroniadis, M. G. Kanatzidis, "Cubic $AgPb_mSbTe_{2+m}$: Bulk thermoelectric materials with high figure of merit," Science, 303 (2004), pp. 818-821.

[11] L. D. Hicks, and M. S. Dresselhaus, "Effect of quantum-well structures on the thermoelectric figure of merit," Physical Review B, 47 (1993), pp. 12727-12731.

[12] L. D. Hicks, and M. S. Dresselhaus, "Thermoelectric figure of merit for a one-dimensional conductor," Physical Review B, 47 (1993), pp. 16631-16634.

[13] L. D. Hicks, T. C. Harman, X. Sun, M. S. Dresselhaus, "Experimental study of the effect of quantum-well structures on the thermoelectric figure of merit," Physical Review B, 53 (1996), pp. 10493-10496.

[14] T. C. Harman, P. J. Taylor, M. P. Walsh, and B. E. LaForge, "Quantum dot superlattice thermoelectric materials and devices," Science, 297 (2002), pp. 2229-2232.

[15] R. Venkatasubramanian, E. Siivola, T. Colpitts, and B. O'Quinn, "Thin-film thermoelectric devices with high room-temperature figures of merit," Nature, 413 (2001), pp. 597-602.

[16] Y. Q. Cao, X. B. Zhao, T. J. Zhu, X. B. Zhang, J. P. Tu, "Syntheses and thermoelectric properties of Bi_2Te_3/Sb_2Te_3 bulk nanocomposites with laminated nanostructure," Applied Physics Letters, 92 (2008), Article number: 143106

[17] T. P. Hogan, A. Downey, J. Short, J. D'Angelo, C. I. Wu, E. Quarez, J. Androulakis, P. F. P. Poudeu, J. R. Sootsman, D. Y. Chung, M. G. Kanatzidis, S. D. Mahanti, E. J. Timm, H. Schock, F. Ren, J. Johnson, E. D. Case, "Nanostructured thermoelectric materials and high-efficiency power-generation modules," Journal of Electronic Materials, 36 (2007), pp. 704-710.

[18] H. Rodot, "Etude et proprietes du systeme $AgSbTe_2$-PbTe," Comptes Rendus Hebdomadaieres des Séances de L'Academie des Sciences, 249 (1959), pp. 1872-1874

[19] L. Borisova, "Density-of-States effective mass in solid-solutions of the $(Ag_{x/2}Pb_{1-x}Sb_{x/2})Te$ type," Physica Status Solidi B—Basic Research, 126 (1984), pp. K155-K158

[20] E. Quarez, K. F. Hsu, R. Pcionek, N. Frangis, E. K. Polychroniadis, M. G. Kanatzidis, "Nanostructuring, compositional fluctuations, and atomic ordering in the thermoelectric materials $AgPb_mSbTe_{2+m}$. The myth of solid solutions," Journal of the American Chemical Society, 127 (25), 9177-9190

[21] F. Ren, E. D. Case, E. J. Timm, M. D. Jacobs, H. J. Schock, "Weibull analysis of the biaxial fracture strength of a cast p-type LAST-T thermoelectric material," Philosophical Magazine Letters, 86 (2006), pp. 673-682

[22] F. Ren, E. D. Case, E. J. Timm, H. J. Schock, "Hardness as a function of composition for n-type LAST thermoelectric material," Journal of Alloys and Compounds, 455 (2008), pp. 340-345

[23] F. Ren, E. D. Case, E. J. Timm, H. J. Schock, "Young's modulus as a function of composition for an n-type lead-antimony-silver-telluride (LAST) thermoelectric material," Philosophical Magazine, 87 (2007), pp. 4907-4934

[24] W. D. Kingery, H. K. Bowen, D. R. Uhlmann, Introduction to Ceramics, John Wiley & Sons, New York, 1976, p. 791

[25] M. S. Darrow, W. B. White, R. Roy, "Micro-Indentation Hardness Variation as a Function of Composition for Polycrystalline Solutions in the Systems PbS/PbTe, PbSe/PbTe, and PbS/PbSe", *Journal of Materials Science,* vol. 4, pg 313-319, April 1969

[26] E. I. Rogacheva, O. N. Nashchekina, "Impurity Effects on Microhardness of PbTe," Inorganic Materials, vol. 32 (11), pg. 1172-1174, 1996

[27] K. Ueno, A. Yamamoto, T. Noguchi, T. Inoue, S. Sodeoka, H. Obara, "Optimization of hot-press conditions of Zn_4Sb_3 for high thermoelectric performance. II. Mechanical properties," Journal of Alloys and Compounds, 388 (2005), pp. 118-121

[28] K. Ueno, A. Yamamoto, T. Noguchi, T. Inoue, S. Sodeoka, H. Obara, "Optimization of hot-press conditions of Zn_4Sb_3 for high thermoelectric performance. III. Effect of starting particle size on thermoelectric and mechanical properties," Journal of Alloys and Compounds, 392 (2005), pp. 195-199

[29] A. Kosuga, M. Uno, K. Kurosaki, S. Yamanaka, "Thermoelectric properties of $Ag_{1-x}Pb_{18}SbTe_{20}$ (x = 0, 0.1, 0.3)," Journal of Alloys and Compounds, 387 (2005), pp. 52-55

[30] S.C. Ur, P. Nash, R Schwarz, "Mechanical and thermoelectric properties of Zn_4Sb_3 and Zn_4Sb_3+Zn directly synthesized using elemental powders," Metals and Materials International, 11 (2005), pp. 435-441

[31] X. A. Fan, J. Y. Yang, W. Zhu, S. Q. Bao, X. K. Duan, C. J. Xiao, Q. Q. Zhang, Z. Xie, "Effect of nominal Sb_2Te_3 content on thermoelectric properties of p-type $(Bi_2Te_3)_x(Sb_2Te_3)_{1-x}$ alloys by MA-HP," Journal of Physics D: Applied Physics, 39 (2006), pp. 5069-5073

[32] J. Jiang, L. Chen, S. Bai, Q. Yao, Q. Wang, "Fabrication and thermoelectric performance of textured n-type $Bi_2(Te, Se)_3$ by spark plasma sintering," Materials Science and Engineering B, 117 (2005), pp. 334-338

[33] J. Y. Peng, J. Y. Yang, T. J. Zhang, X. L. Song, Y. H. Chen, "Preparation and characterization of Fe substituted $CoSb_3$ skutterudite by mechanical alloying and annealing," Journal of Alloys and Compounds, 381 (2004), pp. 313-316

[34] B. L. Yu, X. F. Tang, Q. Qi, Q. J. Zhang, "Preparation and termal transport properties of $CoSb_3$ nano-compounds," Acta Physica Sinica, 53 (2004), pp. 3130-3135

[35] J. Y. Yang, Y. H. Chen, J. Y. Peng, X. L. Song, W. Zhu, J. F. Su, R. G. Chen, "Synthesis of $CoSb_3$ skutterudite by mechanical alloying," Journal of Alloys and Compounds, 375 (2004), pp. 229-232

[36] N. Bouad, R. M. Marin-Ayral, G. Nabias, J. C. Tedenac, "Phase transformation study of Pb-Te powders during mechanical alloying," Journal of Alloys and Compounds, 353 (2003), pp. 184-188

[37] P. J. Taylor, J. R. Maddux, W. A. Jesser, F. D. Rosi, "Room-temperature anisotropic, thermoelectric, and electrical properties of n-type $(Bi_2Te_3)_{90}(Sb_2Te_3)_5(Sb_2Se_3)_5$ and compensated p-type $(Sb_2Te_3)_{72}(Bi_2Te_3)_{25}(Sb_2Se_3)_3$ semiconductor alloys," Journal of Applied Physics, 85 (1999), pp. 7807-7813

[38] S. S. Kim, S. Yamamoto, T Aizawa, "Thermoelectric properties of anisotropy-controlled p-type Bi-Te-Sb system via bulk mechanical alloying and shear extrusion," Journal of Alloys and Compounds, 375 (2004), pp. 107-113

[39] J. Jiang, L. Chen, S. Bai, Q. Yao, Q. Wang, "Thermoelectric properties of textured p-type (Bi, $Sb)_2Te_3$ fabricated by spark plasma sintering," Scripta Materialia, 52 (2005), pp. 347-351

[40] R. W. Rice, *Mechanical Properties of Ceramics and Composites* (Marcel Dekker, New York, 2000), pp. 201-217

[41] M. W. Barsoum, *Fundamentals of Ceramics* (McGraw-Hill, New York, 1997), pp. 415-418

[42] A. L. Pilchak, F. Ren, E. D. Case, E. J. Timm, H. J. Schock, C. –I. Wu, T. P. Hogan, "Characterization of dry milled powders of LAST (lead-antimony-silver-tellurium) thermoelectric material," Philosophical Magizine, 87 (2007), pp. 4567-4591.

[43] B. D. Hall, F. Ren, J. R. Johnson, E. J. Timm, E. D. Case, "Agglomeration during wet milling of LAST (Lead-Antimony-Silver-Tellurium) powders," Materials Chemistry and Physics (submitted)

[44] W. –S. Liu, B. –P. Zhang, J. –F. Li, L. –D. Zhao, "Thermoelectric property of fine-grained $CoSb_3$ skutterudite compound fabricated by mechanical alloying and spark plasma sintering," Journal of Applied Physics D: Applied Physics, 40 (2007), pp. 566-572.

[45] W. H. Coulter, "High Speed Automatic Blood Cell Counter and Cell Analyzer," Proceedings of the National Electronics Conference 12 (1956), pp. 1034-1042.

[46] F. G. Anderson, T. F. Tomb, M. Jacobson, "Analyzing Midget Impinger Dust Samples with an Electronic Counter," U.S. Bureau of Mines Report of Investigations 7105 (1968)

[47] T. F. Tomb, L. D. Raymond, "Evaluation of the Penetration Characteristics of a Horizontal Plate Elutriator and a 10-mm Nylon Cyclone Elutriator," U.S. Bureau of Mines Report of Investigations 7367 (1970)

[48] T. Allen, *Particle Size Measurement*, 3rd Edition (Chapman and Hall, London, 1981) pp. 392-413

[49] H. C. van de Hulst, Light Scattering by Small Particles, John Wiley & Sons, New York, 1957, pp. 114-130

[50] E. I. Benitez, D. B. Genovese, J. E. Lozano, "Scattering efficiency of cloudy apple juice: Effect of particles characteristics and serum composition," Food Research International, 40 (2007), pp. 915-922

[51] O. Munoz, H. Volten, J. W. Hovenier, M. Min, Y. G. Shkuratov, J. P. Jalava, W. J. van de Zande, L. B. F. M. Waters, "Experimental and computational study of light scattering by irregular particles with extreme refractive indices: hematite and rutile," Astronomy & Astrophysics, 446 (2006), pp. 525-535

[52] A. Jurewicz, V. Orofino, A. C. Marra, A. Blanco, "Optical constants of powdered limestone by taking into account the grain shapes: Applicability to Martian studies," Astronomy & Astrophysics, 410 (2003), pp. 1055-1062

[53] D. B. Curtis, M. Aycibin, M. A. Young, V. H. Grassian, P. D. Kleiber, "Simultaneous measurement of light-scattering properties and particle size distribution for aerosols: Application to ammonium sulfate and quartz aerosol particles," Atmospheric Environment, 41 (2007), pp. 4748-4758

[54] S. Brunauer, P. H. Emmett, E. Teller, "Adsorption of Gases in Multimolecular Layers," Journal of the American Chmical Society, 60 (1938) pp. 309-319.

[55] A. Montaser, J. A. McLean, H. Liu, J. –M. Mermet in: A Montaser (Ed.), Inductively Coupled Plasma Mass Spectrometry, Wiley-VCH, New York, 1998, pp. 1-31

[56] I. L. Turner, A. Montaser in: A Montaser (Ed.), Inductively Coupled Plasma Mass Spectrometry, Wiley-VCH, New York, 1998, pp. 265-334

[57] R. Thomas, "Spectroscopy tutorial—A beginner's guide to ICP-MS—Part I," Spectroscopy, 16 (2001) pp. 38-42.

[58] A. Montaser, M. G. Minnich, H. Liu, A. G. T. Gustavsson, R. F. Browner in: A Montaser (Ed.), Inductively Coupled Plasma Mass Spectrometry, Wiley-VCH, New York, 1998, pp. 335-420

[59] D. B. Sirdeshmukh, K. G. Subhadra, K. Kishan Rao, T. Thirmal Rao, "Hardness of Crystals with NaCl Structure and the Significance of the Gilman-Chin Parameter," Crystal Research and Technology, 30 (1995), pp. 861-866

[60] M. A. Korzhuev, S. N. Chizhevskaya, T. E. Svechnikova, O. G. Karpinskii, A. V. Arakcheeva, G. U. Lubman, A. N. Milykh, "Mechanical properties of single and polycrystals of copper-doped Bi_2Te_3 and $Bi_2Te_{2.85}Se_{0.15}$," Inorganic Materials, 28 (1992), pp. 1093-1097

[61] J. W. Sharp, IEEE 22 International Conference on Thermoelectrics (2003), pp. 267-270

[62] F. Ren, B. D. Hall, J. E. Ni, E. D. Case, J. Sootsman, M. G. Kanatzidis, E. Lara-Curzio, R. M. Trejo, E. J. Timm, "Mechanical characterization of PbTe-based thermoelectric materials," in Thermoelectric Power Generation, edited by T.P. Hogan, J. Yang, R. Funahashi, and T. Tritt (Mater. Res. Soc. Symp. Proc. Volume 1044, Warrendale, PA, 2007), 1044-U04-04

[63] B. Houston, R. E. Strakna, H. S. Belson, "Elastic constants, thermal expansion and Debye temperature of lead telluride," Journal of Applied Physics, 39 (1968), pp. 3913-3916

[64] T. E. Svechnikova, S. N. Chizhevskaya, N. M. Maksimova, P. P. Konstantinov, G. T. Alekseeva, O. D. Chistyakov, "Doping of $Bi_2Te_{2.85}Se_{0.15}$ solid-solution with yttrium (Y_2Te_3) and gadolinium (Gd_2Te_3) tellurides," Inorganic Materials, 29 (1993), pp. 178-181

[65] S. N. Chizhevskaya, M. A. Korzhuev, T. E. Svechnikova, G. B. Sheina, "Plastic-deformation of Bi_2Te_3 and its solid-solutions—characteristic features in bending tests," Inorganic Materials, 30 (1994), pp. 447-450

[66] T. E. Svechnikova, N. M. Maksimova, P. P. Konstantinov, "Bi_2S_3 Doping of Single Crystals of Bi_2Te_3-based Solid Solutions," Inorganic Materials, 34 (1998), pp. 233-235

[67] T. E. Svechnikova, S. N. Chizhevskaya, N. M. Maksimova, N. V. Polikarpova, P. P. Konstantinov, G. T. Alekseeva, "Doping of the $Bi_2Te_{2.85}Se_{0.15}$ solid-solution with germanium," Inorganic Materials, 30 (1994), pp. 161-164

[68] T. E. Svechnikova, S. N. Chizhevskaya, N. V. Polikarpova, P. P. Konstantinov, G. T. Alekseeva, L. E. Inozemtseva, "Effect of cadmium telluride on the thermoelectric and mechanical properties of $Bi_2Te_{2.85}Se_{0.15}$ single crystals," Inorganic Materials, 28 (1992), pg. 227-231

[69] T. E. Svechnikova, P. P. Konstantinov, G. T. Alekseeva, "Physical properties of $Bi_2Te_{2.85}Se_{0.15}$ single crystals doped with Cu, Cd, In, Ge, S, or Se," Inorganic Materials, 36 (2000), pp. 556-560

[70] R. Martin-Lopez, S. Zayakin, B. Lenoir, F. Brochin, A. Dauscher, H. Scherrer, "Mechanical properties of extruded $Bi_{85}Sb_{15}$ alloy prepared by mechanical alloying," Philosophical Magazine Letters, 78 (1998), pp. 283-287

[71] S. N. Chizhevskaya, T. E. Svechnikova, V. N. Geminov, I. M. Kop'ev, N. M. Maksimova, "Concentration dependences of the mechanical properties of solid-solutions of the cross-section $Bi_2Te_{2.85}Se_{0.15}$-In_2Te_3 in the system Bi-In-Se-Te," Inorganic Materials, 25 (1989), pp. 1182-1184

[72] S. S. Kim, T. Aizawa, "Crystallographic Anisotropy Control of n-type Bi-Te-Se Thermoelectric Materials via Bulk Mechanical Alloying and Shear Extrusion," Materials Transactions, 45 (2004), pp. 918-924

[73] K. R. Iyer, G. C. Kuczynsk, "Effect of wavelength of illumination on photomechanical effect in germanium," Journal of Applied Physics, 42 (1971), p. 486

[74] W. D. Callister, Jr., Materials Science and Engineering: An Introduction, Wiley and Sons, New York, 2003, p. 750

[75] I. J. McColm, Ceramic Hardness, Plennum, New York, 1990, p. 252

[76] H. J. McSkimin, P. Andreatch, "Elastic moduli of silicon vs. hydrostatic pressure at 25 °C and –195.8 °C," Journal of Applied Physics, 35 (1964), pp. 2161-2165

[77] I. Paul, B. Majeed, K. M. Razeeb, J. Barton, "Statistical fracture modeling of silicon with varying thickness," Acta Materialia 54 (2006), pp.3991-4000

[78] Landolt-Bornstein: Numerical Data and Functional Relationships in Science and Technology, Vol. 17a (Physics of Group IV Elements and III-V Compounds), Springer-Verlag, Berlin, 1982, pp. 62; 104; 234

[79] F. Ericson, S. Johansson, J. A. Schweitz, "Hardness and fracture-toughness of semiconducting materials studied by indentation and erosion techniques," Material Science and Engineering A—Structural Materials, Properties, Microstructure, and Processing, 105 (1988), pp. 131-141

[80] M. Schaper, M. Jurisch, F. Bergner, R. Hammer, "Fracture mechanical evaluation of GaAs wafers," in Progress in Semiconductor Materials II: Electronic and Optoelectronic Applications, edited by B. D. Weaver, M. O. Manasreh, C. Jagadish, and S. Zollner (Mat. Res. Soc. Symp. Proc. Volume 744, Warrendale, PA, 2002) M1.8.1-M1.8.6

[81] Landolt-Bornstein: Numerical Data and Functional Relationships in Science and Technology, Vol. 17f (Physics of Non-Tetrahedrally Bonded Binary Compounds II), Springer-Verlag, Berlin, 1983, pp. 176; 277

[82] A. –B. Chen, A. Sher, W. T. Yost in: K. T. Faber, K. Malloy (Eds)., Semiconductors and Semimetals, Academic, San Diego, 1992, Vol. 37, p. 68

[83] D. Berlincourt, L. R. Shiozawa, H Jaffe, "Electrostatic properties of sulfides, selenides, and tellurides of zinc and cadmium," Physical Review, 129 (1963), pp. 1009-1017

[84] A. G. Evans, H. Johnson, "Fracture-mechanics study of ZnSe for laser window applications," Journal of the American Ceramic Society, 58 (1975), pp. 244-249

[85] R. J. Robinson, Z. K. Kun, "p-n junction zinc sulfo-selenide and zinc selenide light emitting diodes," Applied Physics Letters, 27 (1975), pp. 74-76

[86] A. N. Krasnov, Y. N. Purtov, Y. F. Vaksman, W. Serdyuk, "ZnSe blue-light-emitting diode," Journal of Crystal Growth, 125 (1992), pp. 373-374

[87] http:www. Jmloptical.com/level2/TechInfo/materialstable.aspx

[88] J. B. Watchman, Mechanical Properties of Ceramics, Wiley, New York, 1996, pp. 92-100

[89] H. Wang, R. B. Dinwiddie in: D. M. Rowe and W. D. Porter (Eds.), Thermal Conductivity 27, DEStech Publications, Incorporated, Lancaster, 2005, pp. 484-492

[90] D. K. Shetty, A. R. Rosenfield, P. McGuire, G. K. Bansal, W. H. Duckworth, "Biaxial flexure tests for ceramics," American Ceramic Society Bulletin, 59 (1980), pp. 1193-1197

[91] Ren F., "Mechanical characterization and powder processing of lead telluride based thermoelectric materials," Ph. D. Dissertation, Chemical Engineering and Materials Science Department, Michigan State University, 2007

[92] N. Suzuki, S. Adachi, "Optical constants of $Pb_{1-x}Sn_xTe$ alloys," Journal of Applied Physics, 79 (1996), pp. 2065-2069

[93] E. A. Albanesi, E. L. Peltzer y Blanca, A. G. Petukhov, "Calculated optical spectra of IV-VI semiconductors PbS, PbSe and PbTe," Computational Materials Science, 32 (2005), pp. 85-95

[94] Saturn DigiSizer 5200 Operator's Manual V1.12, 2007

[95] Reichart Analytical Instruments, "Sucrose Solution Percent by Weight Concentration (Brix Value) Versus Refractive Index at 20 Celsius and 589nm Wavelength (per ICUMSA)," Depew, NY, 2006

[96] M. N. Rahaman, Ceramic Processing and Sintering, Second ed., Marcel Dekker, New York, 2003, pp. 50-57

[97] M. G. S. Murray, J. Wang, C. B. Ponton, P. M. Marquis, "An improvement in processing of hydroxyapatite ceramics," Journal of Materials Science, 30 (1995), pp. 3061-3074

[98] H. Kamiya, K. Isomura, G. Jimbo, "Powder processing for the fabrication of Si_3N_4 ceramics: 1. Influence of spray-dried granule strength on pore-size distribution in green compacts," Journal of the American Ceramic Society, 78 (1995), pp. 49-57

[99] Sciencelab.com, Inc, Houston, TX

[100] ASTM Designation E1461, 2001 "Standard Test Method for Thermal Diffusivity of Solids by Flash Method," Annual Book of ASTM Standards,Vol.14.02